OBSERVATIONS IN TURBULENT BUOYANT JETS BY USE OF LASER-INDUCED FLUORESCENCE

Thesis by

Dimitris Antony Papantoniou

In Partial Fulfillment of

the Requirements

for the Degree of

Doctor of Philosophy

California Institute of Technology

Pasadena, California

1986

(Submitted October 18, 1985)

To my parents who gave me the desire to learn

AKNOWLEDGMENTS

I wish to express my deepest appreciation and gratitude to my advisor Professor Ericson John List for providing a lighthouse of ideas, encouragement and support during the three years of working with him. His attitude made this research effort a meaningful learning experience. I would also like to thank Professors Donald Coles and Edward Zukoski for numerous fruitful discussions and Professor Paul Dimotakis who introduced me to the experimental methods that were employed in this research.

I am indebted to many of my fellow graduate students at the Keck Hydraulics Laboratory and the Aeronautics Department at Caltech. Among these, Dr. Manooch Koochesfahani and Dr. Godfrey Mungal deserve special mention for numerous discussions and ideas. Special mention is also due to my friend Mr. Paul Belvoir who shared, in long discussions, some of his expertise in digital electronics that was instrumental for this reaserch.

I wish to thank the staff of the Keck Hydraulics Laboratory for their help, and for providing a pleasant atmosphere for conducting the experiments. Special mention is due to Mr. Leonard Montenegro who helped in the wiring and troubleshooting of the electronic circuitry. The expert assistance of Melinda Hendrix-Werts and Amy Kubin in the preparation of the thesis manuscript is also gratefully appreciated. Finally, I would like to extend my thanks to my family and dear friends who provided me with the emotional support that made this work

possible.

The personal financial support of the Alexander Onassis Fellowship and the California Institute of Technology is gratefully aknowledged. This research was supported, in part, by the National Science Foundation under Grant no. CEE81-17272A01 and Grant no. CEE84-12641.

ABSTRACT

The entrainment mechanism and mixing process are investigated in the far field of a liquid phase buoyant jet issuing into an unconfined, quiescent medium, by an experimental technique based on laser-induced fluorescence (LIF). Visualization experiments show the existence of a large scale organization in the far field, with structures spanning the radial extent of the conical flow region. Quantitative, high-resolution measurements of scalar concentration were performed along the radial direction in the far field region. For each data set, a large number of successive instantaneous concentration profiles were obtained by combining LIF techniques with linear photodiode array imaging and high speed data acquisition. The measurements revealed that the instantaneous profile bears no resemblance to the time-averaged profile. The flow interior is characterized by large spatial gradients of concentration, associated with interfaces between mixed jet fluid and fresh, entrained ambient fluid transported to regions deep into the flow. This is inconsistent with the description of transport by gradient diffusion concepts. The probability of finding unmixed ambient fluid and the concentration variance are greatly increased under the action of buoyancy. At any axial location, the arrival of a structure front is marked by a spatially coherent (along the radial direction) increase in the local concentration level. It is found that, within the structure, values of the concentration are generally decreasing in the upstream

direction; substantial uniformity within the mixed fluid portion is observed along the radial direction. In the conical flow field of the momentum jet, a central region (in fixed spatial coordinates) may be identified within which the local mixed fluid composition is relatively uniform. This is not the case for the buoyancy driven plume, due to a greater variance in the position of the large structure and the high value of the intermittency. It is suggested that fluid is entrained by vortical motions mainly from the back and side regions of the large structure. Flow visualization reveals vorticity in the axial direction which enhances the mixing process; this vorticity appears stronger in the buoyancy driven flow. The results of these experiments are interpreted through a simple conceptual model of entrainment and mixing that encompasses the observed large scale organization of the buoyant jet flow.

TABLE OF CONTENTS

LIST OF FIGURES

LIST OF TABLES

LIST OF SYMBOLS

c_j	jet spreading parameter
c_p	plume spreading parameter
d	nozzle diameter
g	gravitational acceleration
m	specific mass flux
r	radial distance from flow axis
s	large structure spacing
t_ν	Kolmogorov time scale
x	axial distance from source
A_c	constant in jet concentration decay law
B	specific buoyancy flux
C_o	initial tracer concentration
C_m	mean centerline tracer concentration
C_{max}	maximum tracer concentration
C_{mxd}	mean mixed concentration
C_{rms}	root mean square tracer concentration
C_{rmsc}	contribution to the variance from unmixed fluid
C_{rmsh}	contribution to the variance from mixed fluid
$\langle C \rangle$	ensemble average concentration
H	heat source output (Joules/sec)
I_m	intermittency value
J	specific momentum flux
L	visual flow width

L_M	characteristic length scale
L_Q	characteristic length scale
R	correlation function
R_o	initial Richardson number
Re	Reynolds number
Sc	Schmidt number
T	large scale passage time, integral time scale
T_j	large scale time for jet flow
T_p	large scale time for plume flow
U	axial velocity
U_c	local convection velocity in axial direction
U_m	mean centerline axial velocity
U_o	velocity at nozzle exit plane
Y	tracer mass flux

GEEEK LETTERS

α	angle of spread of buoyant jet
ε	rate of dissipation of kinetic energy
η	non-dimensional radial distance
Λ	integral length scale
λ_ν	Kolmogorov length scale
ν	kinetic viscosity
ξ	spatial separation variable for correlation
ρ_a	ambient fluid density
ρ_o	initial plume fluid density

σ	volumetric thermal expansion coefficient
τ	time delay variable for correlation

SUBSCRIPTS

j	refers to momentum jet quantities
o	refers to initial (nozzle) conditions
p	refers to buoyant plume quantities

INTRODUCTION

1.1. Background

Many flows in engineering practice and in the environment are either influenced by the presence of buoyancy forces or are entirely driven by such forces. The buoyancy forces arise when there is a density anomaly in the fluid acted on by gravity. Waste fluids discharged into the environment usually have a density different from that of the ambient fluid. The density difference under these circumstances leads to a buoyancy induced rise or fall of the discharged fluid, which influences its mixing and spreading in the environment.

Axisymmetric jet flows have played an important role in understanding of shear flow in general and buoyancy driven flows in particular. The geometry of such flows is simple, which makes experiments relatively straight forward so that the flow is well documented. Furthermore, since the flow characteristics are of direct importance in many engineering design problems, including dilution, mixing and combustion, there is a strong motivation to understand the motion in detail. Finally, since it is one of the simpler shear flows of higher dimension (the simplest being the plane shear layer), it is of basic theoretical importance.

The focus of the present investigation is the study of the flow structure of a round turbulent buoyant jet, defined here as the flow

field set up by a source of momentum and buoyancy in an infinite medium. An example of a very large scale geophysical flow falling in this category is depicted in the photograph of Figure 1.1. There have been a large number of both experimental and theoretical studies of round pure momentum jets. Buoyant jets (and the limiting case of pure buoyant plumes) have received less attention. As a consequence, a wealth of information on the turbulent flow characteristics of round jets has been gathered. A comprehensive review of the available experimental results was made by List (1982). Besides the experimental efforts, the turbulent buoyant jet has been the subject of a number of numerical studies; these usually rely on a turbulent flow modelling hypothesis of some kind to circumvent the closure problem of the flow equations.

The majority of the experiments to the present have centered on point measurements of the relevant flow quantities. These include the velocity field and the concentration field of a passive scalar carried by the jet fluid. The components of the local velocity vector have been measured usually with hot-wire probes and more recently with non-intrusive laser Doppler velocimeters. The local concentration has been measured with hot wires, thermistor probes, density probes and non-intrusive optical techniques. The latter include light scattering, Raman spectroscopy, and laser-induced fluorescence among others. Emphasis has been placed on increasing the spatial and temporal resolution of the measuring device so that even smaller scales of flow can be studied. From these point measurements a

comprehensive view of the time-averaged characteristics of the turbulent jet flow field has emerged. These include velocity and concentration profiles, turbulent fluctuation intensity and shear stress profiles, as well as the gross entrainment characteristics.

However, despite the large number of experiments that have been made, aspects of the turbulent flow field relating to its instantaneous structure and possible organization remain unclear. This is partly due to the complexity of the turbulent flow in general, and partly due to the lack of experimental means that early workers in the field had at their disposal. It may also be attributed, as List (1982) has noted, to a preoccupation with time-averaging techniques. Interest in the possible large structure organization of the far field of turbulent jets and buoyant plumes has been fueled by the large scale flow organization apparent in the plane shear layer. During the last decade, the work of Brown and Roshko (1974) has inspired a thorough investigation of the shear layer large scale flow dynamics. Flow visualization techniques have proved to be very useful in revealing the flow structure, at least in this case where the flow is mainly two-dimensional.

The traditional view of turbulent structure and mixing in the far field of the axisymmetric jet is that it is mainly composed of eddies that are smaller than the lateral extent of the turbulent region. These eddies evolve in a rather stochastic manner and are responsible for the transfer of momentum and kinetic energy as well as the

entrainment of ambient fluid and subsequent mixing process. This traditional view, that has been based mainly on point measurement techniques, has lent support to the notion that local turbulent fluxes of various quantities are proportional to the local gradient of the corresponding average profiles. While numerical studies based on these models have some success in predicting profiles of averaged flow quantities, they have difficulty in predicting the mixing characteristics of shear flows (Walker 1979).

Evidence from the experimental information gathered on the shear layer suggested that the classical view of mixing and entrainment has to be modified to incorporate the large scale structure characteristics of the turbulent flow field. Broadwell and Breidenthal (1982) noted that mixing models based on the concept of gradient diffusion are inapplicable to turbulent shear layers, and proposed a new simple model for mixing in such flows. This incorporates the observed large scale shear layer features and concepts from the Kolmogorov cascade in scales. Predictions based on their model are in qualitative agreement with experimental observations on mixing in the plane shear layer made by Konrad (1976), Mungal (1983) and Koochesfahani (1984).

The first quantitative investigations of turbulent round jet structure by Corrsin (1943), Wygnanski and Fiedler (1969) and others were centered on an analysis based on conventionally averaged turbulence quantities. During the last decade, there have been a

growing number of investigators that have attempted to establish the existence of a large scale organization in axisymmetic shear flows. Relevant information on the instantaneous structure of the flow and its possible large scale organization may be gathered from point measurements, especially as experiments are becoming increasingly sophisticated with the widespread use of modern digital techniques. To this end, several investigators have performed conditionally sampled single-point measurements in the far field of the round momentum jet. From the measurements of Antonia, Prabhu and Stephenson (1975) and Sreenivasan, Antonia and Britz (1979), it has been recognized that large scale motion plays an important role in the heat and momentum transport in the intermittent region of the far field in a round momentum jet (off the centerline). Their measurements also revealed ramp-like patterns in velocity and concentration time traces. These patterns extended over times comparable to or larger than the characteristic large scale time of the flow. Chevray and Tutu (1978), from conditional measurements, detected the directions of fluid motion in the "turbulent" and "irrotational" regions. Very recently, Komori and Ueda (1985) performed conditionally sampled two-point measurements in the far field of the momentum jet. They detected large coherent eddies with a vortical structure consisting of stong outward turbulent motion from inside the jet, turbulent reverse flow and inflow in the irrotational ambient region (entrainment).

It should be noted here that virtually all of the quantitative studies of this nature have been performed in gas phase momentum jets.

Experimental evidence from shear layers indicates that the molecular diffusivity, characterized by the value of the Schmidt number (Sc = ν/D), may affect the mixing process. The experiments of Konrad (1976), Breidenthal (1978), Koochesfahani (1984) suggest that the amount of molecular mixing in gas and liquid shear layers (at the same conditions otherwise) differs by a factor of two. Hence, since the Schmidt number of a gas phase and liquid phase flow differs typically by three orders of magnitude, some caution should be excercised when comparing flow quantities associated with mixing at different Sc. The dependence of mixing on Sc has not yet been established for the round jet and plume.

Direct evidence of a flow organization in the far field of a liquid phase round jet has been presented by Dimotakis, Miake-Lye and Papantoniou (1983). Large concentration fronts spanning the flow width were evident in their laser induced fluorescence photographs. They found that concentration along the axis of the jet does not decrease monotonically but rather in discrete steps corresponding to the advancing concentration fronts. They also found that unmixed ambient fluid can be transported deep inside the jet (up to the jet centerline) suggesting a large scale transport mechanism. Very recently, Dahm (1985), using the laser-induced fluorescence technique, also presented photographic evidence of a large scale organization in the far field region of the round jet along with PDF's of the concentration.

To date, there have been no investigations to explore the possible large scale organization of the turbulent buoyant plume. There are also no measurements that explore the effect of buoyancy on the instantaneous shear flow structure. Some photographic evidence in the work of Kotsovinos (1977) suggests a possible flapping mode for the far field plane plume. It is of interest that Uberoi and Singh (1975) observed such a mode for the plane jet. The latter obtained spatially correlated measurements (instantaneous profiles) by projecting a hot wire probe at right angles to the flow direction. This technique may be considered as a forerunner of the technique employed in the present investigation.

In a recent experimental study, Papanicolaou (1984) investigated thoroughly the time averaged properties of a liquid phase round buoyant jet. He conducted single point measurements using two-component laser Doppler velocimetry and a laser-induced fluorescence technique. These earlier results formed a broad basis for the present study which shifts its focus to the instantaneous flow structure and, hence, complements this earlier work.

The experiments which are presented here were aimed at both a qualitative and a quantitative study of the entrainment and mixing characteristics of a round buoyant jet. They were also intended to determine the degree of a large scale organization in the turbulent buoyant flows and to document its main features. The cases of a liquid phase pure momentum jet and a buoyancy driven plume were

studied. Experiments covered the range from the jet exit to 150 exit diameters, at a Reynolds number up to 10,000 for the turbulent momentum jet. For the case of the buoyant plume, the experiments were carried to large axial distances where the initial momentum flux plays no apparent dynamic role and the flow is entirely driven by buoyancy forces. The instantaneous concentration field was studied quantitatively with a passive scalar technique that allows temporally and spatially correlated measurements to be made. It is based on laser-induced fluorescence (LIF) diagnostics. The instantaneous fluorescence signal, which is related to the local scalar concentration, was measured at a large number of points in the flow by a scanned linear photodiode array and recorded in real time by a high speed data acquisition system. A brief discussion on the basic principles of this technique along with a summary of previous work based on LIF is presented in the next section.

1.2 Laser-Induced Fluorescence (LIF)

This technique is based on the property of certain organic dyes, such as Rhodamine 6-G or Sodium Fluorescein, to fluoresce when excited by light in the visible spectrum. The resulting fluorescence is at a longer wavelength than the wavelength of the exciting light. The dye is premixed with one of the mixing species (here the jet fluid) and the flow field is illuminated in a spatially controlled manner by a laser beam. The resulting fluorescence intensity is related (see Appendix B) to the local species concentration, which is labeled by

the dye, and to the local laser intensity. The technique has the advantage of being non-intrusive and of being capable of yielding quantitative concentration measurements with high spatial and temporal resolution. The spatial resolution of such concentration measurements depends critically on the local dimensions of the illuminated region in the flow, i.e., the thickness of the laser beam, and the resolution of the imaging system. The temporal resolution depends on the sampling rate of the data acquisition system, since the time required for the fluorescence to "turn on" is typically of the order of only a few nanoseconds (Becker 1969).

Both qualitative and quantitative LIF data have been reported previously, mostly on shear layers and turbulent jet flows. Several investigators used a laser beam to illuminate the flow and recorded the fluorescence at a point on the beam using a single sensor (Robben et al. 1976, Dewey 1976, Liu et al. 1977, Papanicolaou 1984). The experiments that were performed using this method yielded average and fluctuating concentration measurements that compared well with results based on other types of concentration probes. Measurements of space-time correlations using LIF (possible with the use of a second sensor) have not been reported to date.

The first field measurements in shear flows were of qualitative nature; they were performed using laser sheet illumination with photographic film as the recording medium. These include the works of Dewey (1976), Liu et al. (1977), Bernal (1981), Dimotakis et al.

(1981,1983), Koochesfahani (1984) and Dahm (1985). The photographs have been very useful in obtaining qualitative results about the flow structure. Still pictures of round jet of high spatial resolution (obtained by keeping the laser sheet thickness to about a millimeter) showed that (Dimotakis et al. 1983) unmixed ambient fluid is transported deep within the flow region, suggesting that the far field jet entrainment is dominated by large vortical structures. In a recent attempt to quantify these photographic LIF measurements, Jimenez et al. (1985) digitized a number of motion picture frames from the transverse image of a plane shear layer and digitally processed them to offer an "internal view" of the spanwise vortical structures. While this method offers quantitative results on the instantaneous concentration field, it has the disadvantage of being computationally cumbersome and not very precise, due to the inherent limitations of photographic film as the recording medium. An alternative has been offered by the use of self-scanning linear and 2-D photodiode arrays to record the fluorescence resulting from laser line or sheet illumination of the flow field. Dimotakis et al. (1983) used line illumination and such a 1024 element linear array to study features of the entrainment of a turbulent jet. They recorded fluorescence data using the analog output of the array to modulate the intensity of an oscilloscope beam that was driven in a raster scan fashion to produce an x-t diagram of the concentration field. Kychakoff et al. (1983) recorded single-frame data using sheet illumination and a 2-D (100 x 100 element) photodiode array camera. However, due to the large

number of data points per frame and the scanning rate requirements, their multi-frame capability was limited to only a few frames of data. Important contributions to the LIF method were made by Koochesfahani (1984) who used line illumination and a linear photodiode array to acquire quantitative multi-frame species concentration data of high temporal and spatial resolution in a shear layer. His method was subsequently applied to the study of round jets by Dahm (1985).

In the present experimental study of jets and buoyant plumes both sheet and line illumination LIF methods were employed. For the sheet illumination experiments data acquisition relied on photographic recording, both in the form of still pictures and high speed movies. For the line illumination experiments, a 1024 element linear self-scanning photodiode array was used to record the species concentration. For each experiment, a large number of instantaneous concentration profiles were recorded in real time by a computer-based data acquisition system. This system was developed during the course of the investigation, and is capable of acquiring multi-frame data at a sufficiently high rate to "freeze" the turbulent motion across the extent of the flow under consideration.

Chapter 2

EXPERIMENTAL FACILITY AND INSTRUMENTATION

Two sets of experiments were performed in two different water jet facilities. The first set employed sheet illumination of the jet flow field and photographic recording of the fluorescence intensity. The second set employed line illumination of the jet and plume flow field and recorded the fluorescence intensity with a Reticon array camera. The apparatus used in the experiments and the outline of the experimental methods involved are presented in the next sections.

2.1 Sheet Illumination

These experiments were aimed at an understanding of the structure and characteristics of the turbulent jet flow field. They were qualitative in nature, since the fluorescence was photographically recorded. On the other hand, since the data obtained by this method are resolved spatially and temporally to a high degree, it has proved very helpful in understanding the basic features of the flow.

2.1.1 Flow apparatus

This set of experiments was conducted in the GALCIT water jet facility (see Figure 2.1a), which was designed and integrated by G.L. Brown, P.E. Dimotakis and the author. It is a stainless steel construction (1m x 1m x 2m) with 1" thick glass windows on all four

sides, approximately 0.9m by 1.2m. A small window in the center of the bottom of the reservoir serves as an additional optical access port. The fluid in the reservoir discharges to a large PVC dump tank through four 6" lines symmetrically placed at the bottom of the reservoir. The fluid velocity in the test section can be controlled by means of pneumatically actuated adjustable butterfly valves, installed in the discharge lines. These allow a co-flow velocity to be generated in the test section. The jet supply system is of a blown down type, consisting of a high pressure air supply regulated through a sonic orifice metering valve to drive the jet fluid. A schematic of the jet supply system is shown in Figure 2.1b. Note that the velocity at the jet exit is controlled by the sonic orifice size. Jet diameters of 0.76cm, 2.54cm and 7.62cm were used. Details on the construction of the water jet facility can be found in Dimotakis and Papantoniou (1981).

2.1.2 Optical set up

The schematic of the optical set up is shown in Figure 2.2. A 3 Watt argon ion laser (Coherent Radiation CR-3) beam was used as the light source. All lines of the laser beam were used in these experiments. The beam was passed through a combination of long focal length plano-convex and short focal length cylindrical lenses to produce a sheet of light diverging in one direction and focusing in the other. A sheet thickness of a few hundred microns with a width of about 40 cm was produced in this fashion. This sheet could be aligned

with the jet centerline, or on any other plane parallel to the jet axis.

For the 2-sheet illumination experiments, the optical set up was as shown in Figure 2.3. The two sheets were adjusted to intersect at right angles, both containing the jet axis. A system of mirrors, designed so that the fluorescence from both illuminated planes could be recorded on a single photographic film with minimal perspective distortion, was constructed as shown in Figure 2.4 for use in these experiments.

2.1.3 Data acquisition

The fluorescing dye used in these experiments was usually Rhodamine 6-G (sodium Fluorescein was also used in a few experiments). The tracer dye was premixed with the jet fluid at a concentration of about 6 mg/liter. Still pictures of the flow were obtained through a motor driven 35 mm camera (Nikon with a Nikkor 50 mm f1.4 lens, or with a Micro Nikkor 55 mm f2.8 lens) on Kodak Tri-X (400 ASA) film. An orange filter, placed in front of the camera lens, was used to block any laser light scattered by small particles in the test section. High speed movie films were taken with a 16m pin-register movie camera (Teledyne DBM-55). Framing rates of up to 200 frames per second were employed, depending on the jet Reynolds number. For still pictures, the exposure was of the order of 2-4 ms, in order to freeze the motion of the interfaces in the region of interest.

2.2 Line Illumination

This set of experiments forms the major portion of this work that provided the basis for a quantitative description of the concentration field of the buoyant plume and the pure momentum jet. Sodium Fluorescein or Rhodamine 6-G dye was premixed with the jet (or plume) fluid and used as a tracer in the flow. The resulting fluorescence was measured by a linear array of photodiodes and recorded in real time by a computer based data acquisition system.

2.2.1 Flow apparatus

The experiments were conducted in the water jet facility of Keck Laboratory which was designed and integrated by Papanicolau (1984). This flow facility consists of a large (1.15 m x 1.15 m x 3.35 m capacity) water reservoir and an associated jet supply system. A schematic of this facility appears in Figure 2.5. Large (1.2 m x 1.85m) 1" thick tempered glass windows on all four sides of the steel framed reservoir permit observation of the flow in the test section from all directions. There is a precision instrument carriage extending around all four sides of the tank, which can be accurately traversed in the vertical and horizontal directions. It is used to mount the 5 Watt Argon-Ion laser head and the associated optics, as well as the optics for the laser Doppler velocimeter system. An in-line filter was installed for these experiments on the high pressure laboratory water line that fills the tank, to remove small particles

from the tank water.

The jet water supply system consists of a 200 liter mixing tank, a constant head tank and the jet plenum assembly. The jet flowrate is controlled by a calibrated valve and flowmeter combination. The jet plenum assembly may be mounted either on the top of the test section with jet fluid discharging vertically downwards, or on a platform rail system at the bottom of the test section with the jet fluid discharging vertically upwards. Both methods of mounting were employed in these experiments. Various diameter nozzles (ranging from 0.5cm to 5.08cm) may be fitted to the jet plenum so that jets and plumes of a wide range in Reynolds number can be generated. These nozzles have an exit plane flush with the lower jet plenum wall and use a contraction ratio optimized for the Reynolds number range employed in these experiments. For detailed documentation of the Keck water jet facility the reader is referred to Papanicolaou (1984).

2.2.2 Optical set up

A schematic of the optical arrangement for the LIF line experiments is presented in Figures 2.6 and 2.7. The light source was the blue line from a Spectra-Physics 5 Watt Laser, equipped with an Etalon assembly. The laser was operated in the light-stabilized mode by a feedback system that adjusts the current to maintain the beam intensity constant (within 1%). The laser beam was manipulated by a combination of 90 degree prisms and mirrors to intersect the flow

either in the vertical or in the horizontal direction. The beam was focused to a waist of about 500 microns in the test section by a long focal length convex lens appropriately placed on the beam path. These optical components were coated with a special anti-reflection coating to minimize the laser intensity loss from the stray reflected beams. Since the overall quality of the laser beam in the test section has a direct impact on the attainable spatial resolution, extreme care was taken in this part of the experimental set up.

The fluorescence intensity along the beam was measured by a 1024 element linear photodiode array camera (Reticon LC300). A section of the beam inside the test section was focused on the array by a single photographic lens mounted on the camera housing. An optical filter, placed in front of this lens blocked any light of wavelength shorter than 530 nm from laser light scattered from particles in the flow field. The image magnification ratio depends on the focal length of the imaging lens and the distance from the test section. It was desired to image the entire radial extent of the flow while retaining sufficient resolution for each individual pixel. It was found that a Nikon 50mm f1.8 lens was well suited and it was used for these experiments. The response of the imaging system was tested by measuring the array output obtained by transversing a source of light on the object plane. At a magnification ratio of 20:1 the response variation over the entire length of the array was within 10% of the maximum which occurred at the center. This variation is partly due to image distortion due to the imaging lens and the glass windows of the

tank, and partly due to the pixel response nonuniformity over the length of the array (see Appendix A). These nonuniformities are accounted for by the calibration procedure that was employed. Image ratios of 20:1 to 15:1 were used, depending on the experimental requirements, by selecting the distance of placement of the Reticon array camera from the laser beam in the test section.

The linear array is permanently placed on the image plane of the lens, so the lens and array combination must be adjusted as a whole for fine focusing of the laser beam on the array. This was achieved by attaching the camera housing on a surveying unit platform, which in turn was mounted on a very sturdy tripod. This arrangement gave the necessary degrees of freedom for fine adjustments in all three directions. It should be noted that optimal focusing of the array is generally a difficult task since the beam and the array must be brought parallel in the plane that contains the optical axis of the focusing lens. This is best accomplished by maximizing the output of every individual sensing element when a very weak and uniform dye solution is filling the test section. The intensity pattern that corresponds to the optimal focusing under these conditions is close to the one obtained with no dye in the test section and the optical filter removed from the focusing lens. It should be noted that with a uniform dye concentration in the test section, the beam intensity is changing with distance (see Appendix B) since its cross-sectional area is varying as described by Gaussian optics, and it is attenuated by the dye molecules in its traverse of the test section. Attenuation

effects are an exponential function of the dye concentration. At the minimum dye concentration required to obtain a useful response out of all the array pixels, beam attenuation was noticeable when both the green and the blue lines from the argon ion laser were exciting the dye. It was found that for the sodium Fluorescein dye, optimum response was obtained when only the blue laser line was exciting the dye and an optical filter with correspondingly higher cutoff frequency was placed in front of the array imaging lens. In this mode of operation, since the dye was using the available laser power much more efficiently, more fluorescence was emitted for the same laser intensity and dye concentration. The beam attenuation was correspondingly higher. For the Rhodamine 6-G dye, optimum operating conditions were obtained when only the green laser line was used, with a correspondingly lower cutoff optical filter in front of the array imaging lens. Thus, a combination of low dye concentration, high laser intensity at a single wavelength and the appropriate optical filter could be selected to minimize the effect of attenuation over the imaged portion of the beam and, at the same time, obtain a useful response out of the array.

It is possible to account for the combined effects of attenuation, beam nonuniformity and possible misalignment of the focusing system by the calibration procedure outlined in Appendix B. For purposes of calibration, a small vessel made from plate glass with a square cross-section and filled with a calibrating dye solution was placed in the path of the laser beam just outside the tank. A

magnetic stirrer was continuously operated to keep the calibrating solution circulating so that dye bleaching and beam blooming effects (Koochesfahani 1984) could be avoided. With an imaging lens and slit combination, a small section of the beam in its transverse of this vessel was focused on a single photodiode (Hamamatsu S1223-01). An optical filter, used to block any light scattered by the laser, was placed in front of this photodiode.

2.2.3 Data acquisition

The heart of the LIF experimental apparatus is the linear photodiode array (Reticon, RL-1024G) contained in the LC300 camera unit. A more detailed description of the array characteristics and operation procedure is given in Appendix A. The 1024 photodiodes (pixels) measured 16 by 25 microns each. They are closely spaced on an IC package, which is mounted on a small board containing part of the scanning circuitry. This board, along with a second board containing the rest of the scanning circuitry, as well as an amplification and sample and hold circuit, are contained in the small camera housing. The scanning circuit samples sequentially all the array pixels at a user defined frequency (up to 800 KHz) and outputs a video-like analog signal synchronized with the array clock. The individual output of each photodiode is proportional to the integrated (over the scan time) light incident on the photodiode (see Appendix A).

Since the array has 1024 individual sensors, the throughput requirements of the data acquisition system are relatively high. The time resolution for each individual sensor is given by the time between scans, which is the input clock period multiplied by the number of pixels in the array. Thus, to obtain the same time resolution per pixel as from a single probe, the pixel-to-pixel sampling rate (and consequently the system throughput rate) must be typically three orders of magnitude higher than the sampling rate for the single probe. Also, the total amount of data that is generated for the same experimental duration is correspondingly larger. Since the computer memory is typically not large enough to store all the data generated during the experimental run, a high speed magnetic storage device is necessary to accumulate the large amounts of real time data. Furthermore, the digitization of the analog array output may proceed at rates higher (by a factor of 10) than the commercially available analog-to-digital converters (A/D) can handle. As a result of these requirements, some effort was spent by the author in designing and integrating a data acquisition system that provided an adequate throughput rate for the flows under study. A brief documentation of this system is given in Appendix A.

Reticon array data were thus recorded by the computer-based data acquisition system that was developed during the course of this investigation. This is a simple and relatively inexpensive system, based on the Laboratory's PDP-11/60 processor (on DEC Unibus) that has 1/4 Mbyte of main memory, hard disk storage, a 16-channel A/D

converter board, a DMA port and a real time programmable clock. The Reticon array data were digitized by the ADC board, which is a custom made single channel 8-bit A/D system capable of conversions at 2MHz. The ADC was designed to interface to the processor's Unibus through the direct memory access (DMA) port. The digitized data were stored in real time on the system's 7.2 Mbyte Winchester disk (DSD880). A schematic of the data acquisition system appears in Figure 2.8.

While burst-mode operation of the input DMA process allows the transmission of Reticon array output scans to memory at the highest array clocking rate (900 KHz), the available memory size limits the number of full array scans that can be recorded in this fashion to only 192. In order to record continuously a large number of array scans to disk, the input DMA was operated in the usual shared-cycle mode, which limits its maximum input rate to about 500 KHz. However, since the Winchester disk output rate is much slower, the system had to be programmed carefully for optimum performance and data throughput maximization. Two 64 Kbyte data buffers in higher memory were used for temporary storage space. An interrupt-driven data acquisition program synchronized the two main DMA processes - input from the ADC and output to disk. The maximum sustainable data throughput that was achieved in this fashion was 130 Kbytes/sec (close to the maximum rated speed of the Winchester disk).

The calibrating solution photodetector output voltage was preamplified and low pass filtered by a Krohn-Hite electronic filter.

It was then amplified and offset appropriately to be transmitted in differential form to the AD11-K A/D converter of the Laboratory's computer for digitization. This detector was calibrated with input power and dye concentration and its behavior was found to be linear over the range used in the experiments.

Although these experiments were focused on the instantaneous structure of the concentration field, velocity measurements at a single point in the flow field (along the beam path) were also recorded during some of the experiments. For these measurements, the two component laser Doppler velocimetry (LDV) optical arrangement equipped with Bragg cell exciters (as implemented by Papanicolaou 1984) was used to obtain the laser Doppler signals. These signals were fed to the dual LDV processor designed by Gartell (1978), that has since been modified to improve its performance. The processor output is an analog signal related to the instantaneous velocity. A schematic of the optical arrangement and the LDV processor logic is presented in Figures 2.9 and 2.10. The axial and radial velocity data from a point in the test section were taken synchronously with Reticon array data, with one u-v velocimetry measurement recorded for each recorded scan of the array. The velocity data from the two LDV channels and the concentration data from the single calibrating photodiode were sampled through 3 channels of the AD11-K board of the PDP 11/60. These data were stored in real time in lower memory buffers, which were transferred continuously to a removable hard disk (RK05) during the Reticon array sweeps.

The highest array clocking rate that could be used in the experiments, when all the array pixels and all the scans were continuously digitized and recorded, corresponds to the maximum throughput rate sustained by the system, i.e., 130 KHz. This translates to a multi-frame rate (in this case equal to the array scanning rate) of about 126 Hz. Note that correspondingly higher clocking rates of the array could be used if one or more scans and/or pixels were skipped per one recorded. It was in fact desirable to skip scans when recording fluorescence data, in order to keep the total amount of data generated per run manageable while still resolving the essential features of the flow. The scanning rate of the array could also be increased independently of the pixel rate if it was desired to scan only a portion of the 1024 array pixels. The array clocking rate and the rate at which scans were recorded depended on the flow characteristics and other experimental considerations and are given along with other experimental parameters in Chapter 4.

CHAPTER 3

ENTRAINMENT CHARACTERISTICS OF BUOYANT JETS

This chapter starts with a brief presentation of the characteristic features of axisymmetric buoyant jet flows. These include previous experimental findings, and basic results that rely on dimensional arguments rather than the full equations of motion, which are mathematically intractable. A complete review of the experimental literature is not intended; the review articles by List (1982) and Chen and Rodi (1980) are a reference when no other is explicitly given. The essential features of the two limiting cases (that of the momentum driven jet and of the buoyancy driven plume) that are relevant to the present work are presented first so that they will form a reference basis for the results discussed in the subsequent sections. Some qualitative features of the buoyant flow that were observed by the LIF sheet illumination method are also discussed in this chapter.

3.1 Similarity Considerations and Scaling Laws

The flow field of the turbulent jet is produced by a pressure drop through a circular orifice. Ideally it is the flow field due to a steady momentum point source in an unconfined quiescent medium. The momentum jet is entraining ambient fluid and, for a strong enough momentum source, the resulting flow field is a conical region with a spreading angle independent of the initial jet characteristics.

Actual jets, issuing from a finite diameter nozzle, are characterized by the Reynolds number $Re = U_o d/\nu$ and the specific initial momentum flux

$$J_o = \frac{1}{4} \pi d^2 U_o^2. \tag{3.1}$$

Note that in what follows, the term specific (i.e., normalized by the fluid density) will not be explicitly mentioned when referring to specific fluxes of momentum, mass and tracer concentration. This is done because with the proper normalization, the absolute fluid density does not affect the equations of motion appropriate to our problem. For high enough Reynolds number, where the viscosity can be neglected, the local momentum flux and the distance from the source are the governing parameters of the flow. This implies (Landau and Lifshitz 1959) that the flow width L scales with axial distance as

$$L = \alpha x. \tag{3.2}$$

Furthermore, the requirement of conservation of momentum in the axial direction implies that the local mean flow velocity must scale as

$$U_m = A \frac{J^{1/2}}{x}. \tag{3.3}$$

The jet entrainment and dilution of a scalar quantity carried initially by the jet fluid is intimately connected to the value of the spreading angle and the velocity decay law. In fact, dimensional arguments show that the volume flux in the far field jet region is

related to the axial distance from the momentum source and the local momentum flux as

$$m(x) = c_j J^{1/2} x. \tag{3.4}$$

The volume flux therefore is increasing linearly with axial distance, by entrainment of ambient fluid. Since the axial momentum flux is conserved, the entrainment per unit axial length is independent of the axial distance from the momentum source and is scaled by

$$\frac{d}{dx} m(x) = c_j J^{1/2}. \tag{3.5}$$

The constant $c_j = m(x)/xJ^{1/2}$ has been experimentally evaluated to be about 0.25 (Fischer et al. 1979). It has been termed as jet spreading parameter by List and Imberger (1973), since it is related to the value of the spreading angle of the flow.

If the initial jet fluid discharged from the nozzle is carrying a tracer at a certain concentration C_o, it will be diluted by the turbulent jet flow field. Since the tracer mass flux Y is conserved, dimensional analysis may be used to predict the tracer concentration evolution with axial distance as

$$C_m(x) \sim \frac{Y}{xJ^{1/2}} \tag{3.6}$$

or in the more usual form

$$C_m(x) = A_c\ C_o(\frac{x}{d})^{-1}. \tag{3.7}$$

From the summary of experimental results of Chen and Rodi (1980) it is suggested that the value of the constant A_c is 5.6.

If the fluid discharging from the orifice has a density different than that of the ambient fluid, the flow is affected to a certain degree by the presence of body forces resulting from the action of gravity. We are concerned here with the case where the mean flow direction is parallel to the direction of gravity and the density difference acts to accelerate the flow (i.e., positively buoyant). An important parameter in this case is the rate at which the weight deficiency is introduced into the flow field from the source, termed here as specific buoyancy flux B. In particular, if fluid of density ρ_o is discharging into ambient fluid of density ρ_a at the volumetric flow rate m_o then

$$B = (\frac{\rho_a - \rho_o}{\rho_o})\ gm_o. \tag{3.8}$$

In this case, where the buoyancy flux is generated by a mass discharge, conservation of mass implies that the buoyancy flux is conserved only if the ambient density remains constant. Note that in a fluid environment where buoyancy is generated by a heat source H (joules/sec) the buoyancy flux is given by

$$B = \frac{g\sigma H}{\rho c_p} \tag{3.9}$$

where σ is the volumetric thermal expansion coefficient, and c_p is the specific heat at constant pressure. In a uniform density environment heat conservation and the constancy of the volumetric expansion coefficient imply the conservation of B. In ideal gases where σ and ρ are inverse functions of the temperature, heat conservation implies the conservation of B. Whereas B is <u>not</u> generally conserved, the flows that satisfy the conditions of conservation of the buoyancy flux form a rather wide category of flows to which we are going to limit our attention.

The buoyant axisymmetric plume is ideally the flow field resulting from a buoyancy point source in an infinite medium. The body forces have a dominant character in this case. The flow field set up in this manner has some similarities with that of the momentum jet. In particular, the flow spreading angle has been observed to be about the same as for the momentum jet. However, the dominant flow parameter in the buoyant plume is considered to be the buoyancy flux B which, along with the axial distance from source, x, characterize other quantities in the far field. Similarity arguments (e.g., List 1982), analogous to those for the momentum driven jet, then predict that the width of the flow in the far field scales with the distance from the source as

$$L = \alpha x.$$

As noted above, the value of the constant α is about the same for jets and plumes. The evolution of mean centerline velocity along the plume axis is given by

$$U_m(x) \sim \frac{B^{1/3}}{x^{1/3}}. \tag{3.10}$$

Both the local specific momentum flux and mass flux vary with x according to

$$J(x) \sim B^{2/3} x^{4/3} \tag{3.11}$$

$$m(x) \sim B^{1/3} x^{5/3}. \tag{3.12}$$

It should be noted that the plume spreading parameter

$$c_p = \frac{m(x)}{xJ(x)^{1/2}} \tag{3.13}$$

is independent of x as in the momentum jet. The experiments of Rouse et al. (1952) and Papanicolaou (1984) suggest that c_p=0.25. The entrainment rate in the buoyant plume depends on the local momentum flux and the axial distance from the source. In particular

$$\frac{d}{dx} m(x) = \frac{5}{3} c_p J(x)^{1/2}. \tag{3.14}$$

Since c_p is approximately equal to c_j, equations (2.5) and (2.14) imply that the plumes entrain much more ambient fluid than momentum

jets for the same local momentum flux. The tracer concentration evolution with axial distance is given by

$$C_m(x) \sim \frac{Y}{B^{1/3} x^{5/3}} \tag{3.15}$$

where the coefficient of proportionality has been determined by experiments to be about 9.1.

The more general case, where both momentum and body forces coexist, is referred to as a buoyant jet. This flow includes the momentum jet and the buoyant plume as limiting cases. It has been shown that a turbulent momentum jet that has an initial density difference will gradually make a transition to a plumelike flow at large enough values of the axial distance from the source. The appropriate length scale that describes this transition is the length scale defined by the initial specific momentum and buoyancy fluxes. In particular, experiments on buoyant jets (Papanicolaou, 1984) indicate that plumelike flow starts at $x/L_M > 5$ where

$$L_M = \frac{J_o^{3/4}}{B^{1/2}}. \tag{3.16}$$

The importance of the length scale L_M in relation to buoyant jets was recognized by Morton (1959). The length scale defined using the initial specific momentum and mass fluxes as

$$L_Q = \frac{m_o}{J_o^{1/2}} \tag{3.17}$$

characterizes the initial flow geometry and may be used to non-dimensionalize the axial distance from the source in jetlike flows. (Note that L_Q is proportional to the exit diameter for a round nozzle). The dimensionless ratio of these two scales is the initial Richardson number

$$R_o = \frac{L_Q}{L_M} = m_o \frac{B^{1/2}}{J_o^{5/4}}. \tag{3.18}$$

This number, initially defined by Morton (1959), represents the relative importance of inertia and buoyancy forces. The evolution of the entrainment in the transitional buoyant jet flow as a function of the axial distance from the source was described by List and Imberger (1973, 1975). Their analysis, based on dimensional arguments, was largely confirmed by the experiments of Kotsovinos (1977) in the plane geometry and Papanicolaou (1984) in the axisymmetric geometry.

The simple relations presented in this section are derived from dimensional arguments based on similarity principles and have been confirmed by previous experiments. Their usefulness lies in the description of mean flow properties and growth laws. It is clear that similarity arguments alone are not sufficient for the detailed description of the flow structure. Since a theoretical analysis of the turbulent flow based on the full equations of motion is beyond the

present state of the art, the description of the flow structure still relies on a statistical approach combined with use of similarity principles and geometrical relations relevant to the flow. Experiments are instrumental for this description. It should also be noted that the problem of scalar transport in turbulence cannot be solved without knowledge of the structure of the turbulent velocity field. However, the works of Kolmogorov (1941), Obukhoff (1949) and others have established the concept that turbulence at small enough scales has a universal character. This makes the properties of the flow field under study relevant to other turbulent flow problems.

The present investigation is concerned with a study of the instantaneous flow structure and its relation to the entrainment mechanism. In comparing the buoyancy driven plume to the momentum driven jet, questions that may be asked are: i) What are the general features of the flow structure and how do they relate to the presence of buoyancy? ii) How does the buoyancy dominated flow achieve the observed larger entrainment rate as compared to the momentum driven flow of the identical geometry? and iii) How does the larger entrainment rate manifest itself in the instantaneous flow structure? In the following section, through qualitative results based on flow visualization, we will examine the buoyant jet under a perspective that incorporates its large scale vortical organization.

3.2 Flow Visualization With LIF

Flow visualization is often the best method of gaining insight into the turbulent flow processes. The initial phase of this work dealt with the recording of LIF photographs of turbulent momentum jets and buoyant plumes under various flow conditions. Through this technique important flow features were revealed; this prompted a subsequent quantitative study of the concentration field by means of LIF imaging on the Reticon photodetector array.

It should be noted here that there are major advantages offered by the LIF visualization method over conventional methods. Using LIF, it is possible to "slice" through the turbulent flow and obtain an instantaneous concentration pattern at a spatial resolution dictated by the sheet thickness and the imaging optics. By controlling the time exposure on the photographic film, time resolution adequate to freeze the turbulent motions of the interfaces can be achieved. It should be noted that, since the flow scales vary over the axial distance as described in the previous section, the resolution is non-uniform along the axis of the flow. However, since scales increase with axial distance, observations optimized for a certain axial location will be more than adequate downstream of this axial location. The method to circumvent this limitation of the LIF method was to use different jet nozzles (often operated at different conditions) to visualize the flow at adequate resolution over different axial ranges.

It should be stressed that resolution is an important issue; most

of the conventional techniques of flow visualization (that did not address this issue in an adequate manner) missed significant features of the entrainment process. Conventional flow visualization studies relied on back lighting and used smoke or dye to render the turbulent mixed regions visible. The buoyant jet appearing in Figure 1.1 is naturally visualized in this manner. These methods, that offered an external or integrated view of the flow region, have suggested that it is in fact possible to define an interfacial surface that separates the "turbulent zone" from the "non-turbulent" one. Indentations of this surface, not actually visible with conventional techniques but measured by point probes, have been dealt with by use of the concept of intermittency. This was originally defined by Corrsin and Kistler (1955) as the fraction of the time a particular point spends inside the "turbulent zone." The above ideas have lent support to the classical description of the turbulent entrainment process (and the related mixing and dilution) in terms of the diffusive, random walk propagation of this interface into the irrotational, ambient fluid region (Townsend 1976). However, as indicated from recent flow visualization results obtained by the LIF method (Dimotakis, Miake-Lye and Papantoniou 1983, Dahm 1985), this description of the entrainment process is not applicable to jet flow. From their published photographs it is suggested that the interfacial surface, if one can be defined, is topologically very complex. Furthermore, it was suggested by these observations that ambient fluid is entrained by large vortical motions to regions deep within the jet, where it

participates in the mixing process.

3.2.1 Turbulent momentum jets

A time sequence of LIF photographs of a momentum jet is presented in Figure 3.1(a-d). The fluorescence from two perpendicular planes intersecting on the jet axis is simultaneously recorded for each realization. Planar views A and B (see Figure 2.4), appear on the left and right hand side of each photograph, respectively. The Reynolds number is 8,500 based on jet exit diameter of 2.54 cm. The time exposure for each frame is 2ms, and the time interval between successive frames is 270 ms. These photographs span the axial range of $0 < x/d < 27$. The effective thickness of each light sheet was about 0.5 mm. However, in this case the image ratio used and the film characteristics limit the spatial resolution to about 4 mm. Some perspective distortion is inevitably introduced by the imaging system of 3 mirrors (see Figure 2.4), as can be evidenced by the apparent thickness of the light sheets on the jet axis. In observing these pictures, it should be kept in mind that the local fluorescence intensity recorded on film is proportional to the local dye concentration averaged over the light sheet thickness and the local light intensity. The light intensity is varying in a Gaussian manner across the flow (the maximum intensity occurs at the centerline in both views). It is also attenuated by the presence of dye in the direction of the light beam propagation (bottom to top), so it is difficult to compare intensity levels at different parts of the film.

Despite these limitations, important flow features may be discerned in these LIF photographs which are discussed below.

A sharp difference in flow structure exists between the initial mixing region around the potential core of the jet and the far field region. The initial stage, extending to a few jet diameters around a conical potential core region, is markedly less "turbulent" than the far field region. Vortices around the potential core are formed at rather regular intervals and convect downstream up to the end of the potential core at ($x/d \simeq 5$). Pairing occurs during the lifetime of these ring-type vortices. Helical structures are also common, seemingly formed by the pairing process. An example of a helical structure can be observed on Figure 3.1a, at about x/d=3. At the end of the potential core, these initial ring vortices are destroyed in a rather violent fashion, and the flow evolves to its far field state.

Deep indentations, marking the presence of unmixed ambient fluid, can be observed everywhere in the flow. These indentations are present at larger axial distances (not shown here) and are a feature of the flow that cannot be observed from other types of flow visualization. The indentations are not axisymmetric, indicating substantial azimuthal motions. The presence of ambient fluid deep into the conical region defined by the average visual jet boundary indicates that the instantaneous radial concentration profile does not have the Gaussian character that one would expect on the basis of the time-averaged profile shape. It also suggests that the interfacial

surface separating the ambient unmixed fluid with the fluid marked by the dye is considerably more complex than the one suggested on the basis of conventional visualization methods. The complexity of this interface can be evidenced by the presence of a seemingly unconnected small braid of dyed fluid slowly advancing through plane A at about x/d=20.

The overall character of the flow is rather random, marked by the simultaneous presence of a variety of scales at any axial location. However, a noteworthy feature of the momentum jet flow is the presence of discrete concentration fronts that span a large portion of its lateral extent. These fronts are discerned in the pictures (to the extent that the imaging resolution and other non-uniformities permit) by a spatially coherent drop in intensity. The front-to-front spacing increases roughly linearly with axial distance. Fronts were observed at the largest axial distances investigated (150 diameters). We may consider the fluid regions between adjacent fronts as belonging to individual structures. The dynamical significance of these structures to the entrainment process and mixing is an open question. There is some evidence of a large scale body rotation, but longer time sequences than in Figure 3.1 are necessary. However, even from short sequences as the one depicted here, it appears that the leading (downstream) fronts are moving faster than the sides and back regions as these structures are convecting downstream. This may be caused by the higher shearing action occuring off the centerline. It is possible then that, as a result of this shearing action, fresh ambient

fluid is brought deep inside the structures mainly through the sides and back regions. Fluid from the fronts is often ejected outwards towards the jet boundary where it stays inactive for a long time before it gets re-entrained by a subsequent structure (longer time sequences are necessary to observe this phenomenon). It may be noticed that fluid regions immediately behind the structure fronts are free of ambient fluid and appear mixed rather uniformly. The extent of this uniformity in concentration is not clear from these qualitative observations. This issue will be addressed in the next chapter, along with other quantitative results.

The existence of such discrete concentration fronts suggests that molecular mixing in the momentum jet may be achieved in steps, rather than in the continuous fashion indicated by the mean concentration decay law. The evolution of the concentration field with axial distance from the source may then be described in terms of coherent eddies that span the width of the flow, and whose origin is traced at the end of the potential core region. These observations are in general agreement with the results of Dimotakis, Miake-Lye and Papantoniou (1983) and Dahm (1985).

The simple model of mixing in the shear layer flow of Broadwell and Breidenthal (1982) may provide a basis for a description of the mechanics of entrainment and mixing in the jet flow. According to this model, ambient fluid entrained by shear action into the structure will undergo a continuous change in scale by essentially inviscid

motions with very little or no mixing until the Kolmogorov scale is reached. At this scale, where viscosity becomes dominant, mixing proceeds by molecular diffusion.

Multiple turbulent energy cascades in scales, starting at the large scale structure size L and ending at the Kolmogorov scale, would thus proceed during the lifespan of the structure. For large enough Reynolds number, it is argued by Broadwell and Breidenthal that the time to cascade to the Kolmogov scale starting from scale L is proportional to L/U, where U is the characteristic large scale velocity difference. The time to homogenize (reach a state of molecular mixing) would require a time proportional to $(L/U)(Sc/Re^{1/2})$. The implication is that for flow at a given Reynolds number, the effect of a large value of the Schmidt number is to delay mixing at the molecular level after the Kolmogorov scale is reached. However, for high enough values of the Reynolds number, the time to mix to molecular level is much smaller than the time L/U which governs the entrainment. Note that this approach suggests that entrainment and molecular mixing are two distinct processes. Molecular mixing, which is important in problems of chemical reaction and combustion, has a Schmidt number dependence. For the flow depicted in Figure 11, the time for molecular mixing is about 7 times larger than the "turnover time" L/U, implying that a pocket of fresh fluid entrained by the structure at a particular station cannot reach a molecularly mixed state within a local flow diameter. However, unmixedness at the molecular level cannot be detected by the passsive LIF technique

because of inadequate spatial resolution. Actually, since unmixed fluid at these scales would be averaged out and appear as mixed, the technique provides only the upper limit of any measure of mixedness.

The implied dependence of the time scale for entrainment on the axial distance can be deduced from the similarity relations discussed in the previous section. Taking, at any axial station x, $L=\alpha x$ and $U=U_m=U_c$ it is implied that the local time scale governing the large scale entrainment process is

$$T_j(x) \simeq \frac{\alpha x^2}{J^{1/2}}.$$

If the structures are considered to span the conical region of the flow, their scales must be increasing linearly with x so that similarity is maintained. Thus, from geometrical considerations an estimate of the spacing between successive structures might be obtained if we consider them as spheres touching each other and being bounded by the cone of the (solid) angle α. Under these approximations we may write for the spacing $s(x_i)$

$$s(x_i) \simeq \frac{2\alpha}{2-\alpha} x_i$$

where x_i is the position of the i^{th} structure.

The discrete average concentration levels in the fronts, if they are to conform to the similarity requirement $(x/d)C_m(x)=$constant would scale as

$$C(x_{i+1}) \simeq \frac{2-\alpha}{2+\alpha} C(x_i).$$

3.2.2 Buoyant plumes

Photographs of buoyant plumes visualized by LIF are presented in Figure 3.2a-c. The plume is discharging from a 1cm diameter nozzle at the middle of the tank. The plume fluid is a solution of alcohol in water and the ambient fluid is a salt solution. The initial density difference is 1%, but refractive indices of the fluids are matched (Hannoun, 1985). The photographic exposure time is 17 ms and the light sheet thickness is about 0.5 mm. Approximately 75 exit diameters are imaged on film.

In Figure 3.2a the valve controlling the flow rate was shut, so plume fluid is drawn vertically upwards from the source entirely by buoyancy forces. The flow resembles the familiar smoke plume out of a burning cigarette, except that here LIF permits observation of regions in the plume "interior." This flow has some resemblance to the flow pattern of a low Reynolds number jet. An example of such a jet visulized by the LIF method is presented in Figure 3.3 for comparison. It may be observed that the plume is significantly more intermittent. Scales as small as L/10 are actively entraining ambient fluid, as evidenced by the continuous intertwining of the interfaces. This results to the higher degree of dilution which is expected from this flow on dimensional grounds. Note that in this case high values of the local concentration also imply a locally stronger density

difference, to the extent that the differences in the molecular diffusion coefficients of dye, salt and alcohol can be neglected. However, since the molecular diffusion time scales are much longer than the local turbulent time scale, these differences should be negligible.

Figures 3.2b and 3.2c are still LIF photographs of a forced plume. Fluid at an initial density difference of 1% is discharged with an initial velocity of 10 cm/sec. The ratio of the momentum length scale (L_Q = 0.9 cm) to the buoyancy length scale (L_M = 3.2 cm) gives an initial Richardson number R_o = 0.28. Therefore, the considerations presented in Section 3.1 indicating that the momentum jetlike character of the flow is lost after a distance $x/L_M = 5$, would predict a plumelike behavior after x/d = 20.

Evidently the change in behavior from jetlike flow to plumelike flow is gradual. Spadelike structures characteristic of the momentum jet can be discerned in the initial region of Figure 3.2b. While the large scale features of the momentum jet flow have their counterpart in the developed plume region, apparent differences develop in the smaller scale stucture of the concentration field. In comparison with Figure 3.1, it may by observed that a different characteristic of the buoyancy dominated flow compared to the momentum dominated flow is the relative importance of smaller scales in the entrainment process. Figure 3.2c depicts an enlarged portion of the buoyant flow regime. A sharp concentration front is observed to span a large portion of the

radial extent of the layer. Clearly, more ambient fluid can be found in the plume interior than in the jet. This observation is consistent with the high rms values of turbulent concentration and high intermittency throughout the plume regime measured by Papanicolaou (1984) and Kotsovinos (1977). The sharp concentration fronts and the abundance of ambient fluid in the plume interior are important features of the buoyant plume flow, indicating that entrainment into the plume region is achieved by large scale vortical motions. A feature that is related to the increased efficiency of the entrainment and mixing mechanism of the buoyant flow is the large variation of concentration level occurring over small scales, particularly over the braids of the winding vortices. It should be noted here that the characteristic time for entrainment and mixing in the plume scales with axial distance differently from that in the momentum jet. For $L \simeq \alpha x$, $U_c \simeq (B/x)^{1/3}$ we obtain an upper estimate for this time scale

$$T_p = \frac{\alpha x^{4/3}}{B^{1/3}}$$

Note that this scaling depends on the selected eddy size through the angle α. For scales smaller than $L=\alpha x$ that participate in the entrainment/mixing process, while essentially convecting at the same velocity as the large scales, an accordingly smaller time scale for entrainment should be expected. At any rate, it should be observed that the characteristic time for mixing at a certain axial distance is much smaller when buoyancy rather than momentum is driving the flow,

generally implying faster mixing. This characteristic of the buoyant flow is reflected in the mean concentration decay laws. Finally, we should mention that the cascade in scales may proceed in a different manner when buoyancy is driving the flow. A density difference between the eddy and its environment gives rise to a body force proportional to the eddy volume that tends to accelerate it. Shear forces are generated as a result of body forces. Since scales down to L/10 are dominant, this would imply that buoyancy affects the cascade process (and the energy density spectrum) by a direct input of energy at wavelengths greater than 1/L, imposed by the flow geometry.

3.2.3 Transverse illumination of the flow region

A greater insight into the entrainment mechanism, is presented by photographs of a transverse plane (perpendicular to the axis) appearing in Figure 3.4. The Reynolds number for the momentum jet (in Figure 3.4a) was 5600, based on the exit diameter of 1 cm. The plume operating conditions for the flow in Figure 3.4b were similar to that of the flow in Figure 3.2. In both cases, the transverse plane was located at an axial distance of 66cm from the flow source. The light sheet thickness is comparable to that of the previous photographs. Hoewever, the overall resolution in the present case is higher due to a lower image ratio.

A striking feature of these high resolution photographs is that the concentration level over the central flow area is markedly higher

than that of the surrounding region. This central portion of the jet varies in time, corresponding to the the passage of the large structure over the axial location illuminated by the sheet. There is a high degree of regularity in the time evolution of this phenomenon, which will be examined quantitatively in Chapter 4. A feature of the plume flow, which may also be observed in the enlarged axial view of Figure 4.2c, is the very large variation in concentration level associated with the interwining of interfaces. There is evidence in these photographs suggesting the existence of substantial vorticity in the axial direction, resulting in a strong three-dimensionality of the flow. The quantitative measurements presented in the next chapter show that local variations in the plume reach much higher levels (compared to the mean concentration level) than in the momentum jet.

3.3 Sampling the Concentration Field

The existence of characteristic time scales and, correspondingly, of physical frequencies in the flow field, indicates that certain guidelines must be followed when sampling the concentration field of the turbulent buoyant flow. In particular, the length of the sample record and the sampling interval must be selected on the basis of the characteristic time scales in the flow.

3.3.1 The local large scale time

At any axial distance from the source the local convection velocity U_c and width of the flow L define a large scale time

$$T = \frac{L}{U_c}. \tag{3.19}$$

The dimensional considerations presented in the preceding sections imply that for the momentum driven jet,

$$T_j \simeq \frac{\alpha x^2}{J^{1/2}}. \tag{3.20}$$

The measurements of Wygnanski and Fiedler (1969) suggest that the convection velocity is approximately equal to the mean centerline velocity, so a more precise estimate can be written as

$$T_j = 0.66 \left(\frac{d}{U_o}\right)\left(\frac{x}{d}\right)^2. \tag{3.21}$$

For the buoyancy driven plume the convection velocity has not been measured. However, it is reasonable to assume that it is approximately equal to the mean centerline velocity. The scaling laws of the preceding sections would then imply

$$T_p \simeq \alpha B^{-1/3} x^{4/3}. \tag{3.22}$$

Note that the dependence on axial distance is different from that in the momentum driven flow. Taking $U_M = 3.5(B/x)^{1/3}$, as suggested in the review article of Chen and Rodi (1980), and using $\alpha = 0.4$, it is

obtained that

$$T_p = 0.114\ B^{-1/3} x^{4/3}. \qquad (3.23)$$

The large scale time at a particular axial location is related to the passage time of the the large scale eddies of the flow as seen from a probe fixed at this location. It has also been termed "large eddy turnover time" by some authors. Since the lowest frequency that is expected to exist in the flow is of the order of 1/T, it is implied that the sample record should be large enough compared to T for the formation of statistically stable estimates and the resolution of the lowest frequencies. The minimum sample record should be determined experimentally. From initial experiments of the type presented in the next chapter, it was found that 10 to 20 large scale flow times were necessary to obtain stable estimates of various statistical quantities. Note that the large scale time is associated with the local time necessary for entrainment, according to the considerations presented in Section 3.2.

3.3.2 The local small time scale

At the smallest scales of the flow the important parameters are the viscosity and the rate of dissipation of kinetic energy (i.e., the rate at which mechanical energy is converted to heat). The Kolmogorov length scale is defined via these parameters by

$$\lambda_\nu = \frac{\nu^{3/4}}{\varepsilon^{1/4}}. \tag{3.24}$$

The time scale pertinent to the Kolmogorov length scale is given by

$$t_\nu = \frac{\nu^{1/2}}{\varepsilon^{1/2}}. \tag{3.25}$$

The implication of the concept of the Kolmogorov cascade in turbulent scales by which kinetic energy is transferred from scale L to scale λ_ν is that

$$\varepsilon \approx \frac{U_c^3}{L}. \tag{3.26}$$

In other words, although the dissipation is ultimately due to viscosity, the order of magnitude of ε may be determined by those quantities that characterize the large eddies. Thus, the Kolmogorov scale is related to the large scale L and the Reynolds number through

$$\lambda_\nu \approx \frac{L}{Re^{3/4}}. \tag{3.27}$$

The characteristic small scale time is also related to T by

$$t_\nu \approx \frac{T}{Re^{1/2}}. \tag{3.28}$$

This time scale is indicative of the fastest variations in the turbulent flow as related to the random, jittery motion of the smallest eddies. In a mixing flow where one of the species is

labelled with a passive scalar, the small time scale is intimately connected to the motion of the thinnest interfaces. For large values of the Schmidt number, molecular mixing does not occur until the even smaller Batchelor length scale is reached. This scale is given by

$$\lambda_D = \frac{\lambda_\nu}{Sc^{1/2}}. \tag{3.29}$$

It is at the Batchelor scale that interfaces are actually smoothed by the action of molecular diffusion. Since the Schmidt number in gases and liquids differs almost by two orders of magnitude, some differences in the mechanism of mixing may be expected. In any case, the implication is that at a high value of Sc, the interfaces remain sharp at scales comparable to the Kolmogorov scale. This will actually be confirmed by the results to be presented in the next chapter.

The above considerations indicate that if the measurements are to resolve the scalar field at scales comparable to λ_ν and t_ν, the minimum spatial and temporal resolution of the probe should be given by Eqs. (3.27) and (3.28). It should be noted that if the flow patern convects with a mean velocity U, the sampling frequency necessary to "freeze" the thinnest interfaces would be given by U/λ_ν. This frequency, associated with the Kolmogorov passage time, is higher than the rate implied by Eq.(3.28) by a factor of $Re^{1/4}$. In the case that local values are integrated over larger spatial or temporal intervals, the measured instantaneous value will be smeared and not entirely

representative of the true one. Furthermore, if the measuring probe is unable to resolve these high frequencies, the estimated variance and dissipation rate of the scalar fluctuations will be lower than their true values.

For measurements over a large number of points in the flow field that are to be correlated in space and time, the above considerations place a stringent requirement on the system throughput rate. In particular, if the sampling interval is t_v and measurements over N spatial locations are to be performed, the sustained throughput rate must be of the order of $(NRe^{3/4})/T$. Therefore, the capabilities of the data acquisition system (that are fixed) place an upper limit on the local values of Re and T that may be investigated in this manner.

CHAPTER 4

DILUTION EXPERIMENTS USING LIF

A large portion of the present work deals with the acquisition and reduction of concentration data along a line in the far field region of a turbulent momentum driven jet and a buoyancy driven plume. The bulk of the measurements were made along the radial direction and were aimed at revealing the main features of the local instantaneous flow structure. These were complemented by measurements along the axial flow direction. Each experimental data set consisted of a large number of instantaneous fluorescence intensity profiles, along a line spanning the entire radial extent of the flow under consideration. These profiles were later digitally processed to extract the species concentration as a function of space and time.

4.1 Experimental Conditions

4.1.1 Radial LIF measurements in momentum jets

For these experiments, the laser beam intersected the turbulent flow field in the radial direction as shown schematically in Figure 2.6. The laser was operated in the blue line when the fluorescein dye was used to label the jet fluid. Fluorescein emits light strongly in the yellow-green portion of the spectrum. Thus, a light orange filter was placed in front of the Reticon array camera to block the scattered blue laser light in the test section, while allowing a considerable

portion of the green fluorescence signal to be recorded. It was found that this combination resulted in the most efficient use of the available laser power, which for these measurements was limited to 800 milliwatts. An Etalon assembly and a beam-stop were used to select the TEM_{oo} mode of laser operation; this resulted in a laser beam with a Gaussian intensity that was focused to about 500 microns in the test section. Since the local beam diameter defines the measuring volume, it also defines the degree of spatial resolution (normal to the direction of propagation) attainable by the LIF technique.

Two different nozzle diameters were used in these experiments. The smaller diameter (0.5 cm) was used to map the concentration field at an axial distance of 75 cm (150 jet diameters). The larger diameter (1cm) was used to image the fluorescence at an axial distance of up to 120 jet diameters. Since the Keck jet facility is 115 cm square, at this axial distance the radial extent of the flow field is still less than one-third of the width of the test section. This insured that effects of the finite tank dimension would be minimal. For the experiments presented here, the Reynolds number based on jet exit diameter and initial velocity was 5600 and 9000. Limits on the maximum Reynolds number that could be effectively employed were placed by requirements of high spatial and temporal resolution as discussed in Section 3.3.

In order to optimize the spatial resolution for each experimental set, the camera was placed at such a distance from the test section so

that 120% of the visual flow width would be imaged on the photodetector array. It was desired, for this set of measurements, to be able to resolve the small scales while imaging the entire extent of the flow. This requirement limited the jet exit Reynolds number that could be used to 10,000, since the smallest flow scales are typically of the order of $L/Re^{3/4}$ (Kolmogorov scale).

Radial LIF experiments were performed at the dimensionless axial distance of x/d = 48.5, 75, 105, and 150. In all cases, the image ratio and beam width combination resulted in a spatial resolution of the order of the local Kolmogorov scale. For each experiment, the Reynolds number and the axial distance from the source also dictated the array scanning rate and the recording rate (which can be set independently) since the optimal temporal resolution depends on the local time scales. The minimum array clocking rate used was 100 KHz, corresponding to a scanning rate of about 100 Hz. In all cases the line scan time was comparable to the (estimated) Kolmogorov passage time, to ensure that the details of the concentration field were not smeared by the time integration inherent to the technique. The operating conditions for the experimental runs that are presented are summarized in Table 4.1.

Prior to each experiment, the single calibrating photodiode was focused on the laser beam inside the small vessel placed on the beam path and was calibrated at the operating power conditions with known dye molar concentrations. The calibration curve was used to determine

the various molar concentrations employed in the experiment. Subsequently, a weak dye solution (about 10^{-7} molar) was mixed with tank fluid for the array calibration procedure. To focus the optical system, the array output was viewed on an oscilloscope screen and the camera mounting controls were adjusted so that the output of each array pixel was maximized. A large number of array scans (typically 1024) were obtained, time-averaged and recorded while the tank fluid was being stirred to avoid effects of beam bleaching and photoblooming (Koochesfahani 1984). The vessel with the calibrating solution was filled with a known dye concentration and was being sampled during each array scan; its output provided a reference concentration that was used subsequently for the conversion of the fluorescence measured by the array to local dye concentration (see Appendix B).

After calibration, the jet fluid was mixed with dye to a molar concentration that allowed the optimization of the dynamic range of the Reticon array at the axial distance under observation. The desired jet fluid concentration was estimated from the average concentration decay law for the momentum driven jet (Eq. 3.7) and was typically of the order of 10^{-6} molar. The tank was then filled with clear filtered water and a sufficiently long time period (at least 1 hr) was allowed for the motion inside the tank to subside before the jet was started. After a few minutes were allowed for the flow to establish itself, data acquisition commenced and lasted for 2-8 minutes. During this time, 5.2 million individual measurements were recorded on the magnetic disk. Due to the limitation in magnetic disk

space, data acquisition was stopped after 5120 scans were obtained if all 1024 pixels per array scan were being used. Longer time records (in some cases up to 20480 scans) were obtained by skipping an appropriate number of array pixels for each pixel recorded. It should be noted that this practice did not alter the spatial or temporal resolution intended for each individual measurement.

4.1.2 Radial LIF measurements in buoyant plumes

The radial LIF measurements in the buoyancy driven plume proceeded in more or less the same manner as in the momentum driven jet. An added experimental complication that occurs for flows with large density gradients is that of the refractive index variations. The use of clear water and brine as the working fluids was determined to be unacceptable for the LIF method employed in this investigation. Local density variations of the order of 1% cause a substantial wobble of the laser beam and affect the concentration measurements. The alternative that was adopted was to use an appropriate solution of ethyl alchohol in water for the (lighter) jet fluid and a NaCl solution for the (heavier) ambient fluid (Hannoun, 1985). With this combination, the refractive indices of the two fluids were precisely matched (to the fourth significant digit). A refractometer was used during the fluid preparation to aid in the refractive index matching procedure. As a result, for density differences of up to 1% that were used in the experiments, no perceptible beam wobble could be noticed. The jet plenum assembly for all plume experiments was mounted on the

platform inside the tank, with jet fluid discharging vertically upwards. The 1 cm nozzle was used in the plume experiments. Measurements were made at an axial distance of 105 cm from the exit plane using an initial density difference of 1%. At this axial location, the buoyant jet has evolved from an initially jet-like flow to a fully developed plume (Papanicolaou 1984). The experimental settings for the radial plume measurements are summarized in Table 4.2.

4.1.3 Axial measurements

For the axial meaurements, the laser beam was coincident to the geometrical axis of the flow as shown in Figure 2.7. The jet plenum, fitted with the 1 cm nozzle, was mounted on the rail system in the middle of the tank, with fluid discharging vertically upwards. The Reticon camera was placed at a distance such that the axial range of $0 < x/d < 120$ could be focused on the array. The array was clocked at 100 KHz, with one out of 4 array scans recorded on the magnetic disk. The measurement technique was identical to the one presented in Sections 4.1 and 4.2. However, important differences exist in the overall dynamic range of the data attainable from axial measurements. This is due to severe nonuniformities in the usable dynamic range of the array and accentuated problems of dynamic resolution to be dicussed shortly. Since there is significant dilution in the mean concentration level over this axial distance, the initial dye concentration that was used was such that the effect of attenuation of

the laser beam in its propagation up the axis of the flow was offset by the effect of dilution. Note that with this optimization, an approximately uniform dyanamic range is achieved for the jet flow since both the mean dilution and the mean attenuation depend in a linear fashion on axial distance, the two effects canceling each other. However, this optimization is not possible for the buoyant flow where the mean axial dilution does not vary linearly with axial distance. Therefore, the plume measurements had to be performed with a non-uniform dynamic range along the flow axis. Another problem with the axial measurements (especially in the jet flow), is the significant variation of local velocities over the imaged extent of the flow. This causes a non-uniform resolution of the measurements due to the variation of the dynamic component of array resolution (see Appendix A). Due to a combination of such effects, precise quantitative results were not extracted from the axial measurements. However, the significant features of the flow that could be observed from them are discussed in a subsequent section.

4.2 Data Reduction

After each experiment, the digital data were transferred from the magnetic disk to a magnetic tape for subsequent analysis. All data processing was performed on a VAX 11/750 computer. A first step in the reduction of each data set consisted of the conversion of the local fluorescence to dye concentration. An optical transfer function

was calculated from the calibration measurement and the data were processed on a scan-by-scan basis as outlined in Appendix B. The resulting concentration data may be represented by the two dimensional matrix $C(y_i, t_n)$

where $y_i = i\,\Delta y \quad i = 1,2, \ldots, M$

$t_n = n\,\Delta t \quad n = 1,2, \ldots, N$.

Note that Δy is the pixel-to-pixel separation and Δt is the time interval between recorded array scans.

4.2.1 Time averaged profiles of concentration

Statistical analysis procedures have been traditionally employed for the description of the turbulence flow field. For the discretely sampled concentration signal, the Reynolds decomposition of the instantaneous local concentration

$$C(y_i, t_n) = C_m(y_i) + c(y_i, t_n)$$

where

$$C_m(y_i) = \frac{1}{N} \sum_{n=1}^{N} C(y_i, t_n)$$

is formed by conventional averaging of a time record. For an ergodic process, convergence is assured if the number of samples is large enough. Physically, the requirement is that the number of samples N

times the sampling interval Δt should span an adequate number of large scale characteristic times of the flow. For the present experiments a minimum of 10 large scale times were spanned by the measurements (usually about 40). As a first step in the analysis, the data were tested for stationarity according to the procedures described in Bendat and Piersol (1971). It was actually found that about 10-20 large flow times were required for stationarity of data in a record.

The mean radial concentration profile in the momentum jet is presented as a function of the dimensionless radial coordinate $\eta = r/x$ in Figure 4.1. It is rendered in dimensionless form by normalization with its local centerline value. The mean profile has the familiar Gaussian form, reported by a number of other investigators and compares well with previous measurements. Furthermore, the mean profile exhibits similarity in the dimensionless axial distance x/d, as it is expected on dimensional grounds (see Section 3.1) even though no virtual origin has been fitted to the data.

The mean radial concentration profile in the buoyant plume is presented in a similarity form in Figure 4.2 along with the representative profile reported in the experiments of Papanicolaou (1984). Its form is, as expected, similar to that of the momentum jet except that it is a little narrower. Within the limited range of the appropriate dimensionless parameter x/L_M, the measured profiles do exhibit the similarity expected on dimensional grounds and overall compare fairly well with previous measurements.

As an aside, it should be mentioned that the calculation for the mean concentration profile would converge rapidly to the usual profile shape with an ensemble of only 25 instantaneous profiles summed but only if the ensemble consisted of profiles that were sufficiently separated in time, i.e., belonged to different large structures. This ensemble size was used by Uberoi and Singh (1975) who recorded instantaneous profiles in a plane jet that were uncorrelated in time. However, if the profiles in the ensemble are consecutive, a rough convergence to the mean profile shape is accomplished only if the number of profiles that are summed is enough to span one or two large scale times of the flow (in the present case about 300 profiles). This characteristic serves to illustrate the inherent "non-randomness" of the flow, as well as the relevance of the large scale time.

The radial profile of rms concentration fluctuations in the momentum jet and the buoyant plume, normalized by the mean concentration value at the centerline, is presented in Figure 4.3. The form of normalization used is meant to indicate the relative "intensity" of turbulent concentration fluctuations. The fluctuation intensity measured by the probes is generally higher than that reported previously. There are two points that should be made here concerning this disagreement. First, since the concentration fluctuation intensity is due to interfaces (eddies) of all scales, it is reasonable to expect that the higher the probe resolution (both in space and time), the higher the value of concentration fluctuation intensity measured. The correct value is theoretically obtained in

the limit by a probe that can resolve all flow scales including the Batchelor scale. For the present measurements, the spatial probe resolution is relatively high compared to measurements with a wire probe which has inadequate response to large amplitude fluctuations. Second, most reported values are for gas phase jets, which have a Schmidt number of the order of unity, as compared with the present measurements at Sc$\simeq$600. In accordance with the discussion of Section 3.3 it is reasonable to expect that molecular mixing (and the associated smoothing of concentration interfaces) is smaller at higher values of Sc. Representative values reported by previous investigators are rather scattered but such trends may be discerned from Table 4.3 below.

Table 4.3 Fluctuation Intensities in the Momentum Jet

Author	x/d	$C_{rms}/C_m(0)$	Comments
Antonia et al. (1975)	59	0.22	heated air/air
Birch et al. (1978)	70	0.28	methane/air
Becker et al. (1967)	64	0.22	air/air
Corrsin and Uberoi (1950)	30	0.18	air/air
Dahm (1985)	300	0.30	water/water
Papanicolaou (1984)	98	0.22	water/water
Present results	150	0.32	water/water

For the buoyancy driven plume, the normalized rms concentration profile shows that at the center of the flow the magnitude of the fluctuation intensity is roughly twice that of the momentum driven jet. The values measured are higher than the values measured previously by Papanicolaou and other investigators. Such high values

indicate that the flow is very intermittent, which will be confirmed by the analysis presented in Section 4.3.

To investigate the effect of probe resolution, the rms profile calculations were repeated at selected points within the layer using, instead of the instantaneous pixel value, the spatially averaged values of four neighboring pixels. This procedure in effect simulates the response of a probe with a decreased spatial resolution. The results for the plume flow are plotted in Figure 4.4. As might be expected, an obvious trend of decreasing fluctuation intensity for decreasing spatial resolution is observed.

4.2.2 The instantaneous concentration profile

Several instantaneous concentration profiles as recorded by the Reticon array are plotted in Figure 4.6 for the momentum jet and Figure 4.7 for the buoyant plume. The profiles are normalized by the mean centerline value. Although a discussion of the features of the instantaneous profiles will be made in the next section, some noteworthy features should be mentioned here. It is evident that in both flows the shape of the instantaneous concentration profile has no resemblance to the shape of the mean profile. There are large local variations in concentration level resulting in steep gradients in the radial direction. High values of concentration occur in regions way off the centerline of the flow. On the other hand, low concentration fluid or unmixed ambient fluid may be found in regions deep inside the

turbulent flow. In comparison to the jet, ambient fluid may be found in larger parcels in the plume interior. Quantitative results of the extent of ambient fluid presence are presented in Section 4.3.1. The instantaneous plume profile suggests that the concentration variations are more abrupt and occur over smaller spatial scales in the plume than in the jet. This is consistent with the higher value of the turbulence intensity computed for the plume flow. Another noteworthy feature of the plume flow is that the very high values of the concentration occur over spatially small scales, which are exhibited as narrow spikes in the instantaneous profile. From the time histories presented in the next section, it is observed that these regions of high concentration have also a small extent in the time domain.

4.2.3 The evolution of the instantaneous profile

The time evolution of the instantaneous profile may be followed from the concentration time traces presented in Figures 4.7 and 4.8. In these figures, the simultaneous concentration level, as recorded from probes at selected values of the radial similarity coordinate r/x, is plotted versus time. The horizontal time scale is normalized with the large scale time L/U_m and the local concentration values are normalized with the mean centerline value. From this display a comparison may be formed between the time histories at a given point in the jet and the plume flow region. It may be observed that, in comparison to the jet, the concentration level in the plume fluctuates

wildly between high and low values. Ambient fluid is found more frequently in the plume interior. These features are consistent with the high values of the computed concentration variance in the buoyant flow.

An effective way of presenting the time evolution of the entire instantaneous concentration profile is by employing an image array processor equipped with a high resolution monitor. Such a system (De Anza 6400) is available at GALCIT and was extensively used in this investigation for the purpose of data analysis and display. To visualize the evolution of the patterns in the flow, a large number (up to 512) of concentration profiles are successively fed into the memory of the image array processor and are displayed simultaneously as horizontal lines in the high resolution monitor (Conrac). Each scan line of the monitor depicts up to 512 individual pixels. When displaying data recorded at a resolution of 1024 pixels per Reticon array scan, one data pixel is skipped per one displayed. The monitor is capable of displaying data at 8 bits resolution per individual pixel. In other words, the full 256 level range of the data is retained. It is also possible, by setting the intensity transformation tables in the image array processor, to manipulate the red, green and blue guns of the monitor so as to assign different colors of varying intensity to different values of the concentration level. With this pseudocolor assignment the viewer is aided in identifying regions with uniform concentration since the eye is not accustomed to discerning monochrome variations of so many levels.

Pictures of the monitor, depicting the evolution of the instantaneous concentration profile at the axial distance of 150 nozzle diameters in the momentum jet, are presented in Figure 4.9. The vertical axis is time, where the 960 successive profiles of a Re = 5600 jet that are presented span approximately 39 seconds, equivalent to about 6 large scale flow times.

Based on the digital data displayed in Figure 4.9, some important features of the instantaneous concentration field in the fully developed jet flow can be discussed. It is clear that, despite the random characteristics typical of the turbulent flow, there is a certain regularity manifested in the passage of a large structure at time intervals roughly equal to T_j. The front of such a structure is marked by a spatially coherent increase in concentration level relative to that of the preceding (in time) fluid. The central region of the flow is usually at a higher concentration than the side regions, where pockets of ambient fluid are frequently found. High concentration regions are observed to sway at positions off the jet centerline. This may be suggestive of a helical structure in the main flow which, due to the limitations inherent to the present technique, cannot be documented.

These basic features were also observed in the spatially resolved still photographs presented in the previous chapter. However, the digital data presented here permit a slightly more precise statement to be made regarding the uniformity in fluid concentration at any

instant as it passes through the measuring station. The pseudocolor assignment aids the identification of three (crudely defined) levels of concentration. Fluid at the lowest concentration level marked by shades of red color is usually found at regions away from the centerline. The contours indicate that at these large radial distances fluid is relatively stagnant. It seems that fluid parcels that are ejected radially outwards will sit for some time (maybe during the passage of a large scale) before they will get re-entrained into the jet. Fluid at the middle concentration level is typically found around the central region of the instantaneous profile (not always the centerline). This is marked by yellow color. The transition from red to yellow is not always smooth, indicating a step in the concentration value. Finally, regions of highest concentration that are marked by shades of green (and occasionally blue) color are most frequently found at the upstream (front) regions of the large structures. Since at the back region of the structure the concentration level is rather low and is marked by the occasional presence of clear ambient fluid, the transition in local concentration level at the instance of the arrival of a large structure can be very sharp, indicating a steep local gradient.

The classification of the fluid states as belonging to three levels of concentration is rather arbitrary. In fact, there is a subjective aspect in this classification since there are variations of concentration level (and correspondingly of color shade and intensity) inside each color band that the photographic film may or may not pick

up. However, this classification aids in the identification of separate regions of widely varying levels of intensity. From similar data taken almost concurrently at GALCIT, Dahm (1985) concluded that the instantaneous radial profile in the far field of the jet can be fairly approximated as having either a top hat ("one level") or "two level" shape. This could be deduced from the present data if green and yellow regions are considered together. However, Dahm was not able to provide a quantitative measure of the probability of the occurence of the two individual shapes and his classification is as subjective as the present one. The inclusion of a third level in the interpretation of the present data intends to highlight the higher concentration values and steep gradients that characterize the structure fronts. Dahm did not detect such gradients in his jet data. This issue will be taken up later, along with a discussion on the representative structure shape.

For purposes of comparison, a similar image of digital data from the color monitor is presented for the buoyant plume flow in Figure 4.10. The vertical (time) axis in this case spans 960 individual array scans, corresponding to about 4 large scale times. Data were taken at an axial distance of 105 diameters from the plume source, corresponding to $x/L_M = 33$. As before, only one of every two available data pixels is actually displayed on the monitor.

It can be observed that a change in the instantaneous flow structure occurs under the action of buoyancy. In contrast to the jet

flow, it is no longer possible to identify a central "column" where concentration values are relatively uniform. The flow is very intermittent; the probability of finding unmixed ambient fluid is substantial everywhere in the interior of the plume. Even where ambient fluid is absent, local fluctuations of concentration intensity are strong (marked by the interwining of yellow ribbon-like patches in a red background). It is also evident that local concentrations occasionally reach very high levels compared to the local mean value or even the maximum mean value. These are marked by the presence of small regions of green-blue color. It should be noted that these are roughly three times the mean centerline concentration level. It is still possible, as in the jet, to identify concentration structures that convect past the measuring station at time intervals given roughly by the large scale time. Based on observations of longer time records it was concluded that, as in the jet and perhaps even more so, fluid at the highest concentration is found in the regions identifiable as the large structure "fronts." In the buoyant flow there is a direct connection between local dye concentration level and local density difference (or buoyancy force). As a consequence, regions marked with high values of dye concentration are expected to be moving faster than surrounding parcels of low dye concentration. This is consistent with the notion that the front region of the structure is its most undiluted part. It would also imply that different parts of the large structure convect at different speeds. Another difference between the entrainment mechanism of the jet and

the plume is that fluid at the boundaries of the buoyant flow does not tend to stagnate awaiting re-entrainment. In fact, observation of the smaller vortices at the plume boundaries reveals that they are overturning and thus actively entraining ambient fluid. Also, the long vertical streaks often present in the r,t digital pictures at large radial distances in the momentum flow are absent in the plume. In comparison with the jet, the overall picture suggests that eddies of a variety of scales and at different positions are capable of entraining. This is consistent with the greater dilution capability of the buoyancy driven flow compared to the momentum driven flow.

4.3 Turbulent Structure of the Concentration Field

The flow possesses a random character in the sense that neither its time evolution can be predicted by a deterministic function of time nor can the value at a particular time be predicted by an ensemble of realizations. Statistical methods are appropriate for the analysis of such random signals. In this section results based on such methods of analysis are presented.

4.3.1 Intermittency and conditional averaging

To investigate the extent of the presence of unmixed fluid at various radial positions in the flow field and determine the shape of the mean mixed profile, the following scheme is adopted. First, an

intermittency value of 0 or 1 is assigned to the instantaneous concentration value C according to

$$I(\eta,t) = 1 \text{ if } C(\eta,t) \text{ greater than threshold}$$

$$I(\eta,t) = 0 \text{ if } C(\eta,t) \text{ less or equal threshold.}$$

The intermittency profile then follows from the conventional average

$$I_m(\eta) = \frac{1}{N} \sum_{n=1}^{N} I(\eta,t).$$

The mean mixed profile is then determined from a conditional averaging scheme as

$$C_{mxd}(\eta) = \frac{1}{I_m(\eta)} \sum_{n=1}^{N} C(\eta,t)I(\eta,t).$$

It was found that the shape of the mean mixed profile and the intermittency profile were not sensitive to the value of the threshold in the range of 5% to 15% of the mean centerline value. The threshold value was arbitrarily chosen to be 10% of the mean centerline value.

The radial intermittency profile of the far field momentum jet is shown in Figure 4.11. It may be seen that, from a statistical point of view, not much ambient fluid reaches the jet centerline. Of course, the technique employed here only permits identification of unmixed fluid down to the scale that can be resolved. It is obvious that sharp interfaces between unmixed fluid and dye containing fluid

at scales smaller than the resolution limit will appear mixed to the probe. So in that sense, the intermittency estimate should be viewed as an upper limit of the true value obtained from an ideal probe that can resolve all scales. The mean mixed concentration profile in the momentum jet is shown in Figure 4.12. In comparison with the conventionally averaged profile it is much fuller, indicating the presence of high concentration fluid at radial positions off the centerline. In a way it is more representative of the instantaneous profile; however, the sharp local gradients of the instantaneous profiles are still smoothed out by the averaging procedure, and no central "column" of uniform concentration may be discerned.

The intermittency profile and mean mixed profile for the buoyant plume are shown in Figures 4.13 and 4.14. It is clear that a substantial amount of very low concentration fluid or clear ambient fluid can be found in the plume interior. The mean mixed profile in the plume is also fuller than the conventionally averaged profile. It is implied that high concentrations are common at positions off the centerline under buoyant conditions.

A similar conditional averaging procedure can be applied to the concentration variance. The purpose in this case is to estimate the contribution to the computed turbulence intensity from the presence of ambient fluid in the flow interior. The result is plotted in Figures 4.15 and 4.16. The contribution of unmixed fluid to the variance (C_{rmsc}) is overall more important in the buoyant flow and has an off

centerline peak at $\eta = 0.75$. (It should be noted that the value of the peak depends on the value of the threshold chosen, but the qualitative effect is the same.) There is a notable similarity between the turbulent structure of the momentum jet and the buoyant plume, as evidenced from these figures. Similar behavior was exhibited in the plane buoyant flow geometry investigated by Kotsovinos (1977).

4.3.2 Mean centerline dilution

The mean centerline dilution, as computed from the available measurements, is presented along with the extensive data of Papanicolaou (1984) as a function of the appropriate dimensionless distance from the flow origin in Figure 4.17a. There is an overall good agreement with previous measurements. Data for the centerline dilution in the jet are presented in Figure 4.17b, as a function of the dimensionless distance x/d. As expected, the dilution conforms to the axial decay law of Eq.(3.7) predicted from similarity considerations. No virtual origin is fitted to these data. The value of the constant in the decay law that is inferred from the present measurements is $A_c = 5.8$.

4.3.3 Radial profile of maximum concentretion

The maximum concentration C_{max} during the sampling time, made non-dimensional using the mean centerline concentration, is plotted in Figure 4.18. The profile of minimum concentration is not plotted

since it was zero throughout the radial extent of the flow. The radial boundary of the flow can be defined as the distance y/x at which the profile of maximum recorded concentration drops abruptly to zero. It is evident that the dimensionless maximum and minimum concentration depends on the the presence of buoyancy. This is also the case for the plane plume (Kotsovinos 1977). The greater spread in local concentration level is reflected in the higher values of rms turbulence intensity of the buoyant flow. It can also be observed that high concentration values (in excess of the mean centerline value) are recorded at large radial distances.

4.3.4 Probability density function for concentration

The probability density function (PDF) of dimensionless concentration is plotted in Figure 4.19a for various radial positions in the turbulent jet. The PDF is normalized by the requirement that its integral is unity. It should be noted that the shape of the concentration PDF is of interest in cases where a statistical approach is taken in problems involving the predicton of transport, mixing and chemical reactions in turbulent shear flows (e.g., Toor 1962, Pope 1980). The PDF yields a more complete representation of a random variable than the mean and rms value which are obtainable from the first and second moments of the PDF, respectively. Note that the intermittency defined in 4.3.1 can be alternatively defined in terms of the normalized concentration PDF through the integral

$$I_m(\eta) = \int_0^{\xi} PDF(\eta, \xi) d\xi$$

where $\xi = C/C_m$ is the dimensionless concentration and $\varepsilon = 0.1$. It may be observed, from the PDF shapes in Figure 19a, that the PDF is rather symmetric at the centerline, with some preference for lower values (skewness). Asymmetry is introduced at larger radial distances with progressively higher probability for the presence of ambient fluid. The position of the PDF maximum mixed value shifts gradually across the layer, in accordance with the radial profile of the mean mixed concentration of Figure 4.12.

The normalized concentration PDF at the centerline of the momentum jet flow is presented in Figure 4.19b for various values of the nondimensional axial distance from the source. From this representation, it may be observed that the PDF shape exhibits the required similarity with x/d. The normalized concentration variable may also be written in terms of the nozzle fluid concentration using Eq. (3.7), with

$$C_{norm} = \frac{C}{C_m} = \frac{(x/d)C}{A_c C_o}. \qquad (4.1)$$

It should be noted here that Dahm (1985), on the basis of of a single axial LIF measurement in the momentum jet, suggested that a normalized concentration variable that fitted his data describing the axial evolution of the PDF is given by

$$C_{norm} = \frac{(x/d)C}{C_o - C}. \qquad (4.2)$$

The differences between the variables in Eqs. (4.1) and (4.2) would be small for large values of the dimensionless axial distance x/d. On the basis of the good agreement between the PDF shapes in Figure 4.19b, the normalization of Eq. (4.1) seems appropriate. Furthermore, this normalization exhibits the required similarity that exists for the higher moments of the PDF (e.g., rms intensity). This is not the case for Eq. (4.2), which actually corresponds to an rms intensity slowly increasing with x/d, as observed in the axial experiments of Dahm. However, it may be argued that axial LIF measurements are inherently plagued by problems of non-uniform resolution (see Section 4.1.3) and are not as precise as radial LIF measurements. Indeed, at the furthest axial stations of Dahm's axial measurement, where the effective resolution is about equal to the resolution of the present experiments, the rms fluctuation he recorded reaches the values measured in the present experiments.

The PDF of normalized concentration in the plume flow field is plotted in Figure 4.20a as a function of the radial position in the layer. Large differences may be observed between the PDF of the momentum driven flow and the buoyant flow. First, the range of concentrations possible in the plume is much greater than in the jet. Second, the buoyant flow is marked by a high probability of ambient fluid presence at all locations throughout the layer. It is for both reasons that the rms fluctuation intensity (second moment of the PDF)

reaches very high values in the plume.

The normalized concentration PDF at the centerline of the buoyant plume is presented in Figure 4.20b. It may be observed that, contrary to the momentum jet flow, the most probable value is not the mean value due to the high probability of detecting fluid of small or zero concentration. The intermittency, as defined above, is observed to increase for the higher value of the dimensionless distance x/L_M. This behavior might raise the question of how the flow would behave at even higher values of x/L_M or, equivalently, whether "fully buoyant" conditions have been really attained. However, the accurate study of a buoyant jet flow at higher values of x/L_M than the values used here is experimentally very difficult and this question must be resolved by other means.

4.4 The Instantaneous Profile Center and Width

In what has been discussed so far, little use has been made of the fact that the measurements obtained in the present work are correlated in both space and time. This attribute of the measurements, that makes meaningful the digital image display of the data (Figures 4.9 and 4.10), opens the possibility for alternate ways of analyzing the physical process. It would be desirable, for example, to determine quantitatively the extent of uniformity in concentration at a certain axial location at any instant. In view of

the intermittency of the flow and the randomness expected in the time of arrival and position of the large flow scales, a stationary point probe would be clearly inadequate to answer this question. Even field measurements along a line are not quite sufficient since the flow has a three-dimensional character. Although this issue must ultimately be resolved by field measurements that yield concentration on a plane, an attempt will be made with the available data in hand. In particular, one of the questions that can be addressed is whether a different representation of the mean quantities in the flow can be obtained by making use of an instantaneous flow center, instead of the fixed center at the geometrical axis.

If the instantaneous flow pattern is observed to sway, then even if the passive scalar had a constant value but was nonuniformly distributed in space at any instant, the resulting mean profile would be of the usual bell shape type as a result of the conventional averaging procedure. Since from the present experiments it is possible to define at any instant the visual flow boundaries by some suitable criterion, a question that may be addressed is how uniform the concentration is averaged with respect to the instantaneous flow center. To this end, the instantaneous center of the flow was defined for each profile in the ensemble as the midpoint between the boundaries. For this estimate a boundary was defined as the first (or last point) along the radial direction where the local concentration exceeded 30% of the mean centerline concentration. As would be expected, the position of the flow center computed in that fashion has

an average value coincident with the geometrical center, both in the case of the momentum jet and in the buoyant plume. The variation of the position of this center has an rms value of (.025)x for the jet and (.023)x for the plume. The flow width, i.e., the distance between the computed boundaries, has an average value of (.28)x for the jet and (.24)x for the plume. The variation in width has an rms value of (.030)x for the jet and (.046)x for the plume. These values indicate that the variations in flow width are comparable to the variations of the flow center. It should be noted here that the variations in the position of the flow center that are expected to occur in the direction normal to the line of observation cannot be accounted for from the available data.

The profiles of mean and rms concentration were computed relative to the instantaneous jet center and are presented in Figure 4.21. The mean profile is considerably flatter (near the center) than the conventionally averaged profile measured with a "stationary" probe, and drops off for larger radial distance in a rather gradual manner to a second concentration level at $C/C_m = 1/4$. This leveling of the "centered" mean concentration profile occurs at about $r/x = 0.12$. The sharp drop-off at the edge of the layer to zero concentration level is notable. The "centered" profile is definitely more appropriate than the conventionally averaged profile in representing the fluid states in the momentum jet. It is plausible that a greater degree of uniformity near the center accompanied by a sharp drop-off to the lower concentration level would be exhibited, if the estimate of the

flow center incorporated the concentration pattern in the entire plane normal to the axis. For the simpler flow field of the plane jet Uberoi and Singh (1975) found that the swaying action of the entire jet column was responsible for the bell shaped form of the mean profile. With computation similar to the above, they determined that the shape of the mean profile defined with respect to the instantaneous flow center was very flat, suggesting a rather uniformly mixed state in the jet interior . A characteristic feature of their measurements however, is that they did not observe high values of intermittency (or high gradients of the scalar quantity) within the instantaneous profiles recorded by the moving hot wire probe. This may be attributed either to the low value of the Schmidt number (Sc=7 for their measurements) or to an inadequate resolution of the probe.

The representative "centered" profiles for the buoyant plume are presented in Figure 4.22. The trends are similar to the jet flow, but a distinction between two concentration levels cannot be made as clearly as in the momentum jet. This is consistent with the observations based on the transverse flow visualization photographs (Figure 3.4) and the digital images, suggesting that there is a greater variance in the position of the maxima corresponding to the large scale fronts in the plume than in the jet.

4.5 The Integral Scale of Concentration Fluctuations

In this section some results are presented that are obtained using traditional spectral techniques applied to the raw data. These include correlation functions, estimates of the integral scale of concentration fluctuations, and power spectral estimates.

4.5.1 Correlation functions

The autocorrelation function of the concentration time signal at a fixed point in space is defined as

$$R(\tau) = \overline{c(\eta,t)c(\eta,t+\tau)}$$

where τ is a variable time delay and c denotes the instantaneous fluctuation ($c(\eta,t) = C(\eta,t) - C_m(\eta)$). The cross-correlation function between time signals at two points in space is computed in a similar manner as

$$R(\tau) = \overline{c(\eta_1,t)c(\eta_2,t+\tau)}.$$

Unbiased estimates of these quantities ("unbiased" refers to the method of time averaging) can be computed directly from the raw data for selected points in the flow field. These are presented in Figure 4.23a for the momentum jet and 4.23b for the buoyant plume, as a function of the normalized time delay. All the functions are normalized with their value at zero time delay. It is observed that the large scale periodicity of the data shows up as a secondary peak for large enough values of the time delay. This peak is more

pronounced in the cross-correlation function. The general shape of the cross-correlation functions resembles that of a sine wave in broad band noise. It is surprising that the large scale frequency cannot be discerned in the correlation functions reported in the literature. It is possible that previous investigators did not extend the computation of the correlation function for long enough time delays. It is also possible that, due to the wandering of the entire jet column, simultaneous sampling with two probes that are separated by a small distance is actually necessary for the identificaton of the large scale passage frequency. In comparison to the jet, the secondary peak corresponding to the large scale passage frequency is not as pronounced in the plume, due to the increased wandering of the structures in fixed physical coordinates. The good agreement of the autocorrelation functions for small time delay in the momentum and buoyant flow presented in Figure 4.23c shows that the details of the small scale flow structure in the axial direction are independent of the large scale configuration. However, as will be shown shortly, this is not the case for the spatial correlations in the radial direction.

A correlation function that can also be computed from the data is the lateral spatial correlation for zero time delay defined as

$$R(\xi) = \overline{c(r,t)c(r+\xi,t)}.$$

Representative estimates of this function, computed at the flow

centerline at the axial station of x/d=105, are presented in Figure 4.24. As before, normalization with the value at zero spatial increment is used. Note that the nature of the data acquisition method, i.e., sequential sampling of adjacent points in space, will inevitably affect the estimates of the spatial correlation function at very large values of ξ. However, since in the worst case the time lapse between sampling at the largest separation is only .4 ms and the local convection velocity in all cases is less than 5 cm/s, it is believed that insignificant error is introduced in the estimates of the spatial correlation function for the values of separation presented here. The shape of this function indicates in a direct manner the extent of correlation of the concentration fluctuations in physical space in the radial direction. Geometrical considerations imply that it should be an even function of ξ (e.g., see Hinze 1975). For small values of ξ this is indeed the case for any point in the flow field. However, an asymmetry is inevitably introduced for large ξ when the center point is at locations off the flow centerline. This is due to the lack of homogeneity of the flow , i.e., to the existence of a preferred direction.

The shape of the spatial correlation functions reveals that the presence of buoyancy generally acts to decrease the extent of correlation in physical space. This is intimately related to the strongly intermittent character of the buoyant flow. The disagreement of the spatial correlation functions in the lateral direction for the momentum and buoyant flow is noteworthy. It suggests that the action

of buoyancy affects the small eddy structure in the lateral direction more than in the axial direction. This result is consistent with earlier qualitative observations, where it was noted that the interwining interfaces of the vortical structures with axes in the axial direction are thinner in the plume flow and are marked with fluid of high concentration.

4.5.2 Integral scales

The integral time scale of concentration fluctuations is defined through the integral

$$T = \int_0^\infty R(\tau)d\tau.$$

The lateral integral spatial scale is also defined by the corresponding relation

$$\Lambda = \int_0^\infty R(\xi)d\xi.$$

These scales were calculated from the correlation functions and their values are presented in Table 4.4.

4.5.3 Spectral estimates

The power spectrum of a turbulent signal may be obtained by a Fourier transform of the autocorrelation function. For discrete signals the numerical technique employed is the Blackman–Tukey method. This method was actually found computationally more stable than the Cooley–Tukey method which operates on the raw signal using the discrete fast Fourier transform. The latter is obviously superior in terms of computational efficiency but due to problems of aliasing, and finite record length, produced spurious results at high frequencies. In any case, the two methods are mathematically equivalent and since the autocorrelation functions were already available for large enough time delays, the Blackman–Tukey method was used and the results are presented in Figure 4.25a for the momentum jet and the buoyant plume. The spectra are normalized by their integral over wavenumbers, which corresponds to the mean square value of the raw signal. The frequency is normalized by the large scale time.

Spectral estimates that are measured and reported in the literature are usually based on the raw time signal of a fluctuating quantity and thus are actually estimates in frequency space. These are converted to spectral estimates in wavenumber space by the transformation $x=U_c/t$, corresponding with a "frozen" pattern of turbulence convecting past the stationary probe. Since the present data afford the luxury of direct estimates in wavenumber space, these were obtained from the spatial correlation functions and are presented

in Figure 4.25b for the momentum and buoyant flow. The wavenumber scale is normalized with the lateral extent of the flow L.

A general feature of the spectral estimates is the existence of a small region in wavenumber space where the spectral density falls off with a -5/3 power law (as predicted by Kolmogorov). However, the lack of a significant variance in the spectral density, especially at the high wavenumbers where the flows are so markedly different, is discouraging. It indicates that such spectral estimates will inherently yield a poor representation of the flow properties, being too far removed (by computations) from the physical process.

4.6 The Large Scale Features of the Concentration Pattern

The photographs presented in Section 3.2 and the digital images of the type shown in Figures 4.9 and 4.10 suggest that the dimension of the large structure is comparable to the local flow width, and that it convects with the local convection velocity. It should be mentioned here that Sreenivasan et al. (1979) analyzed thoroughly the temperature and velocity time traces in a slightly heated turbulent air jet. Based on an ensemble averaging procedure they found that ramp-like structures in the temperature (tracer) signal, whose time extent was comparable to the large scale time of the flow, were statistically significant and caused a breakdown of local isotropy. It is natural to associate these large scale patterns with the signature of the large scale structure observed in the far field jet

flow. Furthermore, a comparison between gas phase and liquid phase jets is of interest, because of the anticipated effects of the Schmidt number in the molecular mixing process.

For these reasons, a conceptually similar analysis of the concentration time traces was undertaken for the flows considered in the present investigation. To this end, the concentration time signal was processed by the ensemble averaging technique of Sreenivasan et al., which is outlined here. The duration (time interval) between two succesive instants, at which the signal exceeds, during an upcrossing, and falls below, during the subsequent downcrossing, a preset threshold is determined first. If the duration lies within the range of interest, the amplitude level of the signal is obtained, by interpolation if necessary, at S equally spaced points within the excursion. (For convenience, S is chosen as the ratio of the mean duration over the sampling interval.) A subsequent excursion in the same range of duration is treated similarly, and the amplitudes at the S points are added to the previous set of values at the corresponding locations. The ensemble average shape, denoted by $\langle\ \rangle$, is obtained by dividing the sum at each of the S points by the total number N of excursions belonging to the chosen range of duration. For convenience, the expression "duration $\bar{T}$," will be used to signify "range of duration centered about $\bar{T}$," where $\bar{T}$ denotes the arithmetic mean of the extreme values of the chosen range. The interval $\Delta\bar{T}$ used for selecting members of the ensemble is $0.2\bar{T}$. Concentration traces corresponding to several neighboring points were used to form each

ensemble average. This not only improves the convergence of the mean shape, but also makes the computed ensemble average more representative of the average concentration pattern in the large structure. For the purpose of the present analysis, two different probability density functions were obtained for the ensemble. One PDF was computed for concentration values occurring for the first half of the ensemble shape, and the second PDF for the trailing half.

Representative ensemble shapes as computed by this procedure are presented in Figure 4.26a. Normalization is performed with the conventionally time-averaged concentration value at the same radial location in the layer. It should be noted that for small values of the normalized duration the ensemble average shape is symmetrical, whereas for durations comparable to the large scale time an asymmetry is introduced. The effect of using a large number of neighboring points (middle curve) for the ensemble is to smooth the ensemble shape and slightly reduce the front to back gradient. The resulting large structure shape exhibits the characteristics that are observed in the digital display images such as Figure 4.9. The concentration value is thus observed to rise in an abrupt manner in the (downstream) front, while it slopes more gradually in the (upstream) back regions. These results are in qualitative agreement with the structures observed by Sreenivasan et al. in the gas phase co-flowing jet. A quantitative difference is that, in the present case, the average concentration gradient in the structure is generally smaller. Since part of the ensemble averaged structure shape results from the increased

(intermittent) presence of ambient fluid in the back regions, the two separate PDF's are also presented in Figure 4.26b for a clarification of this issue. These correspond to the case of averaging over a large number of neighboring pixels (middle curve of 4.26a) where some smoothing occurs. It is observed that the front-region PDF peaks at a higher concentration than the back-region PDF. This establishes that in the front regions of the structures there is a higher probability for the occurrence of high concentration fluid. Finally, the analogous results for the buoyant plume are presented in Figure 4.27. It may be observed that the large structure pattern in the buoyancy driven flow displays, in the ensemble average sense, similar qualitative features as in the momentum flow.

The time evolution of the large structures in the concentration field as recorded by the axial LIF measurements is presented in Figure 4.28a and 4.28b for the jet and plume flow, respectively. These are digital images of (x,t) traces of the instantaneous concentration pattern on the flow axis, spanning the range $0 < x/d < 118$. A total of 960 individual axial profiles are displayed, spanning a duration of approximately 39 seconds. The flow source is on the far right of the pictures. The local instantaneous jet fluid concentration is normalized by its local time-averaged value. This normalization, in conjunction with the monochrome color assignment employed, aids the identification of fluid regions of unusually high or low local concentration. It may be observed that in both flows, streaks of high intensity alternate between streaks of low (or zero) intensity. This

is a further piece of evidence for the large scale periodicity present at all axial distances in both flows.

The paths in (x,t) space are different in the jet and the plume flow. In the momentum jet, the parabolic behavior suggested by Eq. (3.20) is observed to be followed only in the mean, while the trajectories appear piecewise linear. The implication is that individual structures convect with essentially uniform speed between interactions, and that it is these interactions that are largely responsible for the change of speed (i.e., the change of slope in the x,t diagram). This is generally consistent with the earlier observations of Dimotakis, Miake-Lye and Papantoniou (1983) and Dahm (1985) in momentum jet flows. In the buoyancy driven flow, the trajectories have an almost linear behavior in the mean, as suggested by Eq. (3.22). Based on the limited region of trajectories near the flow source that exhibit a parabolic behavior, it is observed that the transition from jetlike to plumelike flow is completed within a few nozzle diameters, as predicted in the discussion leading to Eq. (3.16). The piecewise linearity of fluid parcel trajectories is even more pronounced in the buoyancy driven flow. It is noteworthy that in both flows structures are observed to convect unchanged for very large axial distances. Finally, the degree of presence of ambient fluid (zero intensity) is confirmed to be much higher everywhere in the interior of the buoyancy driven flow than in the momentum driven flow.

CHAPTER 5

DISCUSSION

5.1 Organized Mixing in the Far Field of Buoyant Jets

From the results of the present investigation it is established that the entrainment mechanism in the buoyant jet flow is dominated by large scale vortical motions. These large scales are capable of transporting ambient fluid in significant quantities, deep into regions in the flow interior where it is subsequently mixed (molecularly) by a shearing action of smaller eddies. The instantaneous concentration pattern observed in the flow under study, shows that the entrainment mechanism cannot be viewed in terms of a "diffusive propagation" of the interface between "turbulent" and "non-turbulent" fluid. In addition, results of the present investigation are generally at variance with any flow modelling schemes that obtain closure of the equations of motion by employing eddy-diffusivity and gradient transport concepts to problems of scalar transport and tubulent mixing.

It is observed on the basis of flow visualization and the results of Section 4.5.1 that both the momentum jet and the buoyancy driven plume exhibit a periodicity associated with the passage of large scale flow structures. (The present results concerning the momentum jet flow are in qualitative agreement with the results of Dahm (1985) for the far field momentum jet). Therefore, it is suggested that the large scale flow organization depends only on the local large length

and time scales, and not on the nature of the driving force. Despite the observed similarity in the large scale structure of the concentration field, it is to be expected that since the flow evolution is markedly different in each case as a function of the axial distance, the effect of buoyancy causes significant differences in the instantaneous concentration pattern and in the details of the entrainment process. The significant features of the entrainment mechanism in the far field buoyant jet are discussed in the following paragraphs.

In the momentum driven jet, a central conical region may be identified where the time-averaged local concentration is relatively uniform and, generally, at a higher concentration than that of the surrounding jet fluid. At any fixed axial location, flow visualization in a transverse plane and the time evolution of the instantaneous radial profile reveal that the cross-sectional area of this region changes shape in a cyclical manner, growing from an initially small region around the center to a region encompassing the entire flow extent. Since this cyclic phenomenon has a period equal to the large scale period L/U, it is considered to be the signature of the large scale structure. Similarity requires that this flow structure have the same features at any axial location as long as the driving forces maintain their balance. The process of entrainment is associated with the continuous engulfment of pockets of ambient fluid of various sizes from the side and back regions of the structure (in a Lagrangian frame). The conditional velocity measurements performed by

Sreenivasan et al. (1979) suggest that these structures possess coherent vorticity in the axial direction. This vorticity would cause the entrainment of ambient fluid mainly from the back regions (in large tongues). On the other hand, the lack of azimuthal coherence of these tongues would suggest that this axial vorticity is not very strong or very coherent. Flow visualization in a transverse plane reveals that smaller, strongly three-dimensional eddies (with vorticity vector in the radial direction) are also responsible for the immediate engulfment of ambient fluid. This process is analogous to the plane shear layer where the secondary (longitudinal) vortex structure results to higher values of entrainment and enhanced mixing as has been observed by Breidenthal (1982) and Bernal (1981).

At any axial location, the highest local concentrations are associated with the time instant of the arrival of a large structure front. This was qualitatively observed from digital flow images as in Figure 4.9, and was demonstrated in a quantitative fashion by means of an ensemble averaging procedure presented in Section 4.6. These results agree qualitatively with the results of Sreenivasan et al. (1979) for a gas phase momentum jet, although the degree of concentration gradient in the axial direction is observed to be smaller for the liquid phase jet.

The mean local concentration at a point in space is formed in a probabilistic manner by the presence of fluid parcels at a variety of concentration levels. The range of possible concentrations in the

momentum jet extends from unmixed fluid to about twice the local mean maximum value, in general agreement with the results of previous investigations. This range is considerably narrower than the range of possible concentrations in the buoyant plume.

The large scale buoyant plume structure may be thought of as a buoyant vortex ring, with a large scale passage periodicity given by by L/U as in the momentum jet flow. This structure is observed to possess a front region of very high concentration. The relation of local concentration values to the local density difference and hence to the buoyancy force implies that the downstream region moves faster than the rest of the structure and that the entrainment and mixing proceed primarily from the side and back regions. It may be also suggested that pressure forces, related to the acceleration of the buoyant structure, play an increased role in bringing ambient fluid in the flow interior through the back regions. It is observed that the variance in the position of arrival of a large scale structure increases under buoyant conditions. This results in a motion that may be associated with the visually observed puffiness of the entire plume column. The large scale plume structure should be structurally and dynamically similar to the buoyant ring considered by Middleton (1975) for his model of a plume cap. In this model, the entrainment into the cap takes place primarily from the rear region.

5.2 Effects of Buoyancy on Entrainment and Mixing

The dimensional arguments presented in Section 3.1, along with previous measurements confirmed by the present results, imply that the entrainment mechanism is much more efficient in the buoyancy driven flow than in the momentum driven flow. The present study offers an internal view of this efficient entrainment mechanism. Flow visualization in a transverse plane reveals vortical structures (of dimensions 1/5 to 1/10 of the large scale L) with the vorticity vector along the radial direction to be active in the engulfment and molecular mixing of ambient fluid. During their roll up, thin strained filaments with very high local concentrations are brought together with clean ambient fluid. The quantitative data show that local concentration values in these strained filaments may reach values as high as 4 times the local mean maximum value. A qualitatively similar mechanism is in action in the momentum jet. However, in the buoyant flow, an eddy containing fluid emanating from the flow source will possess a dynamic of its own, as directed by its own buoyant force; therefore, it is capable of generating shear, entraining and mixing ambient fluid. It is the interaction of a variety of such eddies with the large structure that displays the time averaged plume behavior. The present measurements reveal that the buoyant flow is markedly more intermittent than the momentum flow. This is associated with a more pronounced wandering of the central part of the plume column than in the jet, and with the stronger eddying motions. The higher value for the probability of detection of

ambient fluid in the plume interior is associated with the greater entrainment rate in the buoyant flow compared to the momentum flow. It is also responsible, in part, for the high values of the rms fluctuations observed in the plume flow.

In the foregoing discussion, it should be emphasized that the present results indicate that the effects of buoyancy are felt primarily at scales smaller than the large scale of the flow. A direct calculation of the spatial correlation in the concentration field in Section 4.5 reveals that buoyancy acts to decrease the degree of spatial correlation in the direction normal to the direction of gravity. On the other hand, the calculations show that scales are left largely unaffected along the direction that buoyancy forces act. Therefore, it is implied that there is a lack of homogeneity in the plume flow even at small scales, with the preferential direction being the direction of gravity. The overall effect of buoyancy is more pronounced at the small scales of the flow.

An important feature of both the momentum driven and buoyancy driven flows that were investigated is the strongly intermittent character of the concentration field. The intermittency of the buoyant plume is found to be very significant across the entire radial extent of the flow region. The description of transport processes by means of differential equations that utilize gradient diffusion concepts presupposes continuity of the turbulence in the entire region considered. It has been demonstrated that this is not the case, and

that the deviation from such uniformity is dramatic for the buoyant flow. Therefore, it is suggested that models that will incorporate the large scale organization observed in the flow are more appropriate for the description of the transport process.

CHAPTER 6

CONCLUSIONS

The present experiments have investigated the mechanism of entrainment, transport and scalar mixing in the far field of steady axisymmetric buoyant jets issuing into an unconfined, quiescent and uniform medium. The experimental method of laser-induced fluorescence was used for the direct observations of the entrainment pattern at selected planes in the flow region. The same method, coupled with high resolution linear photodiode array imaging and high speed data acquisition techniques developed during the course of the investigation, allowed the acquisition of a large number of instantaneous concentration profiles. These quantitative measurements offer a high degree of spatial and temporal resolution. Experiments were conducted for the case of the pure momentum jet up to distances of 150 nozzle diameters from the exit plane, and for Reynolds number up to 9000. For the buoyant plume, experiments were carried in the far field region (up to 105 nozzle diameters) where the flow is entirely driven by buoyancy forces. A summary of the results is presented below:

1. In both the momentum driven jet and the buoyancy driven plume, there exists a large structure organization of the concentration field. The fundamental periodicity of the large scale passage is determined by the local convection velocity and the radial flow extent.

2. The large scale structure typically posseses a characteristically

sharp concentration front. At any location, local maxima of the concentration are associated with the time instant of the arrival of the large structure. A high degree of spatial coherence is exhibited by the concentration fronts and the associated structures. As a result, the decrease in scalar concentration along the axial direction is being achieved in discrete steps rather than in the continuous fashion indicated by the similarity decay laws.

3. The scalar concentration is found to be decreasing in the mean from the front (downstream), toward the back regions of the structure. This result is consistent with previous observations in low Schmidt number (gas phase) momentum jets, although the gradient in the axial direction is found to be smaller in the present case of liquid phase jets.

4. Unmixed ambient fluid is transported deep into regions in the flow interior by large scale vortical motions, primarily from the side and back regions of the structures. Smaller, highly three-dimensional vortical structures in the flow interior participate in the molecular mixing process; these structures are more intense in the buoyancy driven flow.

5. The instantaneous concentration profile has a shape dominated by the intermittent presence of the ambient fluid in the flow interior, resulting in steep concentration gradients. These gradients are observed to increase under buoyant conditions. The mean profile is therefore not representative of the instantaneous condition.

A mean profile centered on an instantaneous flow center is found to be more appropriate in representing the mixed states in the interior of the momentum jet flow.

6. The probability of detecting ambient fluid anywhere in the flow interior is greatly increased under the action of buoyancy. The variations in local concentration level are also increased under buoyant conditions. As a result, the concentration variance in the buoyant flow is about twice that in the momentum flow. This is a direct manifestation of the efficiency of the entrainment mechanism in the buoyancy driven flow.

7. The action of buoyancy affects primarily the small scale structure, acting in general to decrease the degree of spatial correlation in a direction normal to the direction of gravity. It was found that the degree of correlation in the direction of action of gravity is largely unaffected by the presence of buoyancy.

8. The probability density function of the jet fluid concentration, when properly normalized with the local mean concentration, is self-similar along the axial direction. This indicates the general self-preservation and similarity of the flow in the far field. Self-preservation in the development of both the momentum jet and the buoyant plume flows is exhibited by the axial variation of both the time-averaged and rms concentration, as well as the axial evolution of the shape of the time-averaged profiles.

9. The basic entrainment concepts suggested from the present measurement of highly resolved instantaneous concentration profiles are at variance with concepts of entrainment and mixing based on gradient transport models. It is suggested that models that will incorporate the large scale organization observed in the flow are more appropriate for the description of turbulent transport and mixing processes.

APPENDIX A

Data Acquisition System

In this appendix we present a brief overview of the basic components of the high speed data acquisition system that enabled the recording of large amounts of fluorescence intensity data. The components of this system are the linear photodiode array camera (EG&G Reticon Corp. Model LC300A), a high speed A/D device (ADC), and the laboratory minicomputer with the hard disk storage device. A brief description of the computer program that controlled the data acquisition is also included in this appendix.

A.1 Reticon Array Camera

The LC300A camera is similar in size and operation with an ordinary photographic camera with the exception that the film is replaced by a linear photodiode array (RL1024G) and its associated electronic circuitry. The RL1024G array consists of 1024 diodes (pixels) placed in a single row with center-to-center spacing of 25 microns. Each photodiode has an associated storage capacitor (which integrates the photocurrent), and a MOS multiplex switch for periodic readout via a shift register scanning circuit. There is a second row of dummy diodes with their associated capacitors and switches. The dummy diodes are read out differentially with the photodiodes to allow cancellation of the multiplex switching transients. The array is

operated in the charge storage mode, requiring a single-phase TTL clock to drive the scanning circuit. A periodic start pulse initiates each array scan. The blanking time (interval between the end of a scan and the beginning of the next scan) may be independently adjusted. The pixel-to-pixel sampling rate is the input clock frequency and the total time between scans is the interval between start pulses. During the time between scans (line scan time) the charge stored by the circuit on the capacitor of each photodiode is gradually removed by photocurrent. The photocurrent is the product of the diode sensitivity and the incident light intensity. The total charge removed from each cell is the integrated (over the line scan time) photocurrent. The array is thus an integrating device, the charge output of each photodiode being proportional to the exposure, i.e., light intensity times the scan time. Each individual photodiode exhibits linearity up to saturation, but response nonuniformity over the length of the array is of the order of +/-14%.

The electronic circuit internal to the array camera amplifies the video output of the array, and uses a sample and hold circuit to output a Video S/H analog signal (range 0-1 Volts) synchronized with the input TTL clock. It also outputs a TTL signal (SYNC) synchronous with the start pulse that initiates each scan.

A.1.1 Resolution and dynamic range

The image resolution of the array has a static and a dynamic component. The effective resolution is the larger of the two

components. The static component is determined by the effective aperture of the pixel (16 microns) and the magnification ratio of the imaging optics. Thus, for a magnification ratio of 1/15 that was typically used, the static resolution in the image plane is 375 x 390 microns. The resolution in the third direction is determined by the laser beam diameter, which is much smaller than the depth of field of the imaging optics. The dynamic component of resolution is determined by the distance the object moves in the object plane during the scan time. Thus, for a scan time of 10ms and a mean flow velocity of 4cm/sec, the dynamic component becomes equal to the static component calculated above. It is desirable to use a sufficiently small scan time so that, for the flow under consideration, the effective resolution is about equal to the static resolution of the experiment. The effective resolution of the measurements depended on the actual experimental conditions (Reynolds number, scan time and magnification ratio) and is noted in the tables desrcibing the experimental settings for the measurements.

The dynamic range of the array is determined by the dark noise level. The dark noise voltage output level of the array increases with the line scan time, being a maximum of 10 mV at a scan time of 40 ms. For the scan times used in the experiments, the dark noise voltage level (measured with the array in the dark) was less than 4 mV peak to peak corresponding to a dynamic range of 250/1.

A.2 The ADC

The ADC is a high speed single channel A/D device, designed to interface the Reticon array camera to a direct memory access (DMA) port of a PDP11 minicomputer. It is based on the TDC1001 A/D chip which is capable of 8-bit conversions at a rate of 2.5 MHz. The ADC is configured to digitize the input video S/H signal at a fixed rate of 2.2 MHz. An on-board 20 MHz oscillator clock (Vectron CO-234), featuring excellent stability characteristics, provides timing for the A/D chip. Settings at the front-end section of the ADC allow division of the number of digitized pixels per Reticon array scan by a power of two. Additionally, a similar freedom is allowed for in the transmission of scans to the host computer. The clock timing pulse for the Reticon array circuitry and the SYNC output signal from the array are used to generate internally the CONVERT pulse for the A/D. Two digitized values (16 bits of data) are set up for transmission at a time to the DMA port of the host computer. The ADC can handle the data rate corresponding to the maximum array clocking rate (800KHz). Note that this rate is within the capabilities of the computer bus (Unibus) if all other devices are silenced, with the input DMA operating in burst mode. This allows the transmission of about 192 KBytes of data to the computer memory. However, the device is usually operated at a lower rate with the input DMA sharing cycles, thus permitting the continuous recording of data to disk.

Various procedures were used to test and calibrate the device.

These included digitization and acquisition of known voltage levels to determine linearity, and fast varying waves to determine overall response. It was also tested against a calibrated instrument by feeding the output of the Reticon array camera to both the ADC and the 12-bit AD11-K of the host computer, both being sampled at the same time (up to 80 KHz). Linearity was excellent and the response was well within the specifications of the TDC1001 chip. Furthermore, no drift was observed during a year period.

A brief description of the circuitry of the ADC is presented in the next section along with a schematic diagram. The purpose of this description is to aid future researchers in performing data acquisition at high data rates, for verification of the present results or experimentation in similar areas. Some of the features built into the ADC are system dependent, but the overall concept is rather simple and general enough to be usable for a variety of applications.

A.2.1 Circuit description

The ADC circuitry is mounted on two boards. A small board houses the analog section and has a ground plane to improve noise immunity. It is mounted on top of the larger board that houses the digital circuitry. The digital and analog sections are powered from two different power supplies. The circuitry is logically divided in three sections. In the first section (Figure A2.1) the start-convert signal

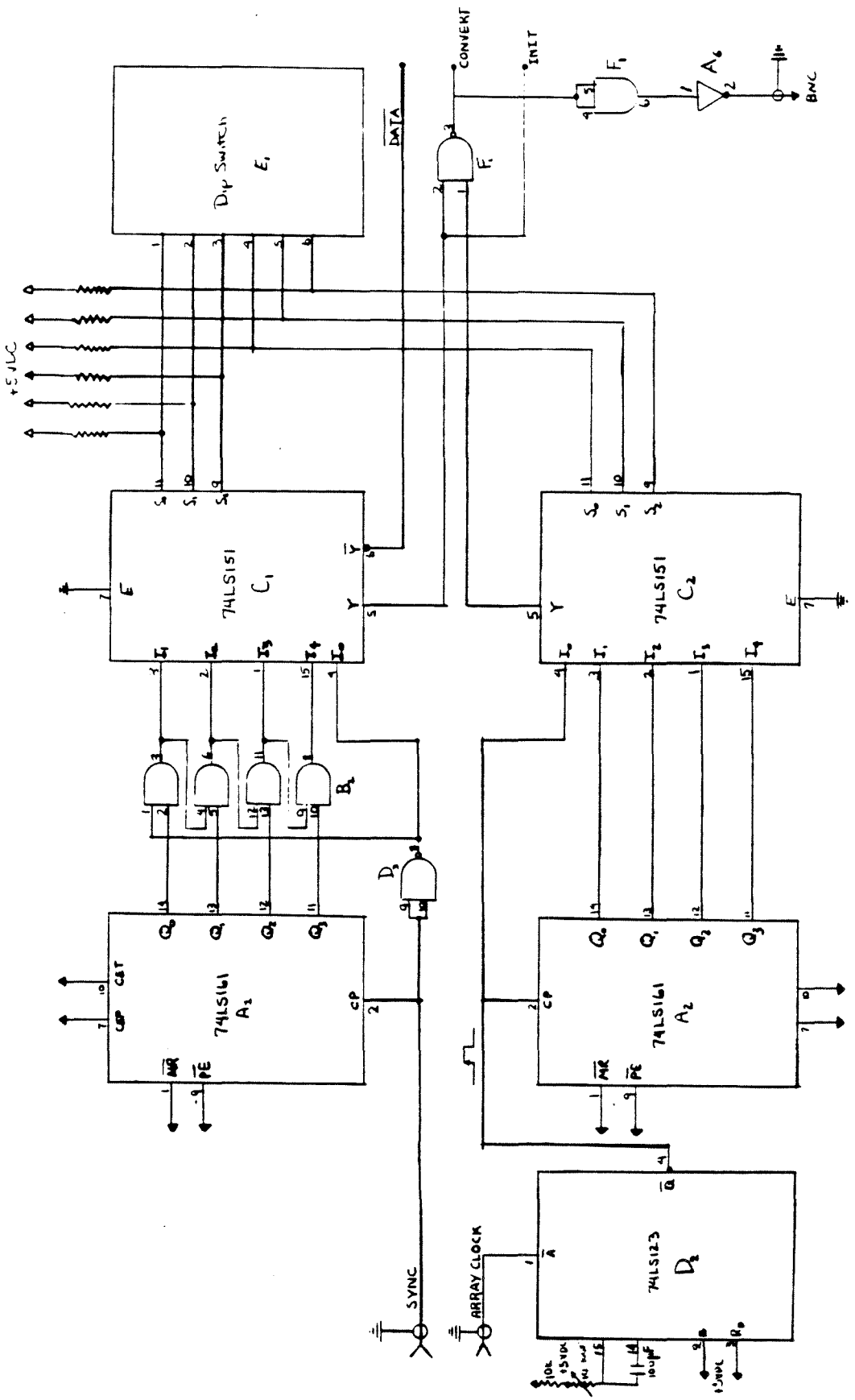

Figure A2.1. ADC circuitry, part I.

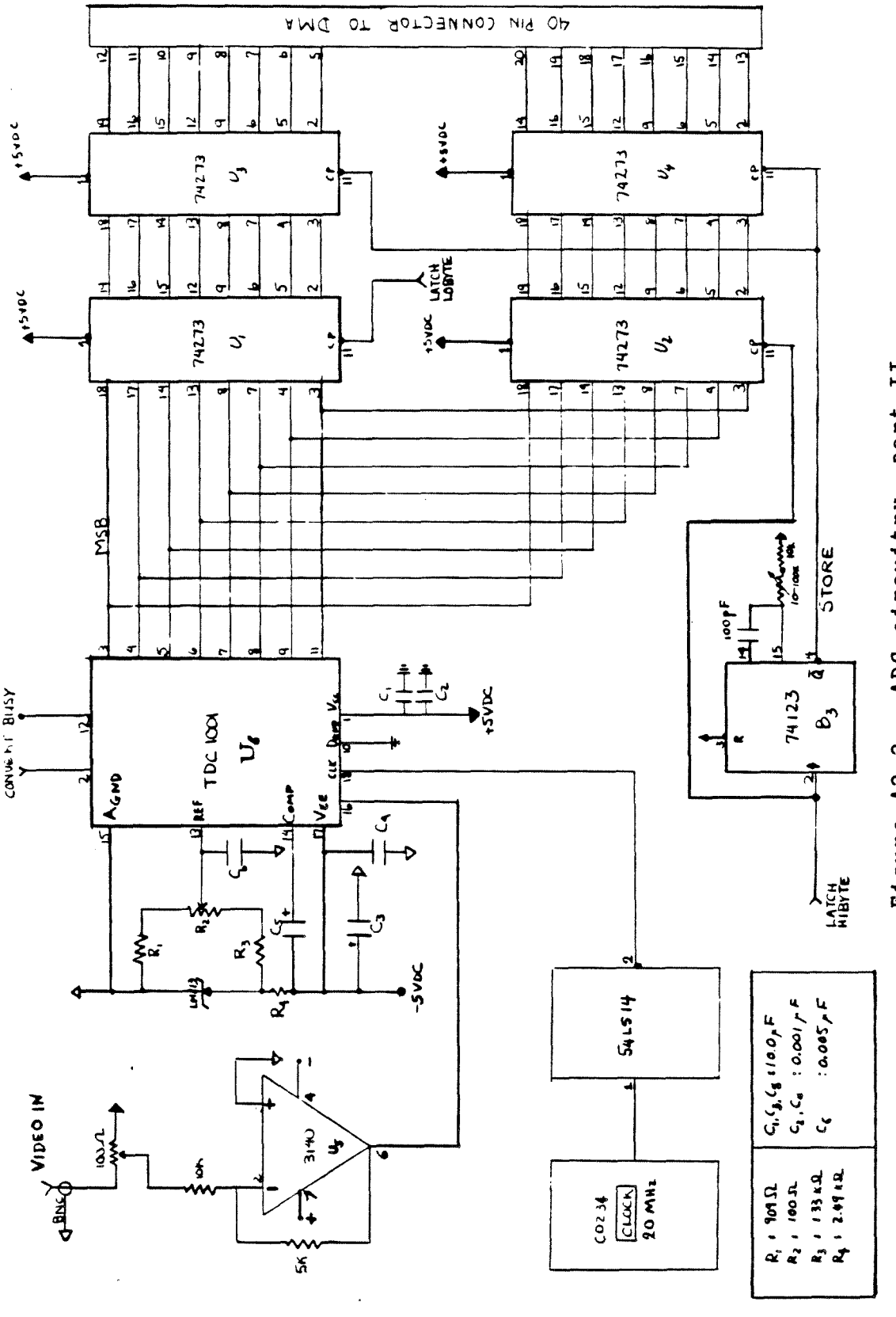

Figure A2.2. ADC circuitry, part II.

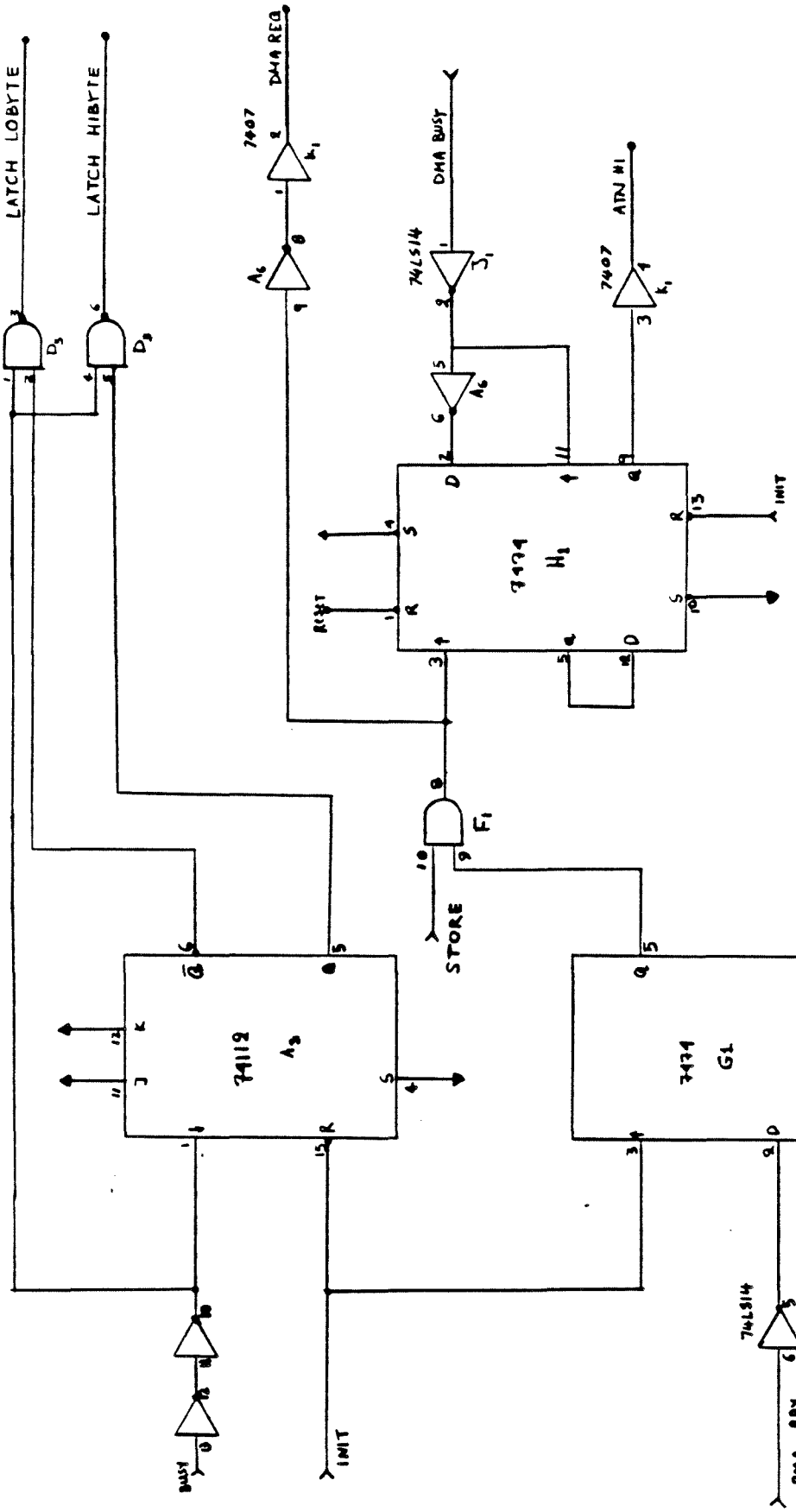

Figure A2.3. ADC circuitry, part III.

for the on-board A/D chip is generated. The external ARRAY CLOCK (delayed appropriately) and the SYNC output pulse from the Reticon array camera are fed to two synchronous counters. The preselected outputs of these counters are shaped and logically anded to produce the CONVERT pulse.

The second section comprises the analog signal shaping and the A/D conversion (Figure A2.2). The S/H video signal output of the array is negatively amplified to match the input voltage range of the A/D (-0.5 to 0.0 Volts). The 20 MHz clock that times the A/D is physically isolated from the rest of the circuit, being separately mounted in a small box. A Schmitt trigger buffer is used to electrically isolate the clock and keep noise in the rest of the circuit at a very low level. The TDC1001 output data lines are sequentially latched on two stages of D flip-flop type latches. The outputs of the second stage latches are connected to the 16 input lines of the DR11-B DMA. Two 8 bit words are set up for transmission at a time to the host computer.

The third section (Figure A2.3) consists of the logic necessary to interface to the PDP11 Unibus through the DR11-B port. The BUSY output signal of the A/D at the end of each conversion clocks a flip-flop to produce (with an appropriate delay) the LATCH LOBYTE and LATCH HIBYTE signals for the first stage latching. After the second conversion is completed, data are moved over to the second latch stage after a small delay and, if transmission to the host is enabled, a DMA

REQ signal is sent to the DR11-B. Data from the two conversions are held on the lines during the duration of the DATI bus cycle. The end of the bus cycle is monitored by the negative transition of the CYCLE pulse which is provided by the DR11-B. Since the device can digitize faster than the Unibus can transfer the data, care must be taken to avoid data overrun. To ensure data integrity, an error signal is generated (ATN HI) if the next conversion finishes before the end of the DMA input cycle. This condition generates an interrupt via the DR11-B and disables further transmission of data. The data acquisition sequence is initiated by the DMA RDY pulse from the DR11-B, which is under program control. The data transmission starts at the beginning of a scan.

The signals from the Reticon array are input to the ADC via front panel BNC connectors. Selections for the division of the input SYNC and CLOCK pulses is achieved by a front panel DIP switch. Other output signals from the ADC available through front panel BNC connectors are the CONVERT and DATA pulses. These signals are used to synchronize the data acquisition from the Reticon array with other external events. In particular, the DATA signal was used to trigger the conversions of channel 0 of the AD11-K board synchronously with array scans.

In the design of the ADC some generality was sacrificed for simplicity. The resulting effectiveness/cost ratio of this device is quite high. In the case that a much faster (next generation) computer

bus will allow the transmission of large amounts of digital data to a dedicated memory bank or a high speed disk, improvements would include the addition of a fast FIFO stage to temporarily store some data on board. This can be easily added and would take some load off the rest of such a (fast) system. For the current applications as part of the present data acquisition system with the Reticon array camera, the two stage output latching proved to be more than adequate. Finally, it should be noted that although it is not designed to be a general purpose high speed A/D channel, it may be used as such if an external start is provided for the digitization and a synchronization pulse for the orderly transmission of data. In such a case, the input analog signal should also not require a S/H circuit (which is not available on the ADC). For many applications this is unlikely to be required since the analog signal must be held at levels for only 45 ns.

A.3 Programming for High Speed Data Acquisition

The material presented in this section is presented for the purpose of aiding future experimental researchers with the difficulties associated with high speed data acquisition requirements. Programming practices, to the experience of the author, become important when the data rates that must be sustained by the system are comparable with the limits imposed by the hardware components of the system. In such cases, higher level computer languages for all their convenience are very inefficient (because of the associated overhead) and programming must rely on assembly language routines, somewhat

tailored to the appropriate hardware of the system.

A data acquisition process may be viewed as comprising of two synchronous processes: data input from a device and data output to another device. Data are routed through the computer bus to memory, which is accessible to DMA devices and to the CPU. Memory buffers serve as temporary data storage areas. (If enough memory is available to store all the data to be acquired, then the output device is the memory itself but we will not consider this case here.) A multiple buffering scheme is essential for accomodating high data rates. It should be realized that the maximum system throughput under any scheme is limited by the throughput of the slowest device on the system. Thus, the throughput rate must be maintained slightly below this level and the program should be structured so that it treats the slowest device as being able to keep up. It is believed that for maximum performance only two buffers should be used since a queue scheme increases system overhead. Device interrupts should be carefully controlled and interrupt routines should be kept very small. High throughput is possible only if both processes are using direct memory access; the alternative presented by direct I/O is inadequate since it ties down the CPU resources. In the case that both processes are fast DMA processes, the limit is placed by the speed of the computer bus. Under these circumstances, the maximum possible rate is about 1/2 of the bus bandwidth but careful programming is necessary to realize it.

The basic components of the minicomputer based data acquisition

system are shown in Figure 2.9. The PDP11/60 is a fast processor with cache memory and 256 Kbytes of main memory, running under the RT11 v.4 operating system. The AD11-K is an 8 channel A/D converter, capable of 12-bit conversions at a rate of 90 KHz (single channel). The DR11-B digital interface is a direct memory access port, capable of a data transfer rate of 1Mbyte/s in burst mode. This limit is placed by the maximum rate attainable by the computer bus (Unibus). The hard disk storage consists of a 7.2 Mbyte Winchester disk (DSD880). This is a rather outdated device, having a burst transfer rate of 500 Kbytes/s within a track, but a maximum rating of 120 Kbytes/s across the entire disk. Since it is the slowest device on the system, the data acquisition program had to be tailored so that it would optimize the disk output rate. It was in fact possible, by directly programming the disc controller to exceed its rated output speed by 10%.

The data acquisition was based on an assembly language subroutine that synchronized the two high-speed DMA processes (input from the ADC and output to disk). This program also sampled the 3 AD11-K channels synchronously with the input array sweeps. The AD11-K was started externally, using the negative transition of the DATA pulse provided by the ADC. The input process was initiated under program control by the setting of the GO bit in the DR11-B. Two 64 Kbyte memory buffers were used to store the data temporarily. This allowed the transfer of 64 full array scans at a time, thereby increasing (slightly) the system throughput. Synchronization in this double buffering scheme

was accomplished by controlling the device interrupts. Each device was programmed to interrupt the processor only when its operation on the buffer was finished, or if an error condition developed. The disk transfers were optimized by utilizing the disk controller's capability of performing spiral writes with implied seeks. The data were thus sequentially written in a disk area reserved for the acquisition output. It could be accessed afterwards in a regular fashion (as a file) and transferred for storage on a magnetic tape. The total time taken for the acquisition process was recorded by the KW11-K programmable clock. Since the actual time taken was a known multiple of the array clock period, a comparison with the time measured by the KW11-K clock provided an independent check of the data integrity.

APPENDIX B

LIF DATA REDUCTION

B.1 Laser Beam Attenuation by the Dye

The main features of Fluorescein dye relating to the LIF measuring technique are discussed by Robben et al. (1976) and Koochesfahani (1984) and will not be reproduced here. The absorption spectrum peaks at 488 nm (blue line) and the emission peaks at 525 nm (green-yellow). It was determined that optimum operation was obtained when exciting the dye with the blue laser line while allowing part of the green fluorescent light (and all the yellow) to be recorded by the array. Since the laser beam is traversing a medium that contains dye molecules, absorption of photons that are responsible for the dye excitation causes attenuation of the laser power along the beam path. Quantitatively, for a beam traversing a medium of non-uniform dye concentration, we may write an expression for the beam intensity I along the direction of propagation y as

$$I(y) = I(y_o)e^{-\int_o^y \varepsilon c(\xi)d\xi}$$

where ε is the attenuation parameter and c is the molar concentration of the dye. The attenuation parameter is a function of the excitation frequency and it was measured in a straightforward manner. A small vessel filled with a solution of Fluorescein dye (which was being continuously stirred) was placed in the path of the laser beam. The

input I_o and output I(L) beam power was measured with a power meter for various molar dye concentrations. From these data, the quantity $-1/L \ln [I(L)/I_o]$ was computed and is plotted versus dye molar concentration in Figure B.1. From this measurement it is indicated that the value of the attenuation parameter is .005 /cm 10^{-7} molar for the operating conditions used in the experiments.

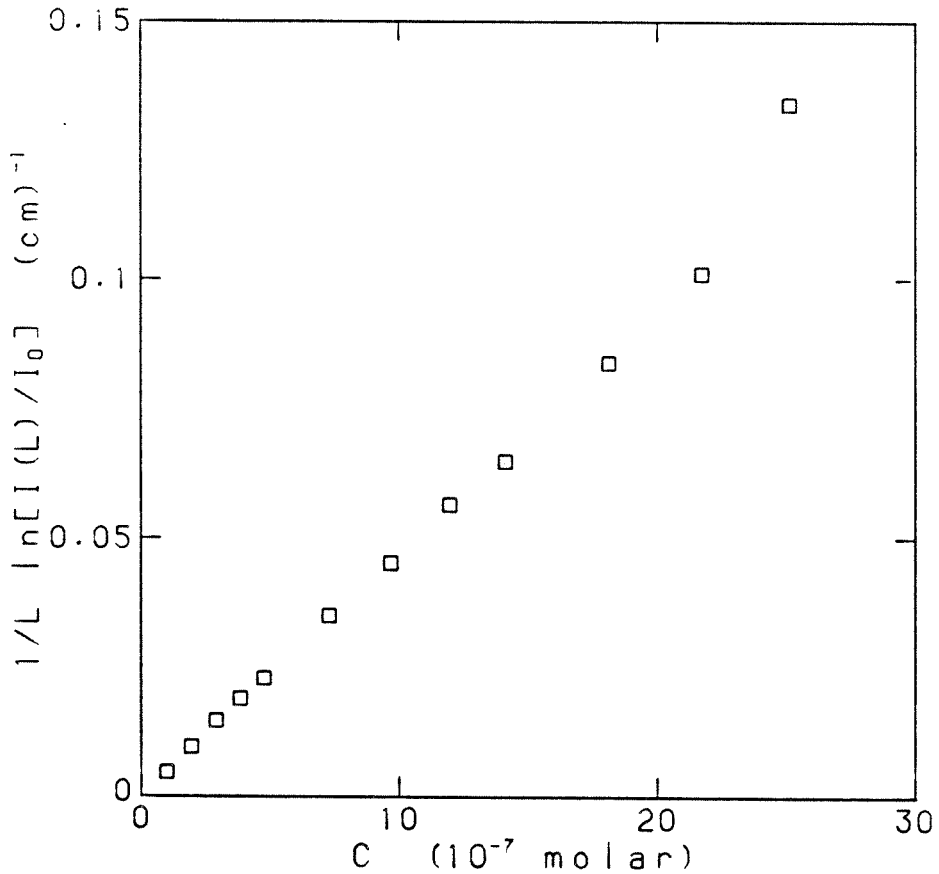

Fig. B.1 Experimental determination of the attenuation parameter for the Fluorescein dye

B.2 Conversion of Fluorescence Data to Concentration Data

The method used to convert the instantaneous fluorescence data to concentration data is based on a procedure similar to the one used by Koochesfahani (1984). In essence, this procedure relies on the use of an overall optical transfer function which includes the response nonuniformities of the array, possible misalignment of the entire optical system, and the nonuniformity of the beam intensity along its traverse of the test section. The data are also corrected on a scan-by-scan basis for beam attenuation due to the presence of dye in the beam path. The difference in the present experiments is that a calibrating signal usually could not be obtained from the array output itself, since a known concentration is not generally available in the test section (as is the case for the shear layer). A possible solution would be to place a vessel containing a known dye solution in the beam path and image it onto a section of the array. However, this would reduce the spatial resolution of the measurements as the optical system would be operated at a higher image ratio. The solution that was adopted was to image a separate photodiode on such a vessel, and use its output for reference purposes.

The procedure used for the conversion of the fluorescence data to dye concentration data consists of the following steps.

A) Background noise pattern

The background noise pattern was recorded prior to each experiment at

full laser power with no laser dye in the test section. This was always zero since the combination of fixed pattern noise of the array and the background pattern illumination were less than a single level of the ADC.

B) Determination of the overall transfer function

After the optical system was focused, the test section was filled with a uniform (weak) dye solution of known concentration and the time average of the array output over a large number of array scans was recorded. The calibrating solution was also used to fill the small vessel placed on the beam path and the single calibrating photodiode was focused on the beam inside this vessel. The averaged output of the calibrating photodiode was also recorded. The fluorescense measured is related to the input laser power through

$$F(\xi) = I_o H(\xi) \varepsilon c_o e^{-\varepsilon c_o \xi} \qquad (B.1)$$

where:

F is the averaged output of the array corresponding to the raw fluorescence measured in the test section

ξ is a coordinate along the direction of beam propagation spanning the dye containing region along the beam path

c_o is the known dye molar concentration in the test section

H is the unknown transfer function which includes all possible

nonuniformities and unknown constants of the optical system.

For the photodiode output we have the corresponding relation

$$F_s = I_o H_s \varepsilon c_o e^{-\varepsilon c_o \xi_s} \tag{B.2}$$

where ξ_s spans all the dye containing region in the beam path up to the sensor, and subscript s refers to photodiode quantities.

C) Data reduction

During the experiment, where the fluorescence intensity from an unknown concentration pattern is recorded for each scan, we may write for the instantaneous array output,

$$F(\xi,t) = I_1 H(\xi) \varepsilon c(\xi,t) e^{-\varepsilon \int_o^{\xi} c(\zeta,t) d\zeta} \tag{B.3}$$

and for the calibrating photodiode output,

$$F_s(t) = I_1 H_s \varepsilon c_o e^{-\int_o^{\xi_s} c(\zeta,t) d\zeta} . \tag{B.4}$$

We have allowed for the possibility that the input laser power I_1 during the experiment differs from the calibration conditions.

There are two possible methods to determine $c(\xi,t)$ from the calibration experiment.

i) Compute from (B.1) the function $G(\xi) = \varepsilon H(\xi)$ and apply the correction for attenuation, on a scan-by-scan basis, using the following "recursive" relation following from (B.3)

$$c(\xi,t) = \frac{F(\xi,t)}{I_1 G(\xi)} e^{\varepsilon \int_0^{\xi} c(\zeta,t)d\zeta} .$$

The validity for this approach relies on the assumption that the laser beam intensity I_1 remains constant during the experiment. This assumption could be justified in the present experiments since the stabilizer circuit in the laser head kept the laser intensity constant to within 1%.

ii) An alternative method, especially useful when the input laser intensity might be fluctuating in time during the experiment, is by use of the instantaneous output of the calibrating photodiode. Note that, from (B.1) and (B.2),

$$G_s(\xi) = \frac{H(\xi)}{c_s H_s}$$

may be obtained, so that the correction for the attenuation may be applied on the following equation, obtained from (B.3) and (B.4)

$$c(\xi,t) = \frac{F(\xi,t)}{F_s(t) G_s(\xi)} e^{\varepsilon \int_{\xi_s}^{\xi} c(\zeta,t)d\zeta} .$$

It should be noted that the reference concentration may be placed either at the beginning or the end of the test section. In each case, the computation for each scan should start from the pixel that is imaged to the location closest to the reference location and proceed outwards. In the case where the reference condition is imaged on the array itself (for example, on the known constant concentration at the jet exit plane in the case of axial measurements), method (ii) is appropriate with quantities subscripted with s corresponding to the array pixel imaged on the reference concentration.

REFERENCES

Antonia, R.A., A. Prabhu, and S.E. Stephenson (1975) Conditionally sampled measurement in a heated turbulent jet. J. Fluid Mech. 72, 455-480.

Batchelor, G.K. (1952) The effect of homogeneous turbulence on material lines and surfaces. Proc. Roy. Soc. A 213, 349.

Batchelor, G.K. (1959) Small scale variation of connected quantitites of like temperature in turbulent fluid. Part 2 The case of large conductivity. J. Fluid Mech. 5, 134-139.

Becker, H.A., H.C. Hottel, and G.C. Williams (1967) The nozzle-fluid concentration field of the round, turbulent, free jet. J. Fluid Mech. 30, 285-303.

Becker, R.S. (1969) Theory and Interpretation of Fluorescence and Phosphorescence. Wiley-Interscience, New York.

Bendat, J.S. and A.G. Piersol (1971) Random Data: Analysis and Measurement Procedures. Wiley-Interscience, New York.

Bernal, L.P. (1981) The coherent structure of turbulent mixing layers: I. Similarity of the primary vortex structure. II. Secondary streamwise vortex structure. Ph.D. Thesis, California Institute of Technology, Pasadena, California.

Birch, A.D., D.K. Brown, M.G. Dodson, and J.R. Thomas (1978) The turbulent concentration field of a methane jet. J. Fluid Mech. 88, 431-449.

Breidenthal, R.E. (1978) A chemically reacting turbulent mixing layer. Ph.D. Thesis, California Institute of Technology, Pasadena, California.

Breidenthal, R.E. (1981) Structure in turbulent mixing layers and wakes using a chemical reaction. J. Fluid Mech. 109, 1-24.

Broadwell, J.E., and R.E. Breidenthal (1982) A simple model of mixing and chemical reaction in a turbulent shear layer. J. Fluid Mech. 125, 397.

Brown, G.L., and A. Roshko (1974) On density effects and large structure in turbulent mixing layers. J. Fluid Mech. 64(4), 775-816.

Chen, C.J., and W. Rodi (1980) Vertical Turbulent Buoyant Jets: A Review of Experimental Data. Pergamon Press, Oxford.

Chevray, R., and N.K. Tutu (1978) Intermittency and preferential transport of heat in a round jet. J. Fluid Mech. 88, 133.

Corrsin, S. (1943) Investigation of flow in an axially symmetric heated jet of air. NACA Wartime Report W-94.

Corrsin, S., and A.L. Kistler (1955) NACA Report R-1244.

Corrsin, S., and M.S. Uberoi (1950) Further experiments on the flow and heat transfer in a heated turbulent air jet. NACA Report 998.

Dahm, W.J.A. (1985) Experiments on entrainment, mixing and chemical reactions in turbulent jets at large Schmidt number. Ph.D. Thesis, California Institute of Technology, Pasadena, California.

Dewey, C.F., Jr. (1976) Qualitative and quantitative flow field visualization utilizing laser induced fluorescence. In Proc. AGARD Conf. on Applications of Non-Intrusive Instrumentation in Fluid Flow Research, AGARD-CP-193.

Dimotakis, P.E., and D.A. Papantoniou (1981) Investigation of the relation of the structure of turbulence in the near field of a turbulent jet to the noise emitted in the far field. Final Scientific Report, Contract No. Y-481468-0935N, Boeing Commerical Airplane Company.

Dimotakis, P.E., R.C. Miake-Lye and D.A. Papantoniou (1983) Structure and dynamics of round turbulent jets. Phys. Fluids 6, 3185.

Fischer, H.B., E.J. List, R.C.Y. Koh, J. Imberger, and N.H. Brooks (1979) Mixing in Inland and Coastal Waters. Academic Press, New York.

Gartell, G. (1978) A signal processor for a laser-Doppler velocimeter. Tech. Memo. 78-5, W.M. Keck Laboratory of Hydraulics and Water Resources, California Institute of Technology, Pasadena, California.

Hannoun, I. (1985) Matching the refractive index in density stratified flows. Tech. Memo. 85-1, W.M. Keck Laboratory of Hydraulics and Water Resources, California Institute of Technology, Pasadena, California.

Hinze, J. (1975) Turbulence. McGraw-Hill, New York.

Jimenez, J., M. Cogollos, and L. Bernal (1985) A perspective view of the plane mixing layer. J. Fluid Mech. 152, 125-143.

Kolmogorov, A.N. (1941) C.R. Acad. Sci. URSS, 30, 301.

Komori, S., and H. Ueda (1985) The large-scale coherent structure in the intermittent region of the self-preserving round free jet. J. Fluid Mech. 152, 337-360.

Konrad, J.H. (1976) An experimental investigation of mixing in two-dimensional turbulent shear flows with application to diffusion-limited chemical reactions. Ph.D. Thesis, California Institute of Technology, Pasadena, California. Also Project SQUID Technical Report CIT-8-PU.

Koochesfahani, M.M. (1984) Experiments on turbulent mixing and chemical reactions in a liquid mixing layer. Ph.D. Thesis, California Institute of Technology, Pasadena, California.

Kotsovinos, N.E. (1975) A study of the entrainment and turbulence in a plane buoyant jet. Ph.D. Thesis. California Institute of Technology, Pasadena, California. 306 pp.

Kotsovinos, N.E., and E.J. List (1977) Plane turbulent buoyant jets: Part 1 - Integral properties. J. Fluid Mech. 81, 25-44.

Kotsovinos, N.E. (1977) Plane turbulent buoyant jets: Part 2 - Turbulent structure. J. Fluid Mech. 81, 45-62.

Kychakoff, G., R.D. Howe, R.K. Hanson, and K. Knapp (1983) Flow visualization in combustion gases. AIAA Paper No. 83-0405, 21st Aerospace Sciences Meeting, January 1983.

Landau, L.D., and E.M. Lifshitz (1959) Fluid Mechanics. Pergamon Press, New York.

List, E.J. (1982) Mechanics of turbulent buoyant jets and plumes. In Turbulent Buoyant Jets and Plumes, W. Rodi, Ed., Pergamon Press, New York.

List, E.J., and J. Imberger (1973) Turbulent entrainment in buoyant jets. Proc. ASCE, J. Hyd. Div. 99, 1461-1474.

List, E.J., and J. Imberger (1975) Closure of discussion to: Turbulent entrainment in buoyant jets and plumes. Proc. ASCE, J.Hyd. Div. 101, 617-620.

Liu, H.T., J.T. Lin, D.P. Delisi, and F.A. Robben (1977) Application of a fluorescence technique to dye-concentration measurements in a turbulent jet. NBS Special Publication 484, in Proc. Symp. on Flow in Open Channels and Closed Conduits.

Middleton, J.H. (1975) The asymptotic behaviour of a starting plume. J. Fluid Mech. 72, 753-771.

Monin, A.S., and A.M. Yaglom (1971) Statistical Fluid Mechanics, Volumes I and II. M.I.T. Press, Cambridge, Mass.

Morton, B.R. (1959) Forced plumes. J. Fluid Mech. 5, 151-163.

Mungal, M.G. (1983) Experiments on mixing and combustion with low heat release in a turbulent shear flow. Ph.D. Thesis, California Institute of Technology, Pasadena, California.

Obukhoff, A.M. (1949) Izv. Akad. Nank, SSSR, Geogr. i Geofiz 13, 58.

Papanicolaou, P.N. (1984) Mass and momentum transport in a turbulent buoyant vertical axisymmetric jet. Ph.D. Thesis, California Institute of Technology, Pasadena, California.

Pope, S.B. (1981) A Monte Carlo method for the PDF equations of turbulent reactive flow. Combustion Science and Technology 25, 159-174.

Robben, F.A., J.T. Lin, D.P. Delisi, and H.T. Liu (1976) Feasibility study of a dye-fluorescence technique for measuring concentrations in fluids. Flow Research Note No. 91, Flow Research Inc.

Rouse, H., C.-S. Yih, and H.W. Humphreys (1952) Gravitational convection from a boundary source. Tellus 4, 201-210.

Sreenivasan, K.R., R.A. Antonia, and K. Britz (1979) Local isotropy and large structures in a heated turbulent jet. J. Fluid Mech. 94, 745-775.

Toor, H.L. (1962) Mass transfer in dilute turbulent and nonturbulent systems with rapid irreversible reactions and equal diffusivities. AIChE J. 8(1), 70-78.

Townsend, A.A. (1976) The Structure of Turbulent Shear Flow. Cambridge University Press, Cambridge, England.

Uberoi, M.S., and P.I. Singh (1975) Turbulent mixing in a two-dimensional jet. Phys. Fluids 18, 764.

Walker, B.J. (1979) Turbulence model comparisons for shear layers and axisymmetric jets. U.S. Army Missile Command Technical Report RD-80-1.

Wygnanski, I., and H. Fiedler (1969) Some measurements in the self-preserving jet. J. Fluid Mech. 38 577-612.

Figure 1.1. One of the largest turbulent buoyant jets on record. The Mt. St. Helens eruption May 18, 1980, Washington, U.S.A. (Courtesy of Longview Daily News, Washington.)

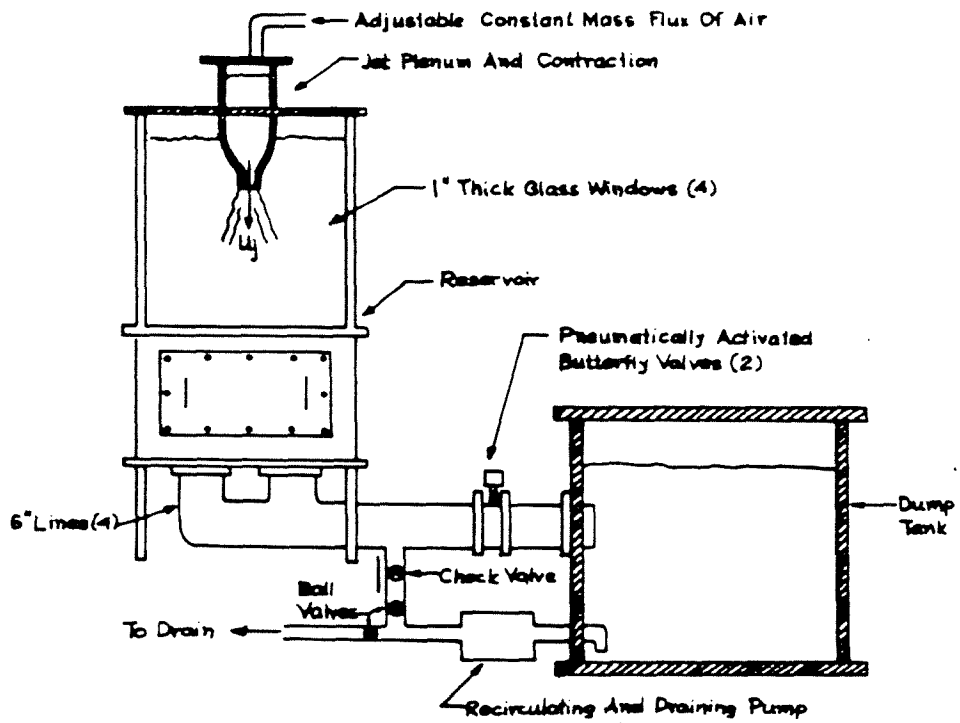

Figure 2.1a. Schematic of the GALCIT water jet facility.

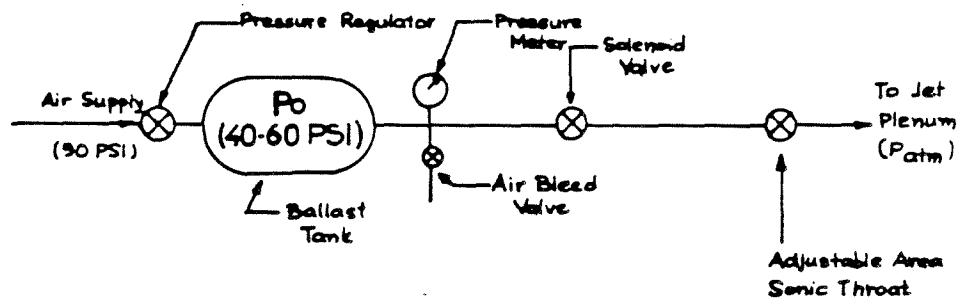

Figure 2.1b. Schematic of jet supply system.

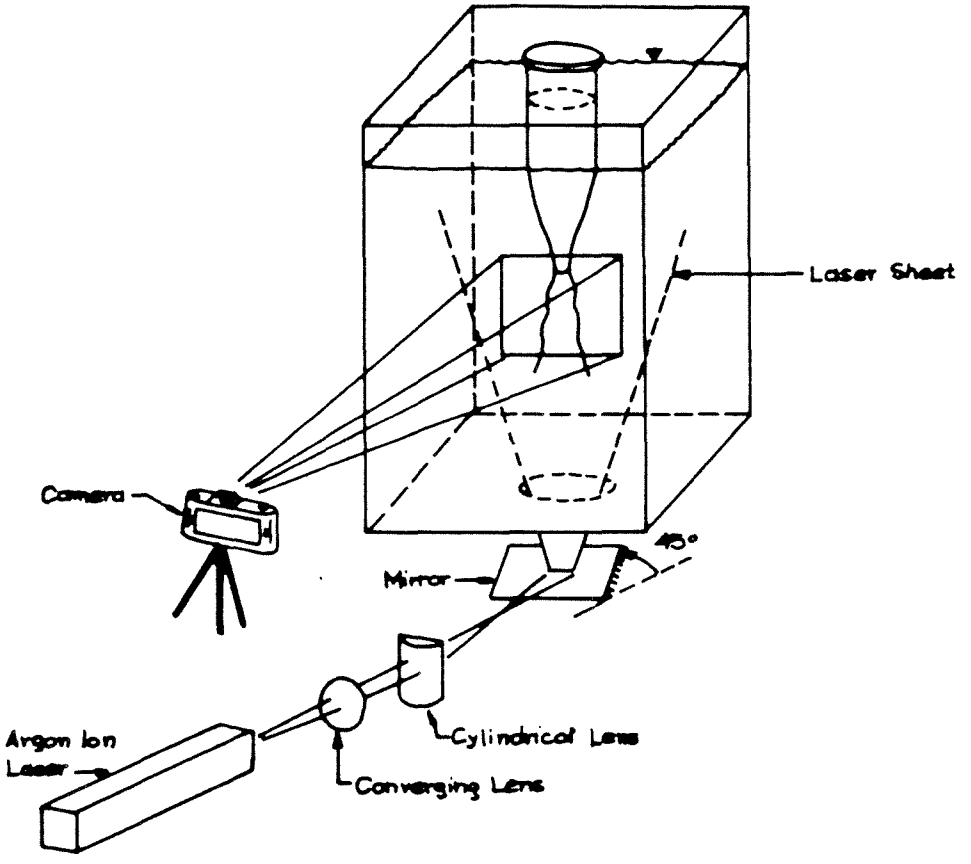

Figure 2.2. Schematic of the optical system for sheet illumination.

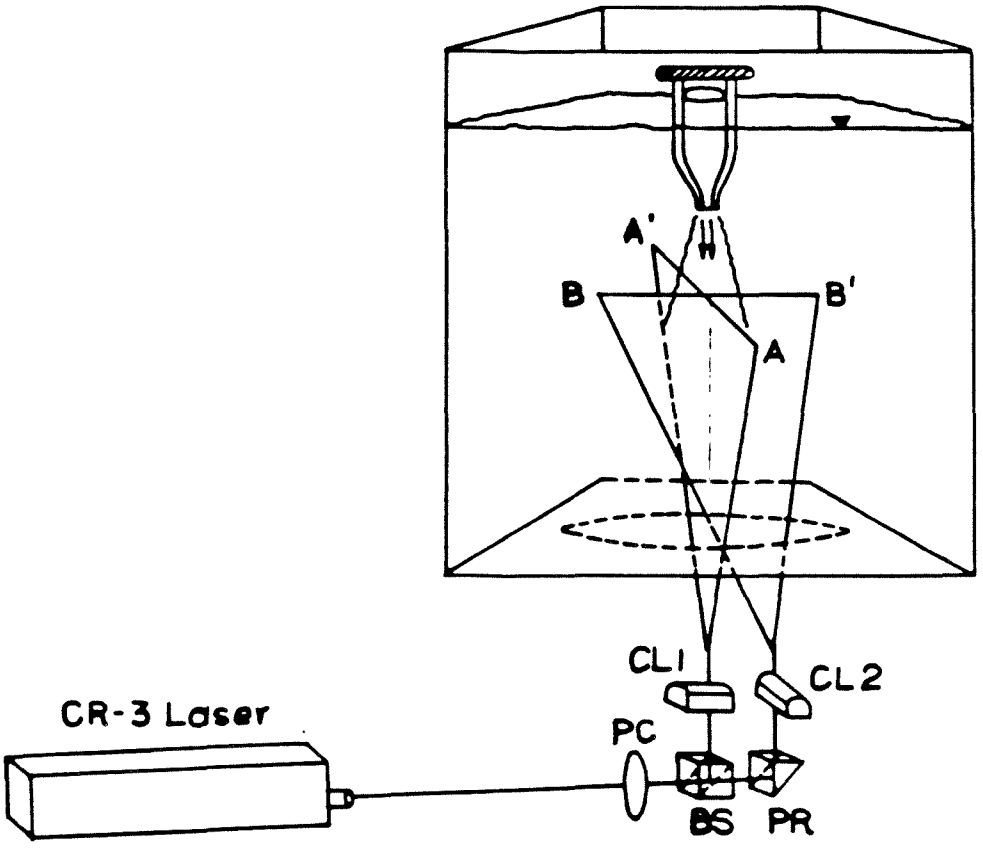

CL: cylindrical lens
PC: plano-convex lens
BS: beam splitter
PR: right angle prism

Figure 2.3. Schematic of the optical system two-sheet illumination.

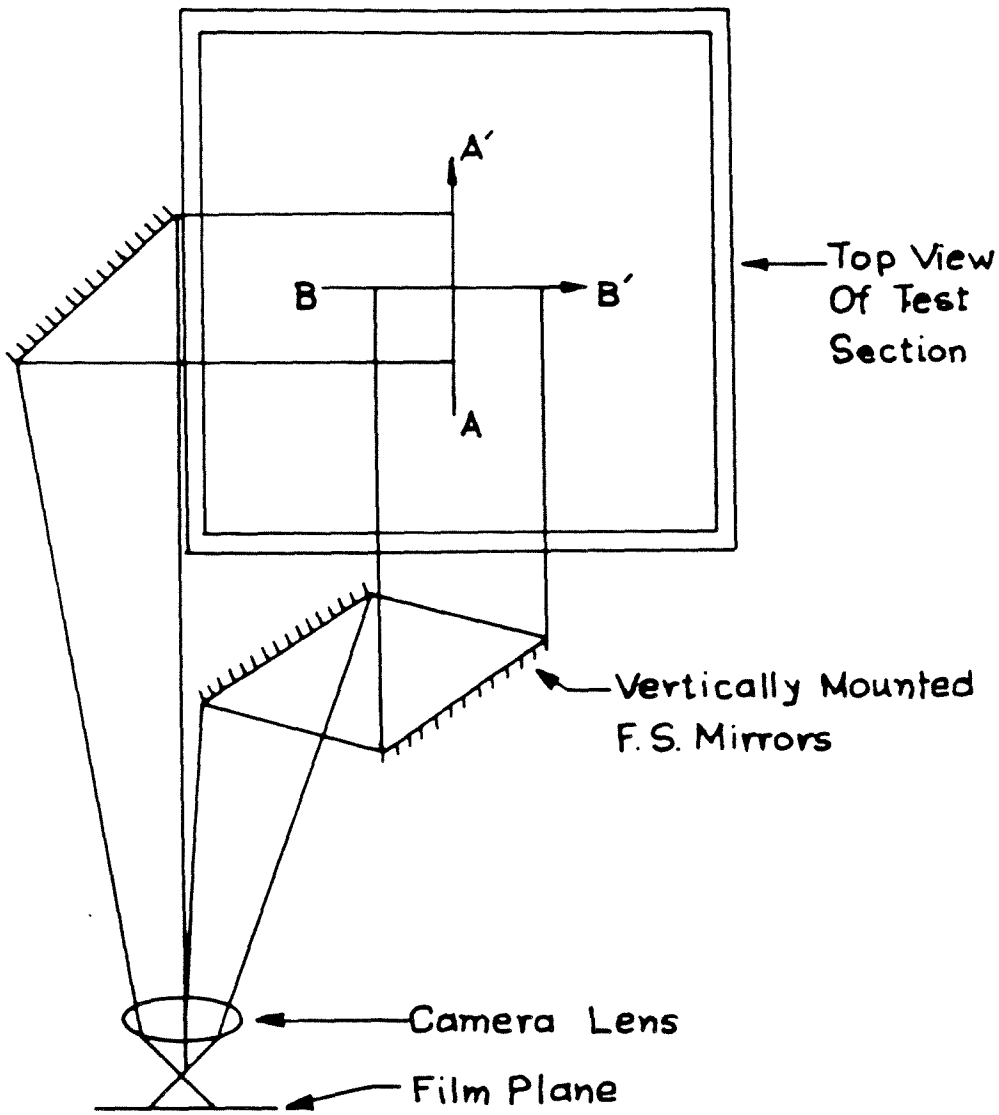

Figure 2.4. Schematic of the system of mirrors for the receiving optics in two-sheet illumination experiments.

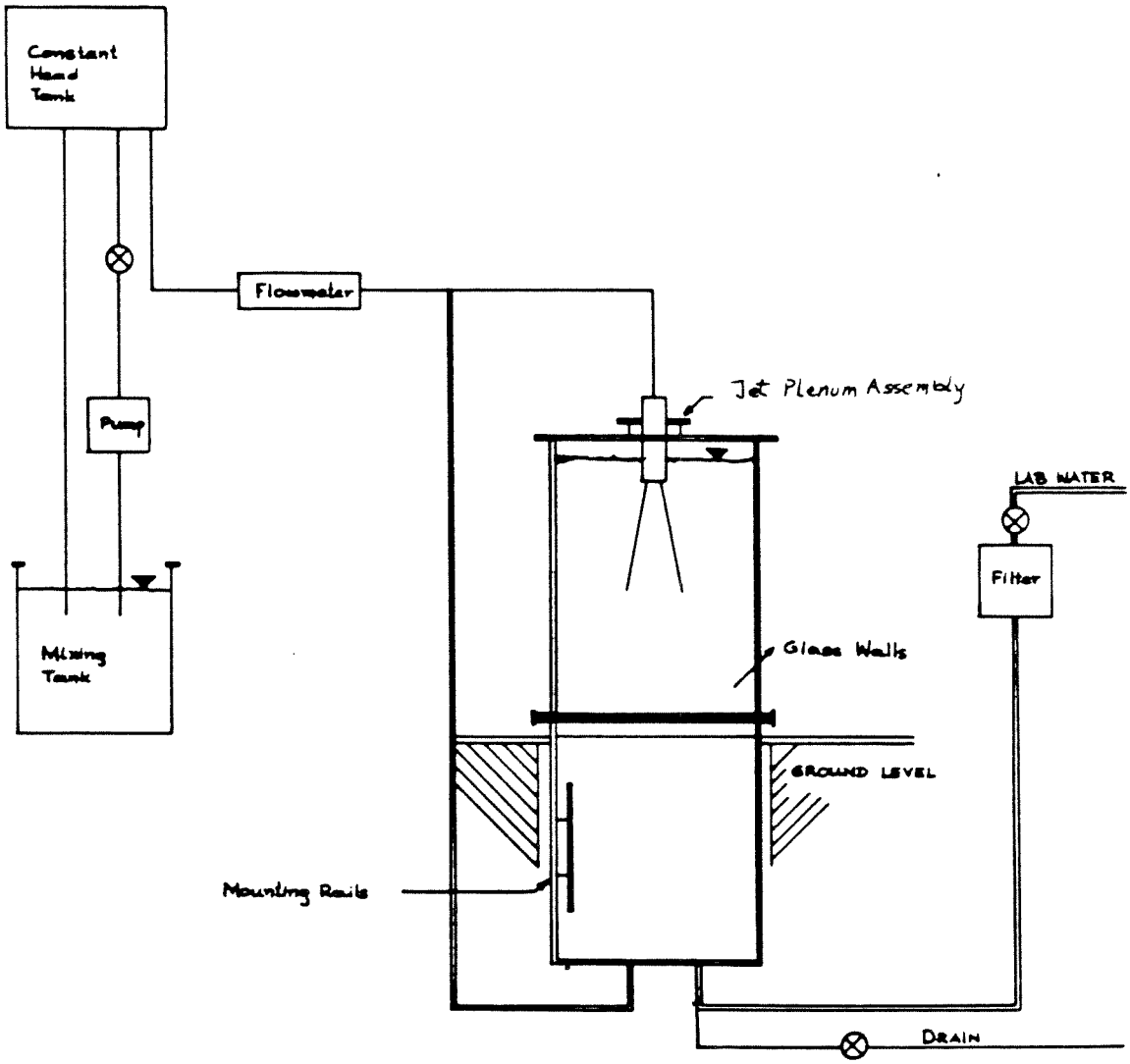

Figure 2.5. Schematic of the Keck Laboratory water jet facility.

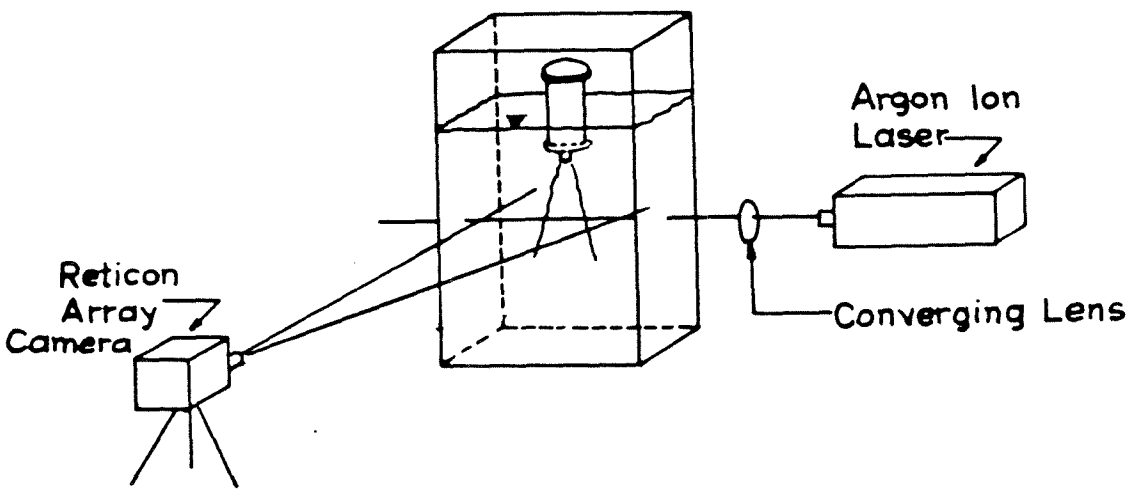

Figure 2.6. Schematic of optical system for radial LIF measurements.

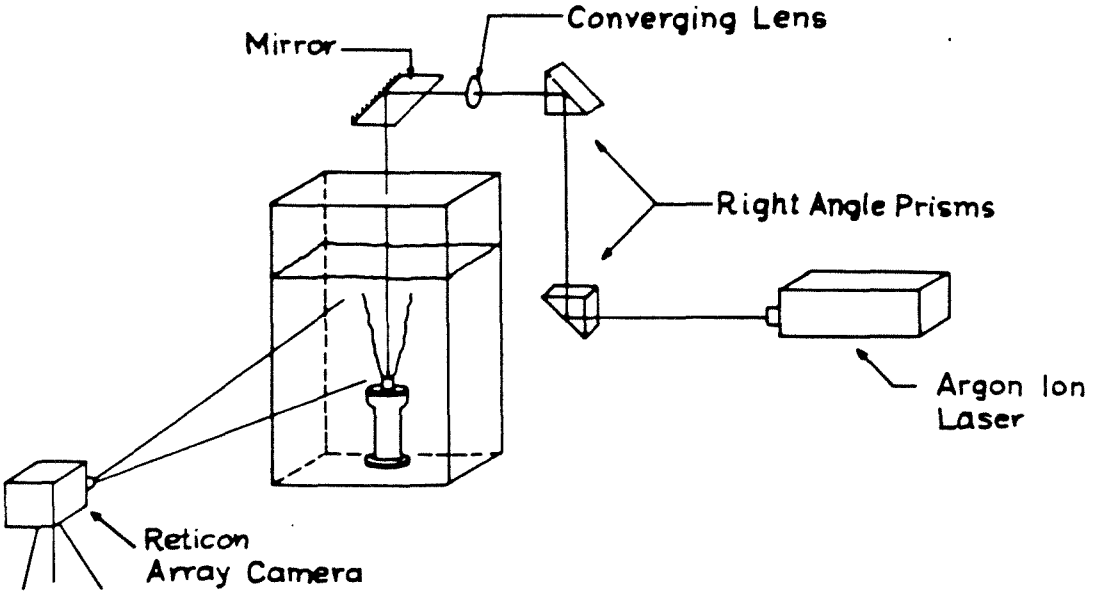

Figure 2.7. Schematic of optical system for axial LIF measurements.

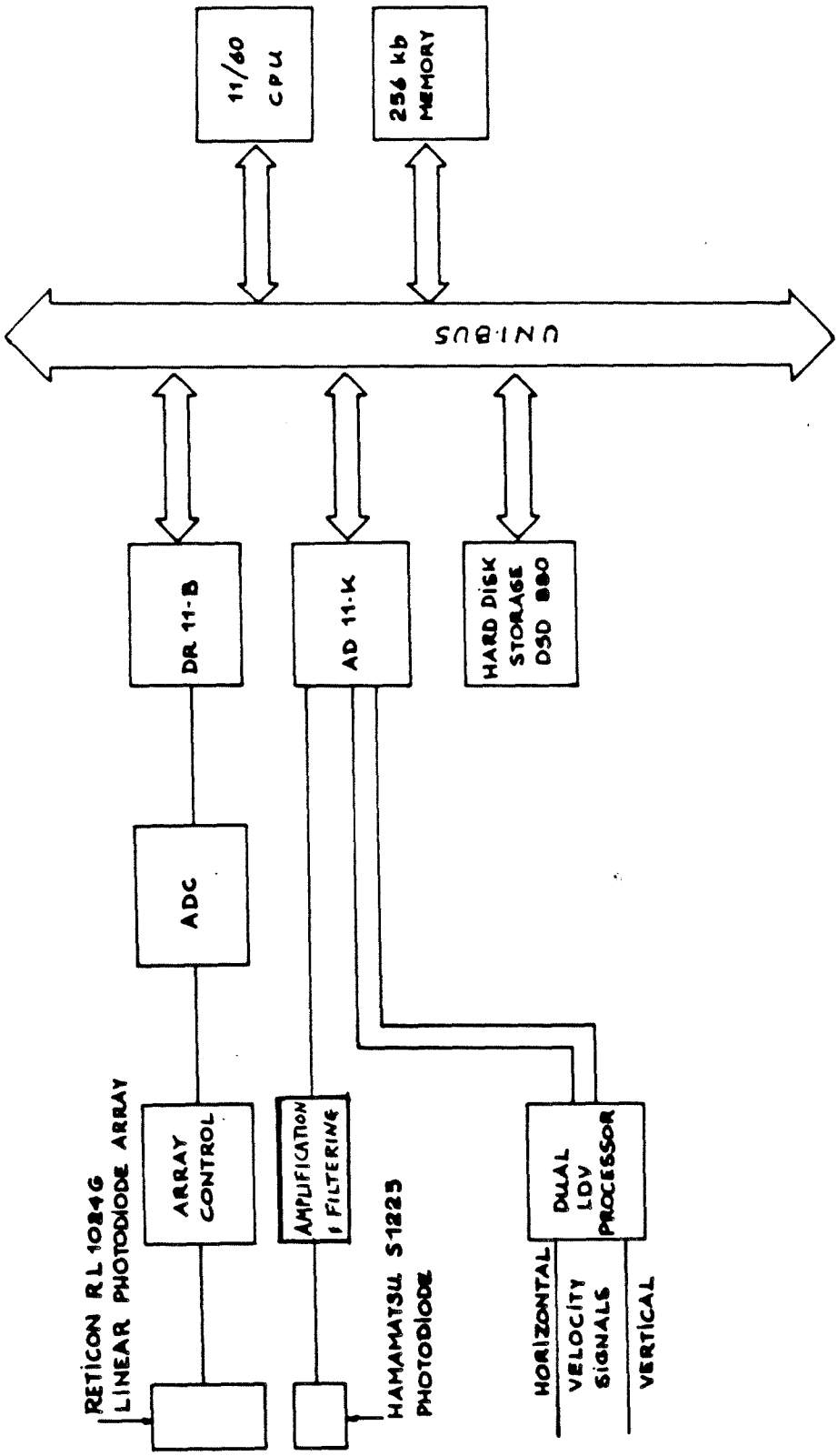

Figure 2.8. Schematic of the data acquisition system.

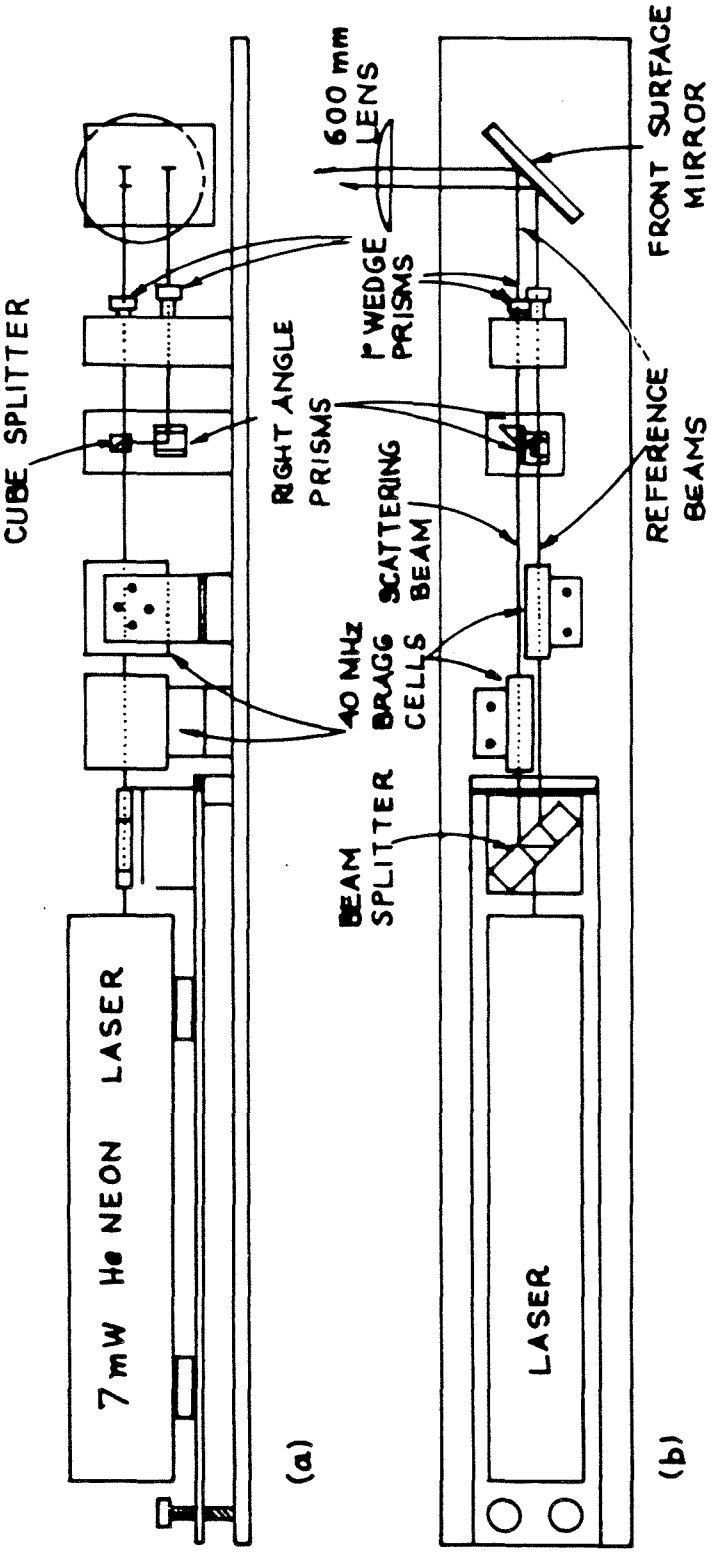

Figure 2.9. Schematic of the LDV optical arrangement.

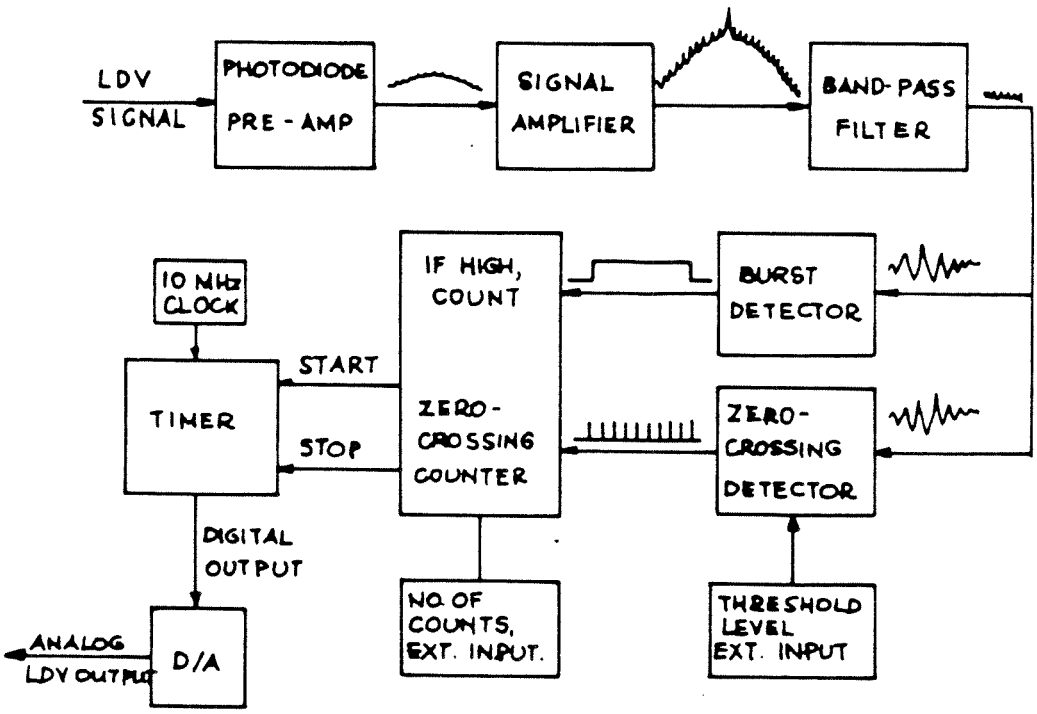

Figure 2.10. Schematic of the LDV processor logic.

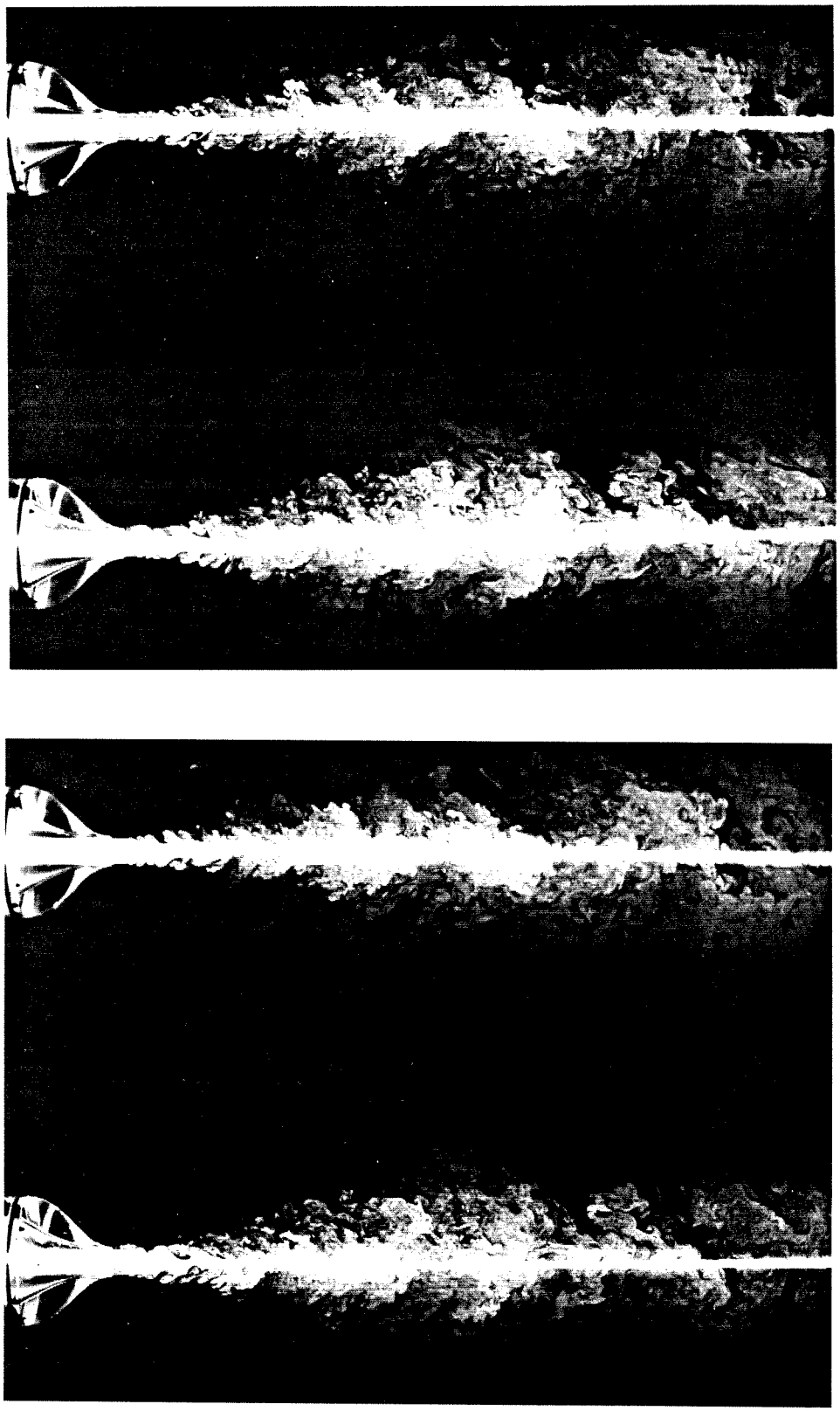

(a) (b)

Figure 3.1. Time sequence photographs of jet mixing at Re = 8500, visualized with two-sheet laser illumination.

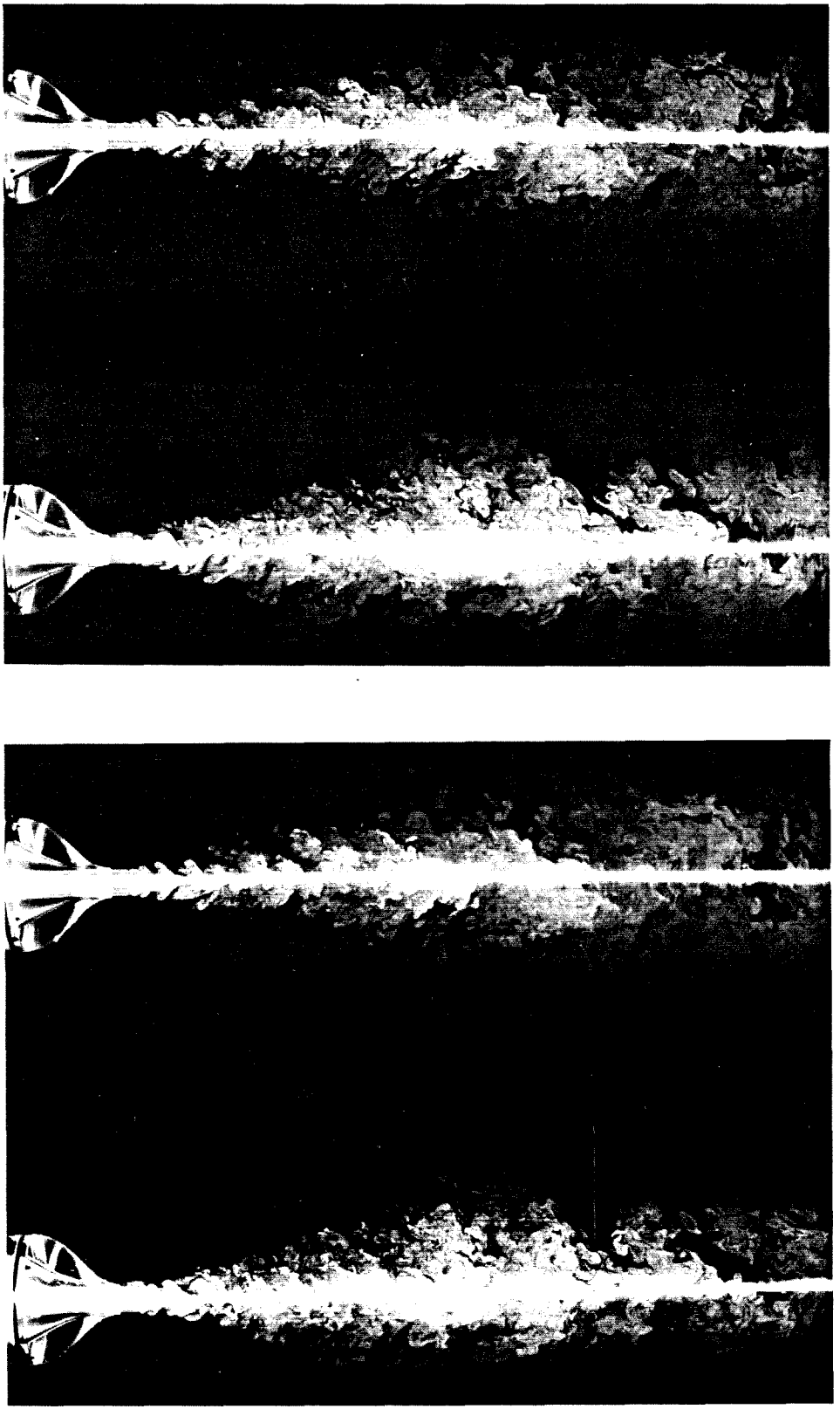

(c)

(d)

Figure 3.1. Time sequence photographs of jet mixing at Re = 8500, visualized with two-sheet laser illumination (continued).

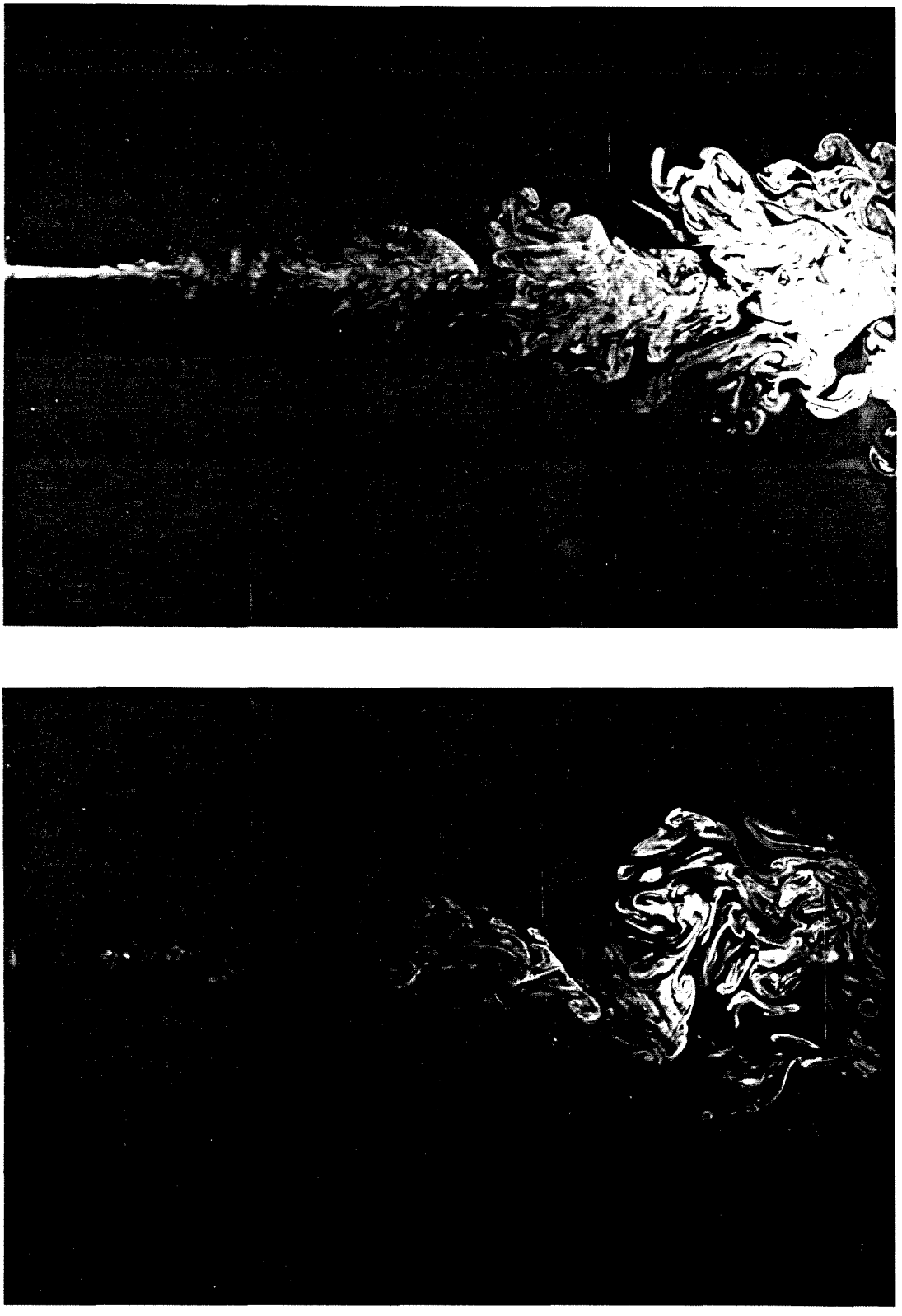

Figure 3.2. Laser sheet illumination photographs of plume mixing.
(a) Buoyancy driven plume (left). (b) Forced plume (right).

Figure 3.2. (continued)
(c) Detailed view of the far field plume mixing region.

Figure 3.3. Laser sheet illumination photograph of low Reynolds number jet, Re = 700, 0< x/d < 160.

(b)

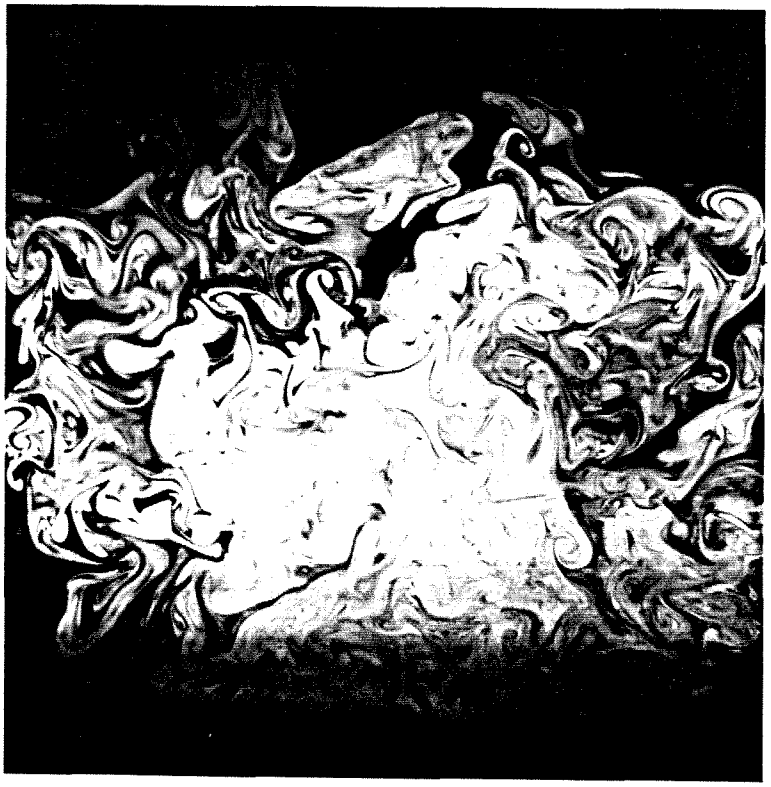

(a)

Figure 3.4a. Transverse laser sheet illumination photograph of jet mixing, Re = 5600, x/d = 66.

Figure 3.4b. Transverse laser sheet illumination photograph of plume mixing, x/Lm = 18, x/d = 66.

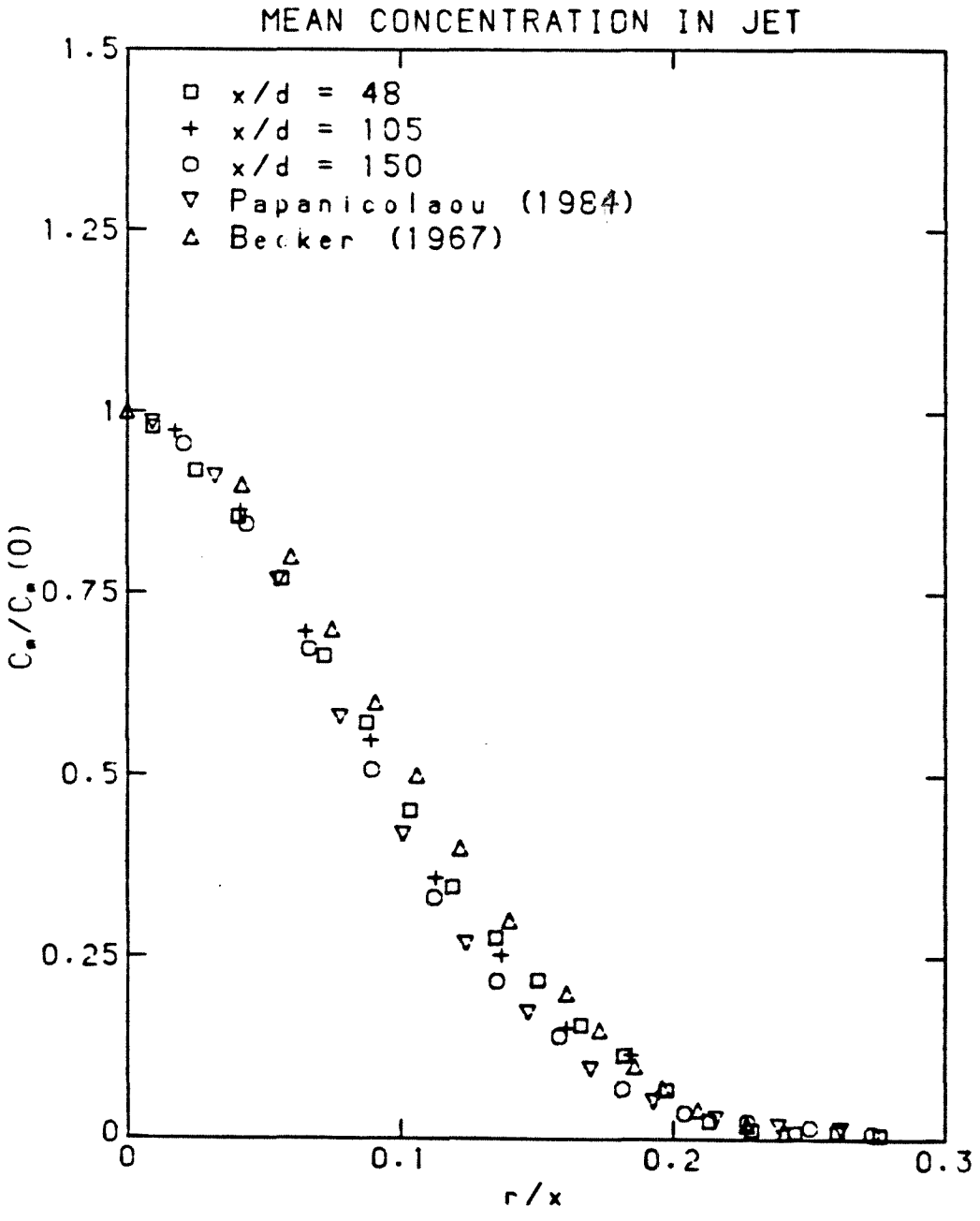

Figure 4.1. Radial profile of mean normalized concentration in jet.

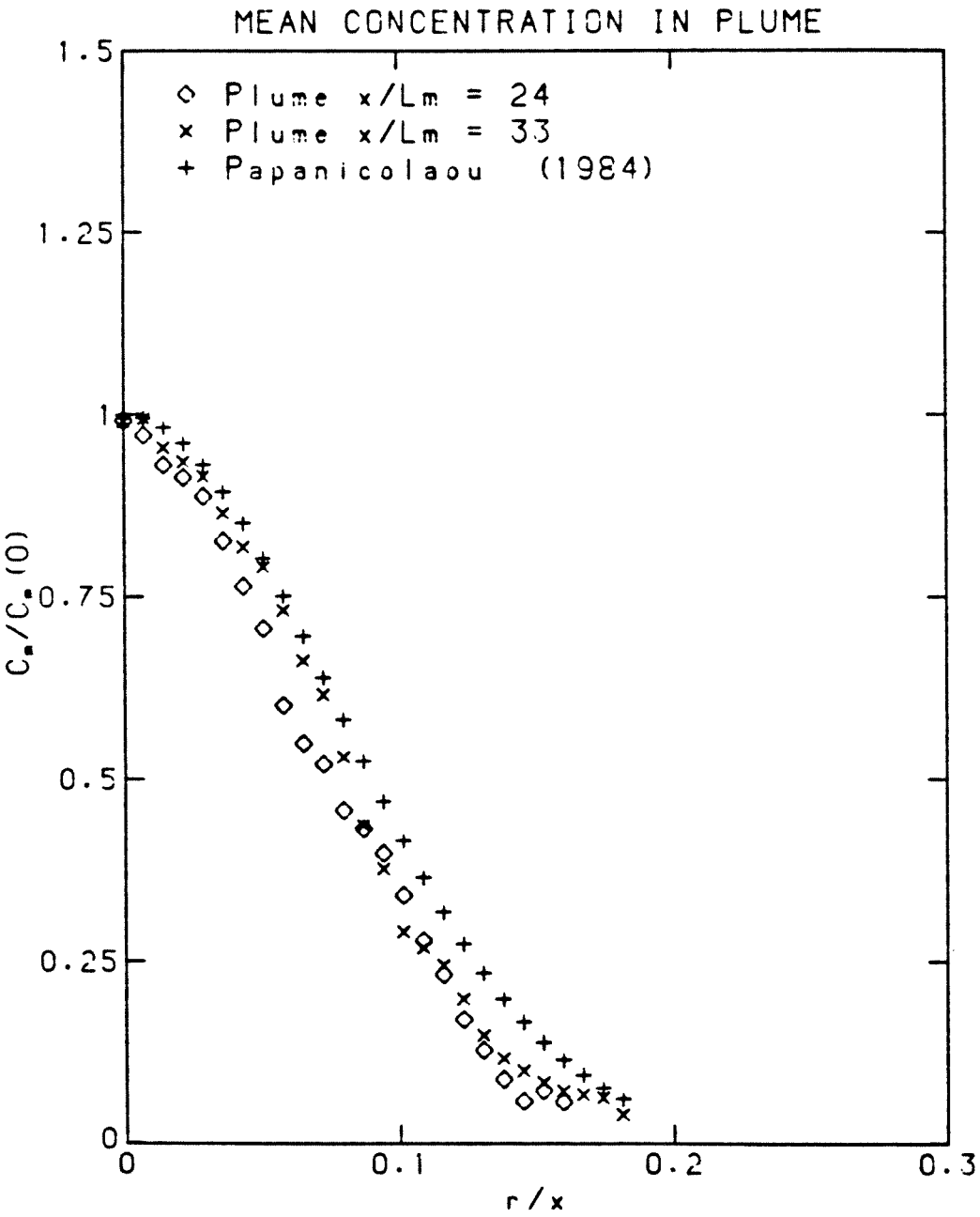

Figure 4.2. Radial profile of mean normalized concentration in plume.

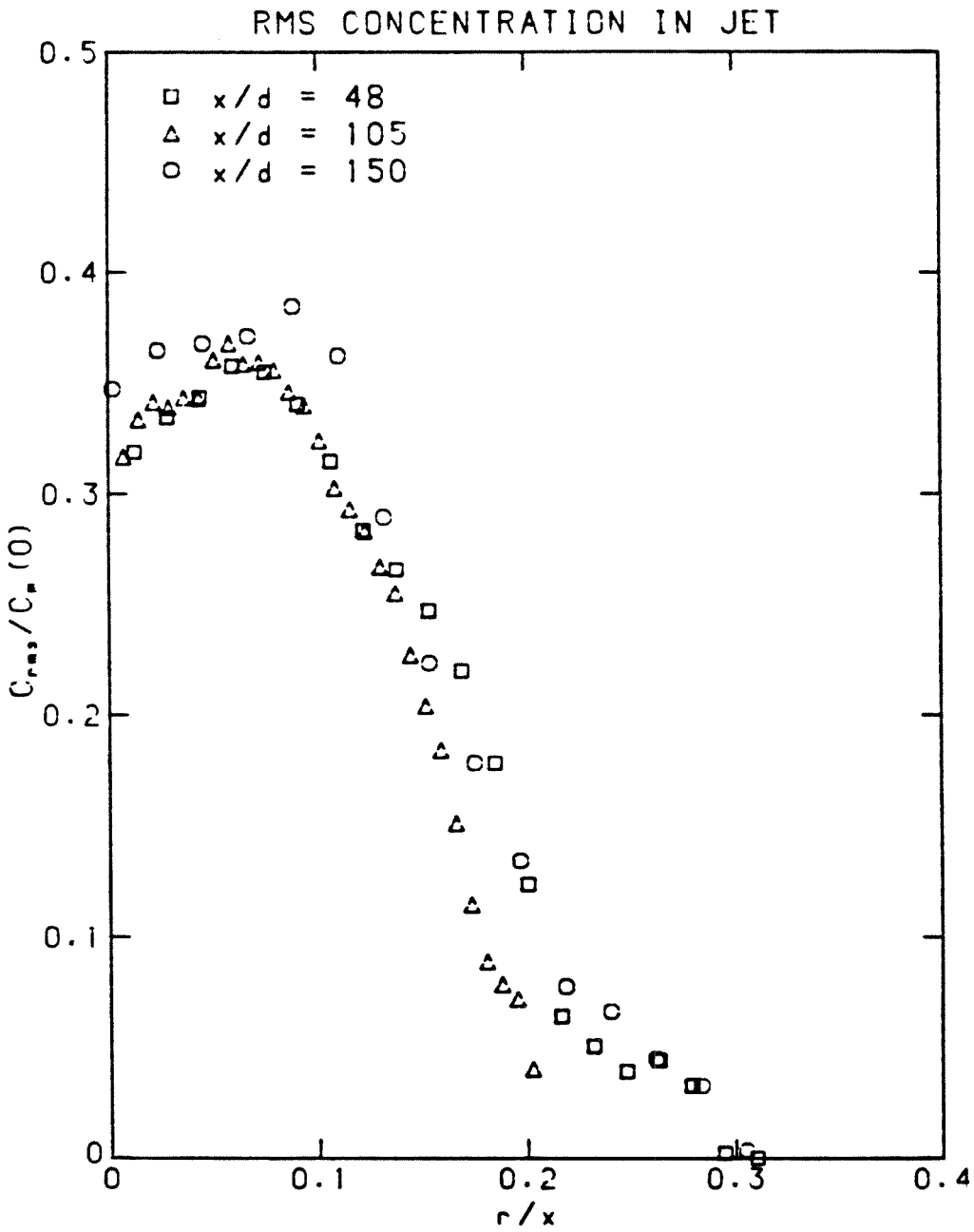

Figure 4.3a. Radial profile of concentration fluctuations in jet.

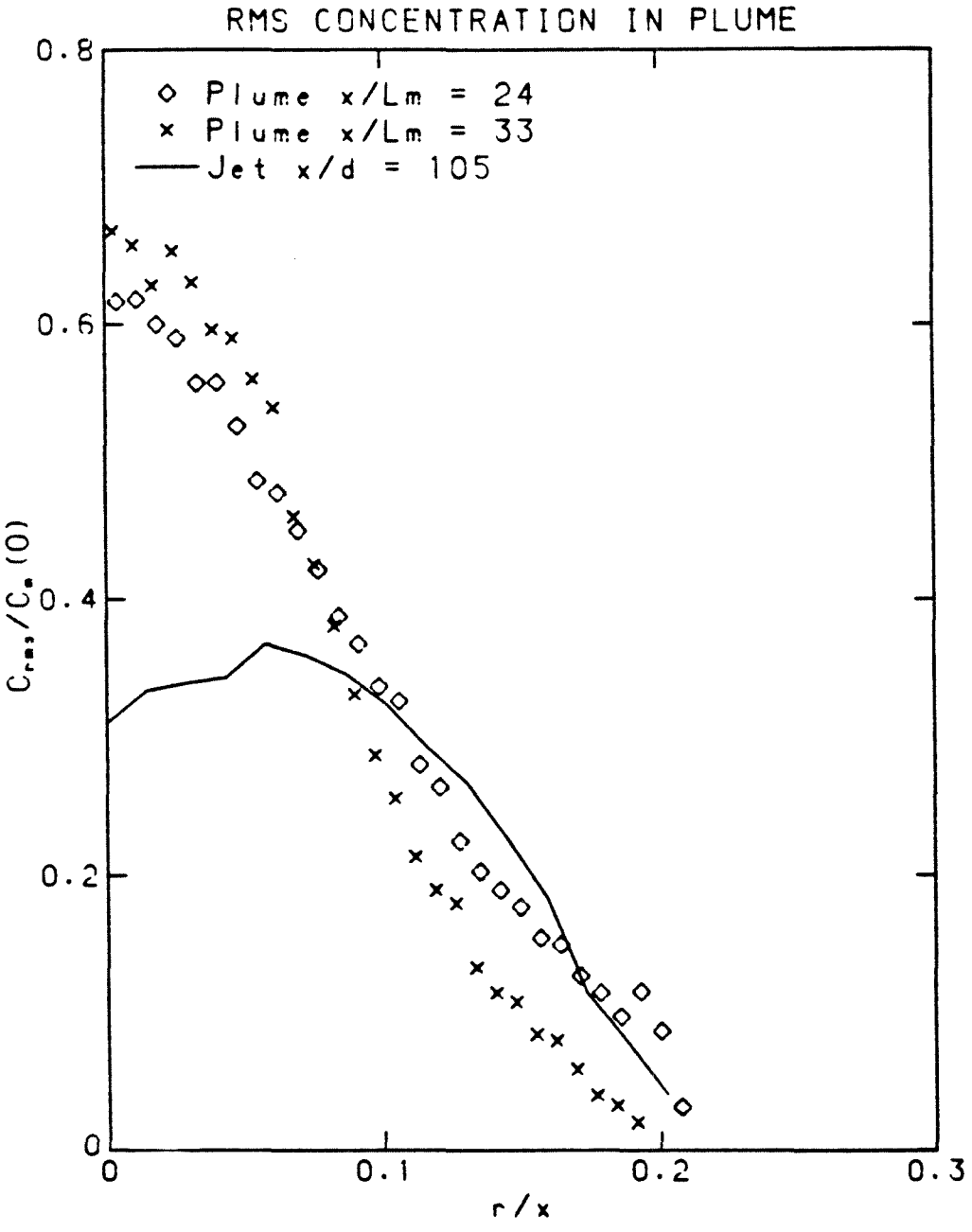

Figure 4.3b. Radial profile of concentration fluctuations in plume.

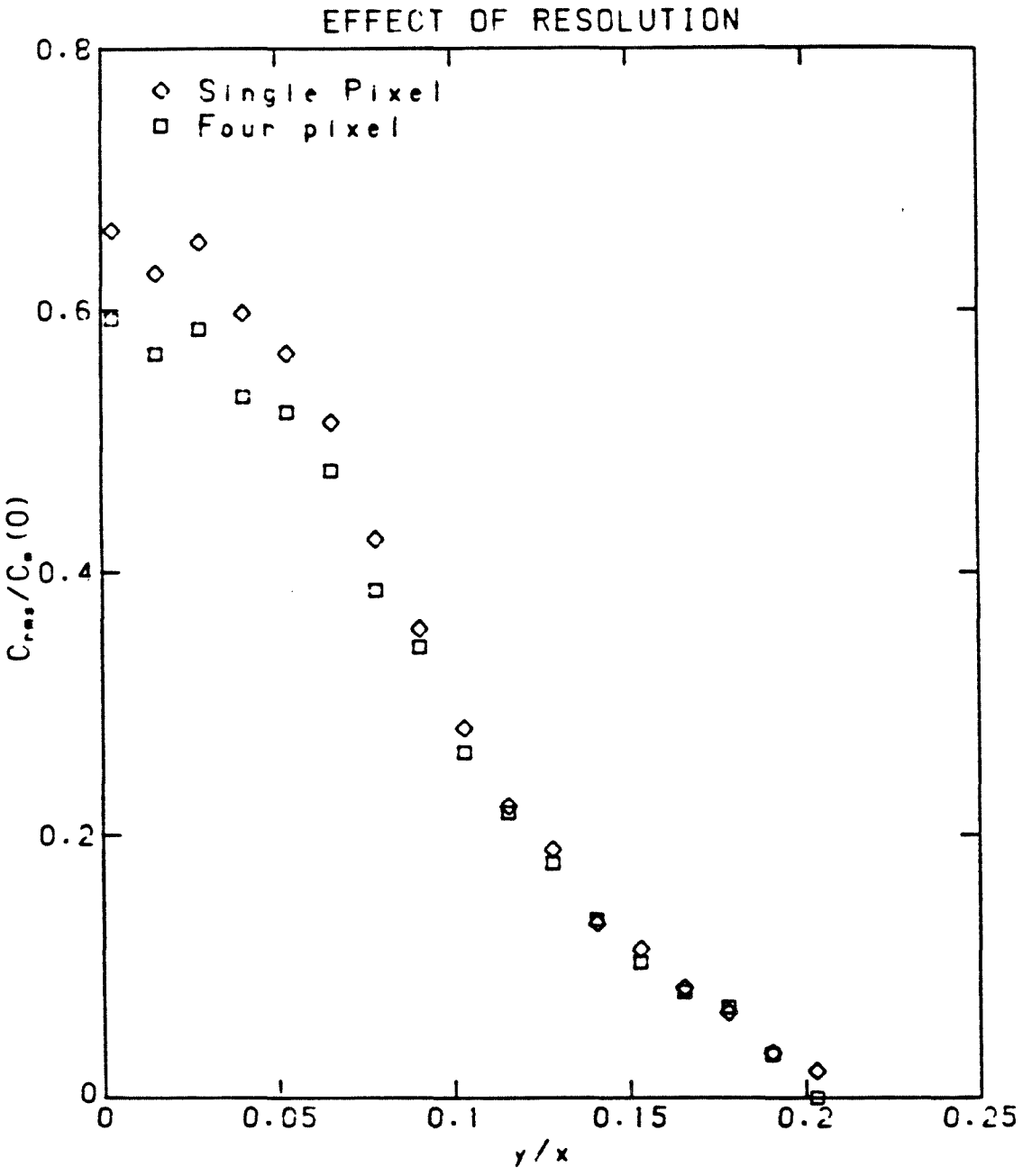

Figure 4.4. Effect of spatial resolution in computation of rms fluctuations in plume.

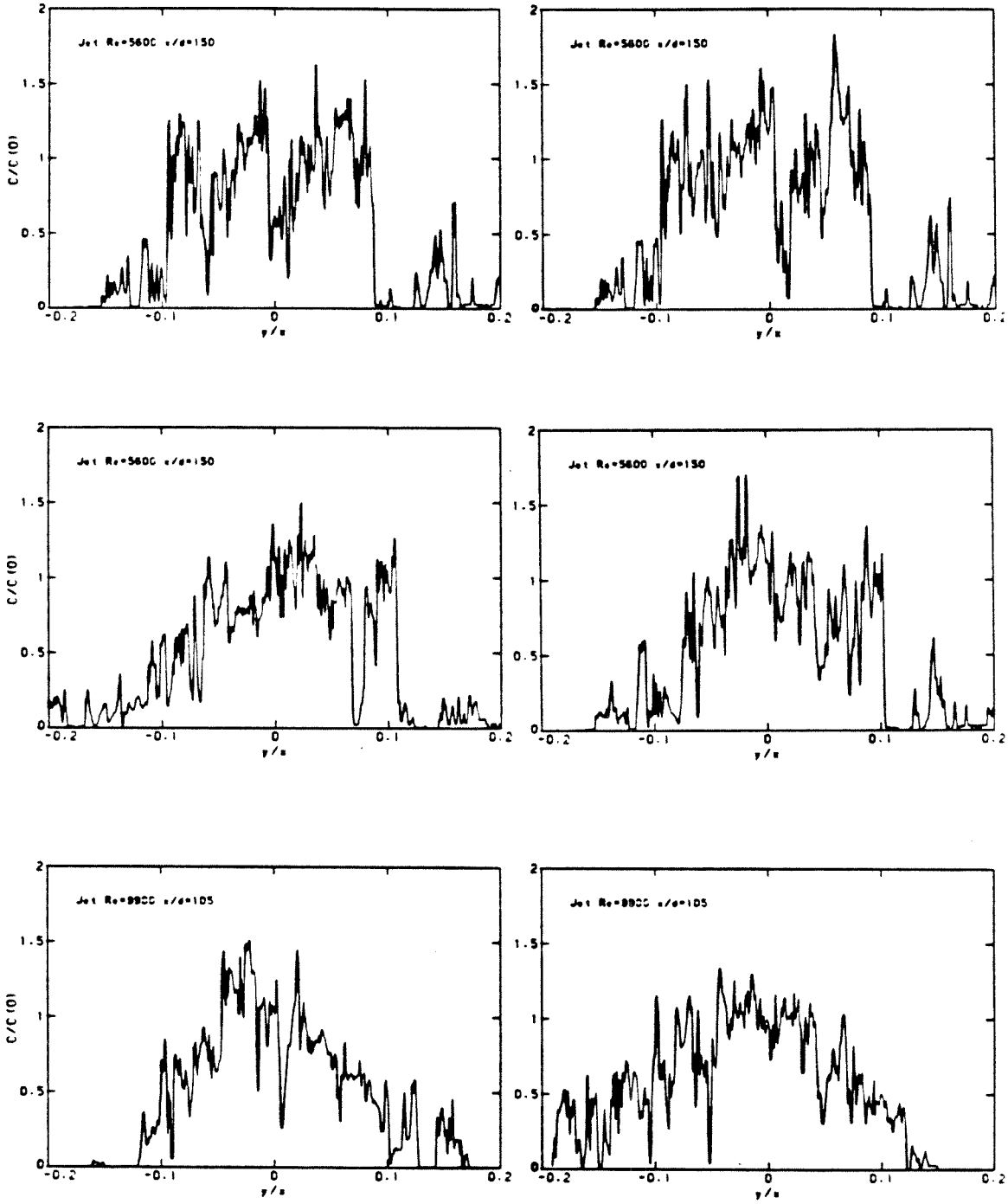

Figure 4.5. Instantaneous concentration profiles in jet.

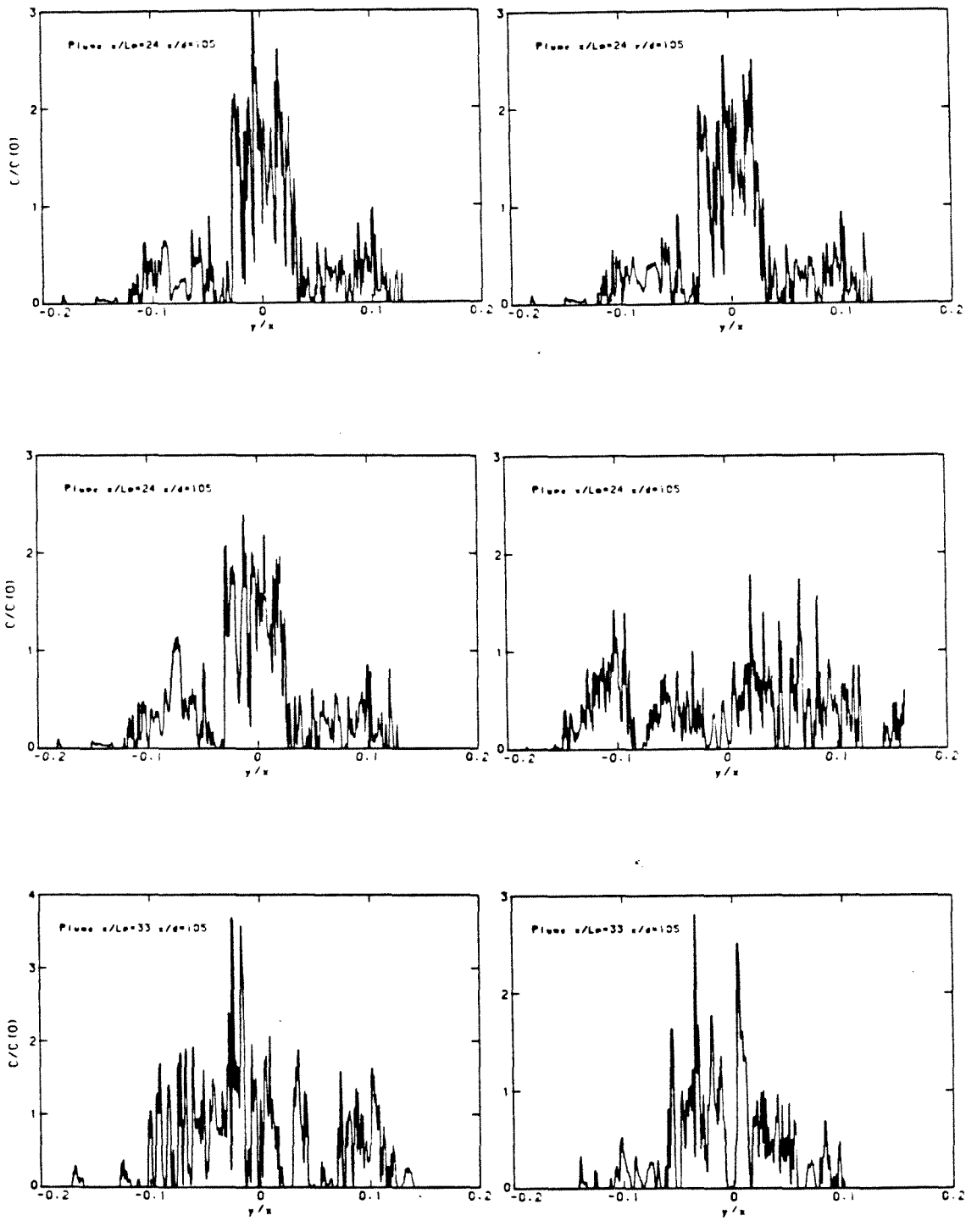

Figure 4.6. Instantaneous concentration profiles in plume.

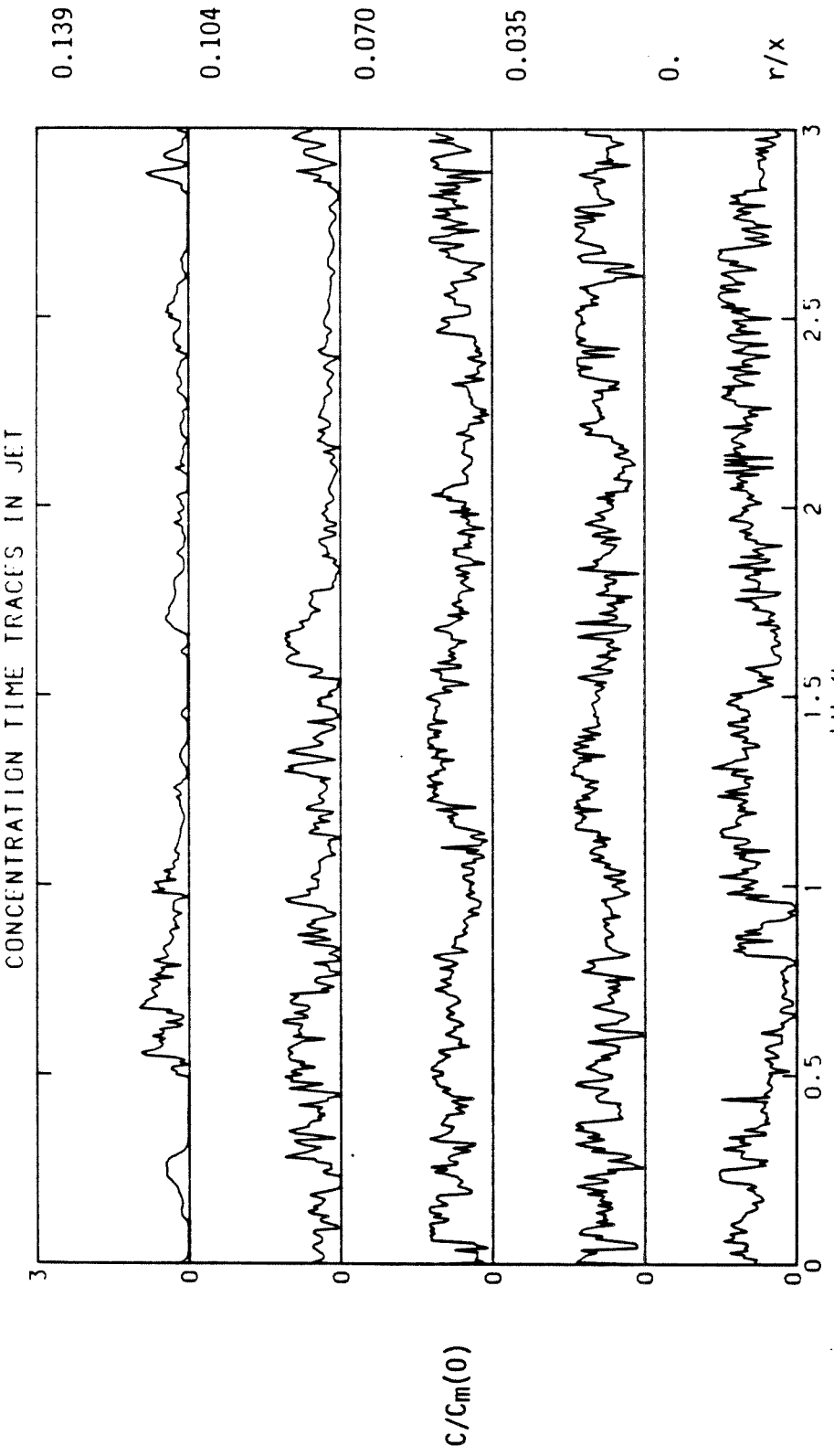

Figure 4.7. Concentration time traces at various radial positions in jet.

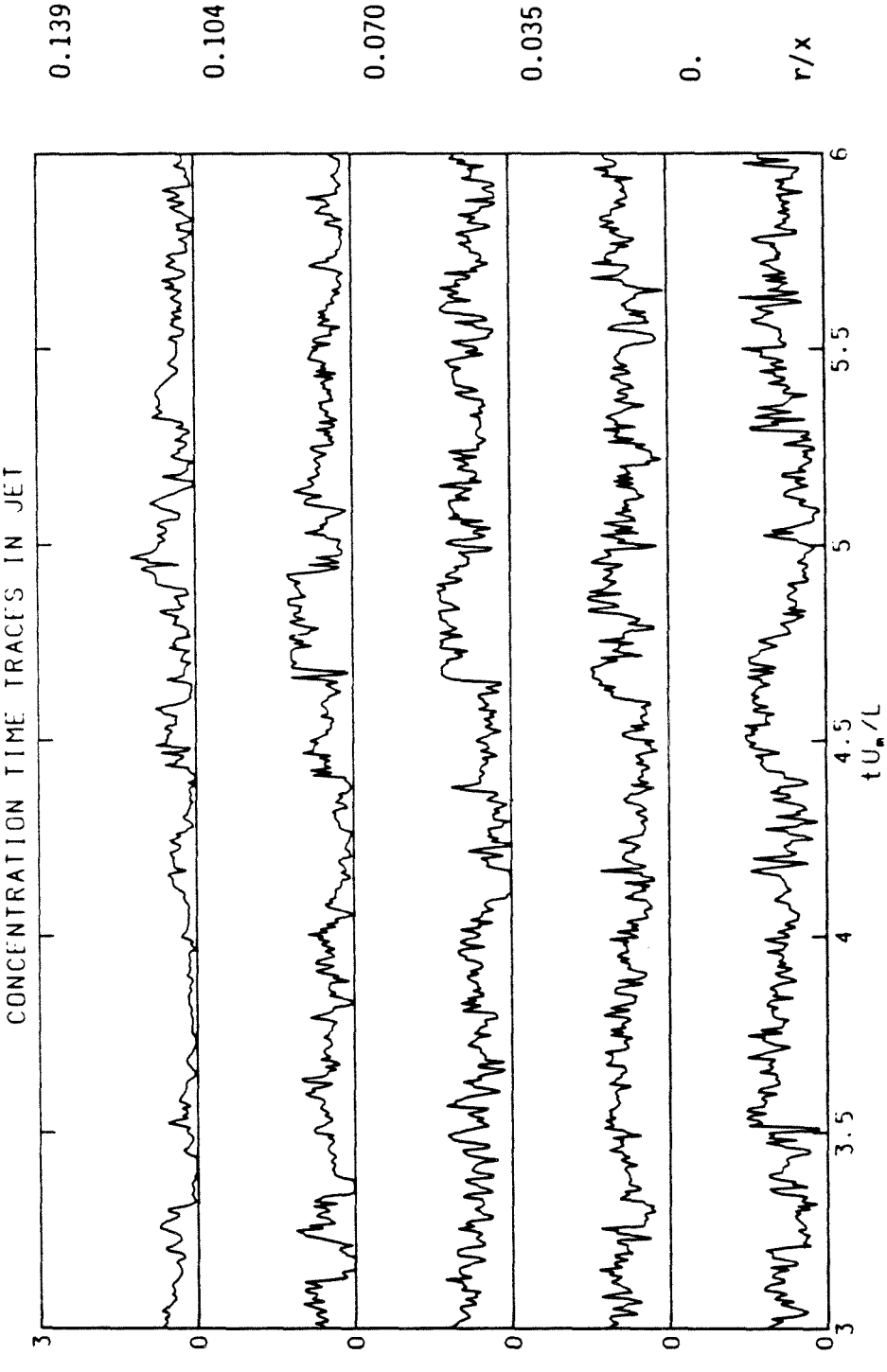

Figure 4.7. Concentration time traces at various radial positions in jet (continued).

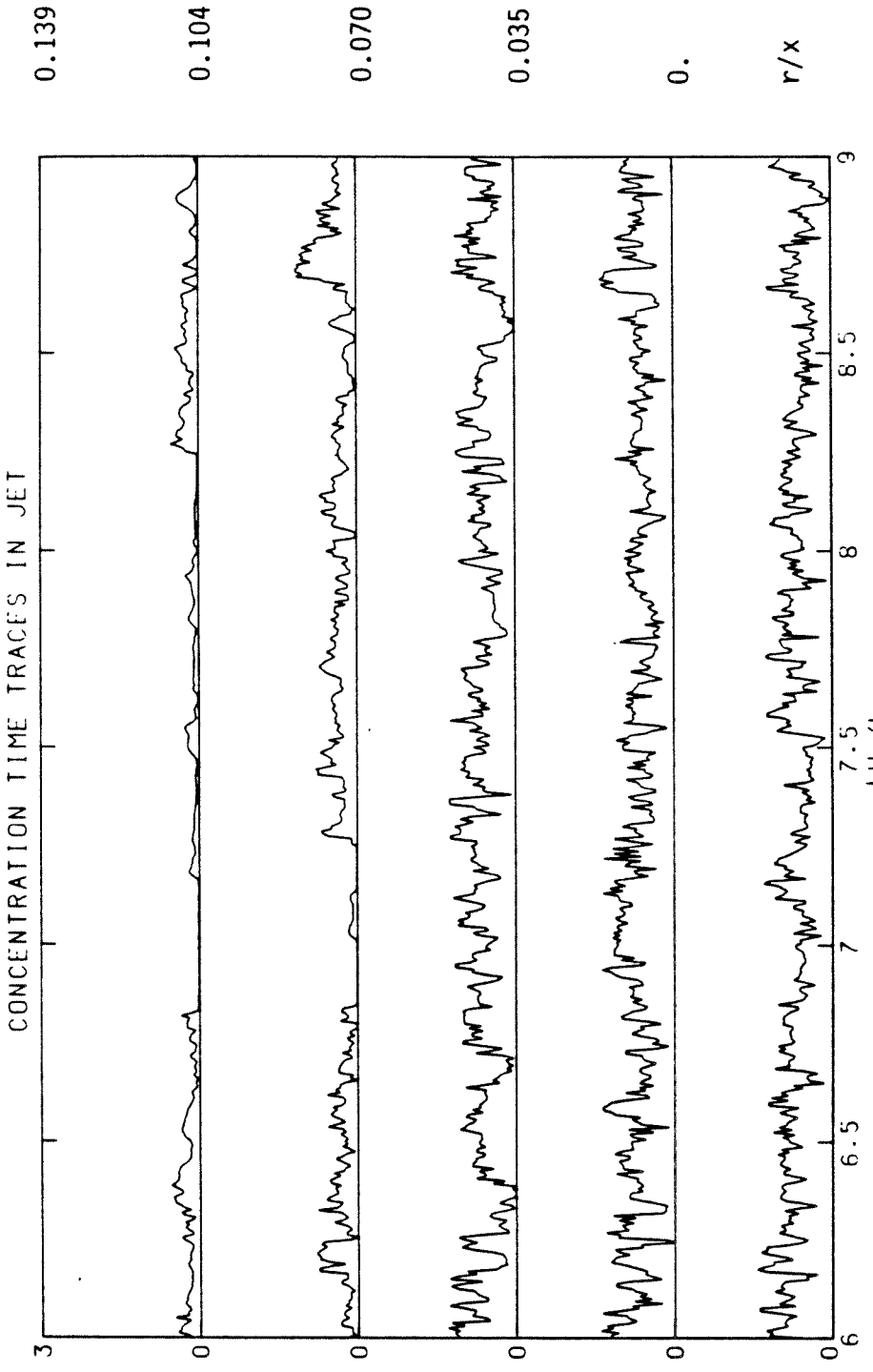

Figure 4.7. Concentration time traces at various radial positions in jet (continued).

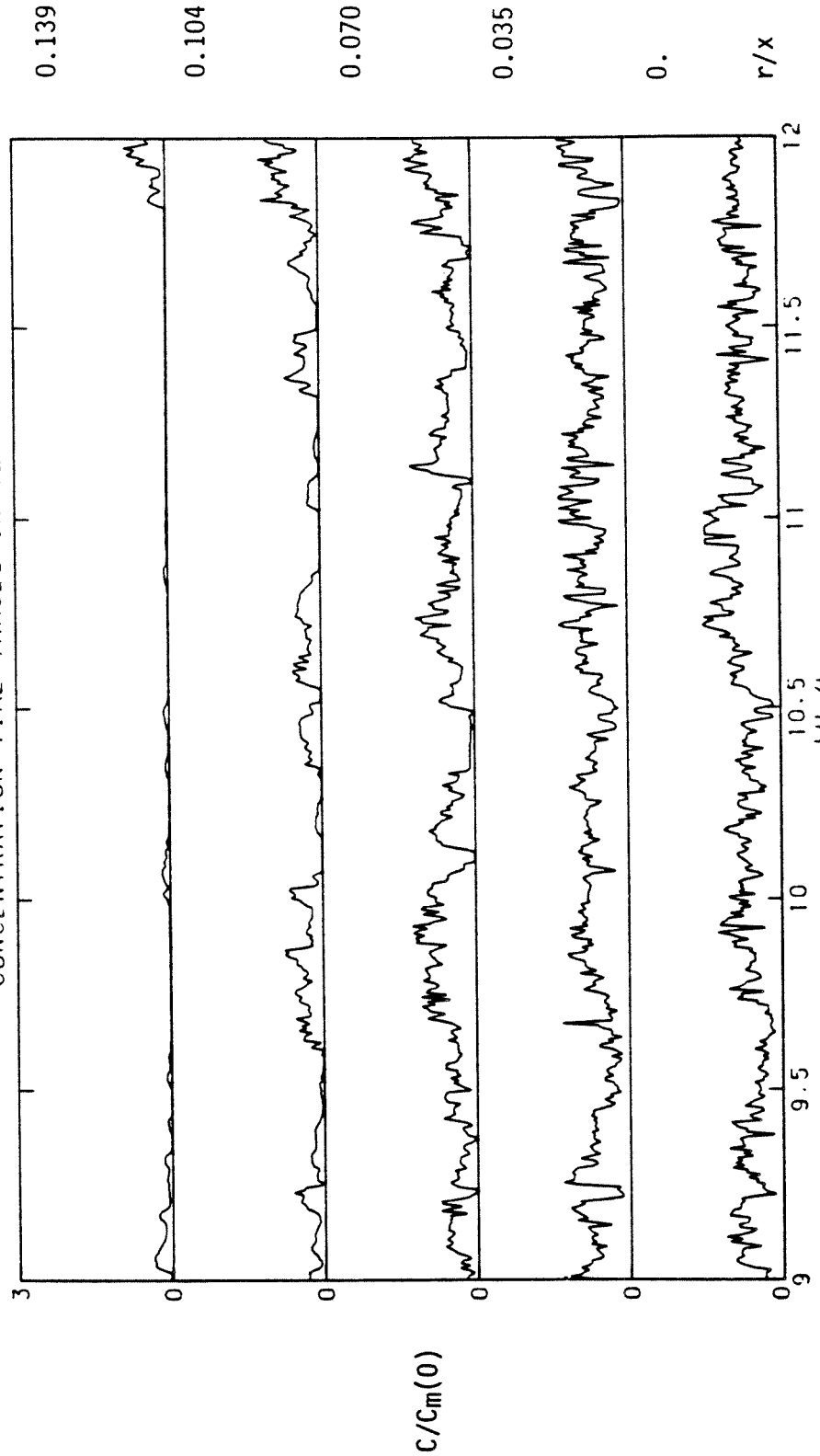

Figure 4.7. Concentration time traces at various radial positions in jet (continued).

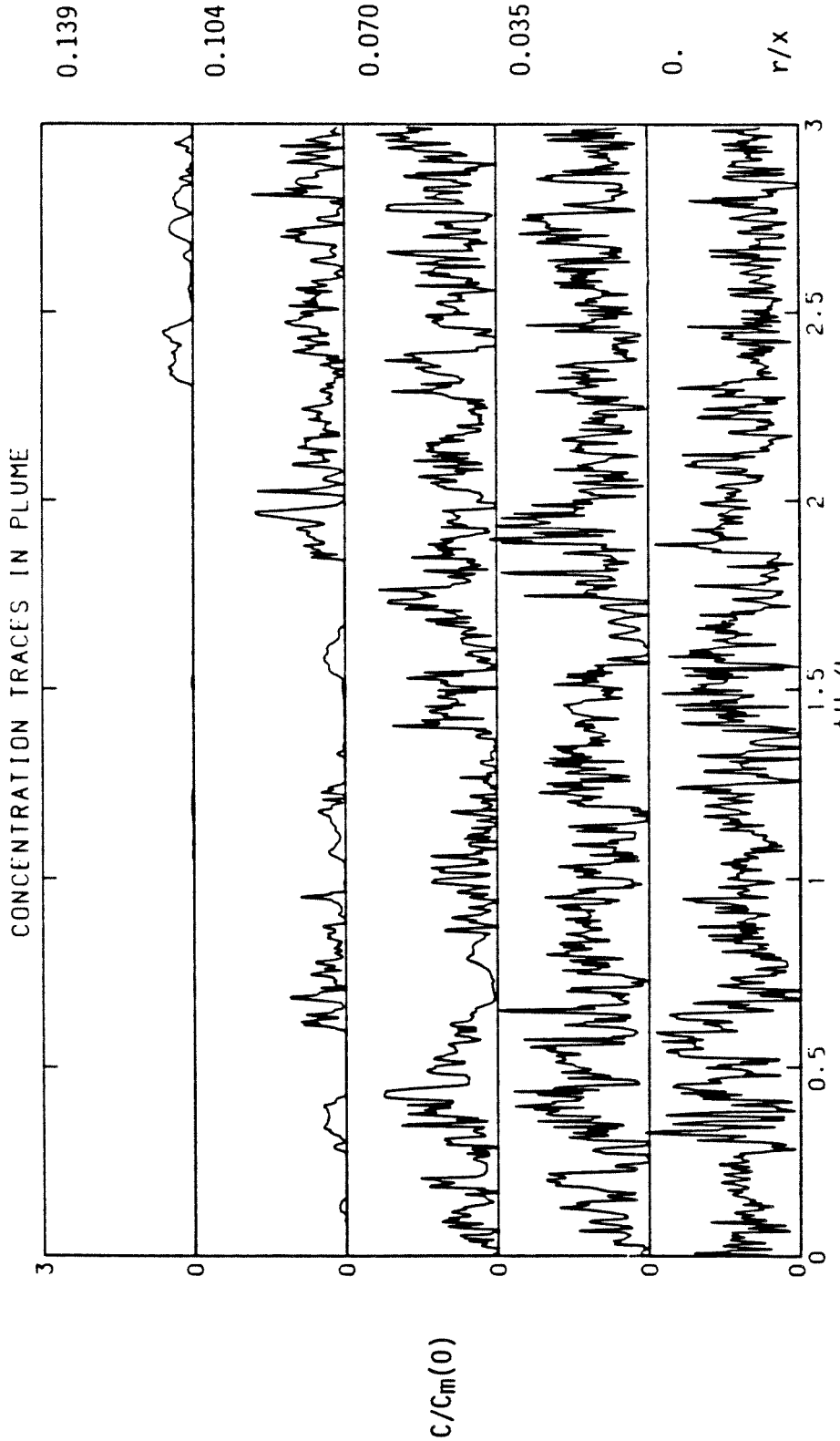

Figure 4.8. Concentration time traces at various radial positions in plume.

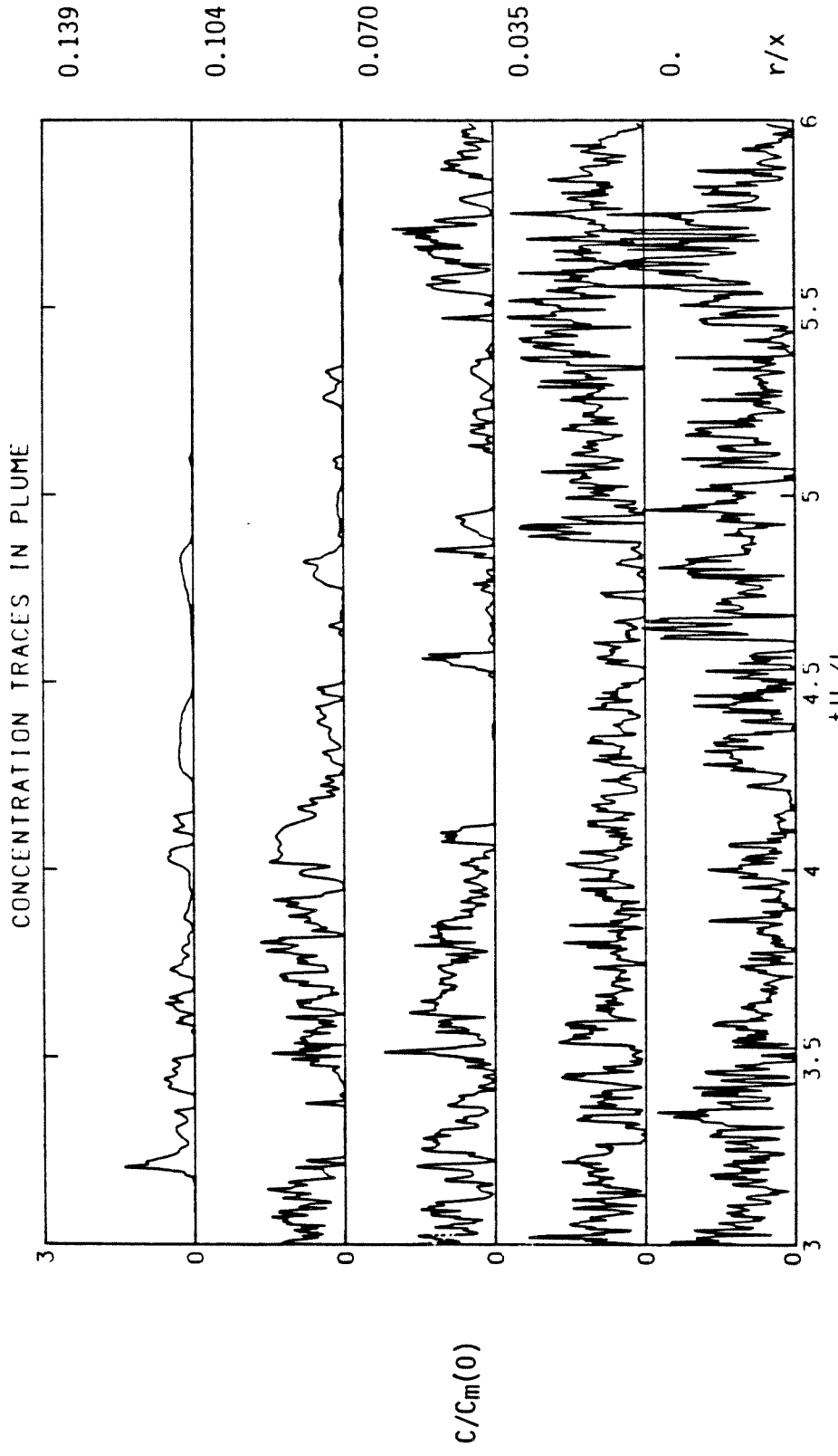

Figure 4.8. Concentration time traces at various radial positions in plume (continued).

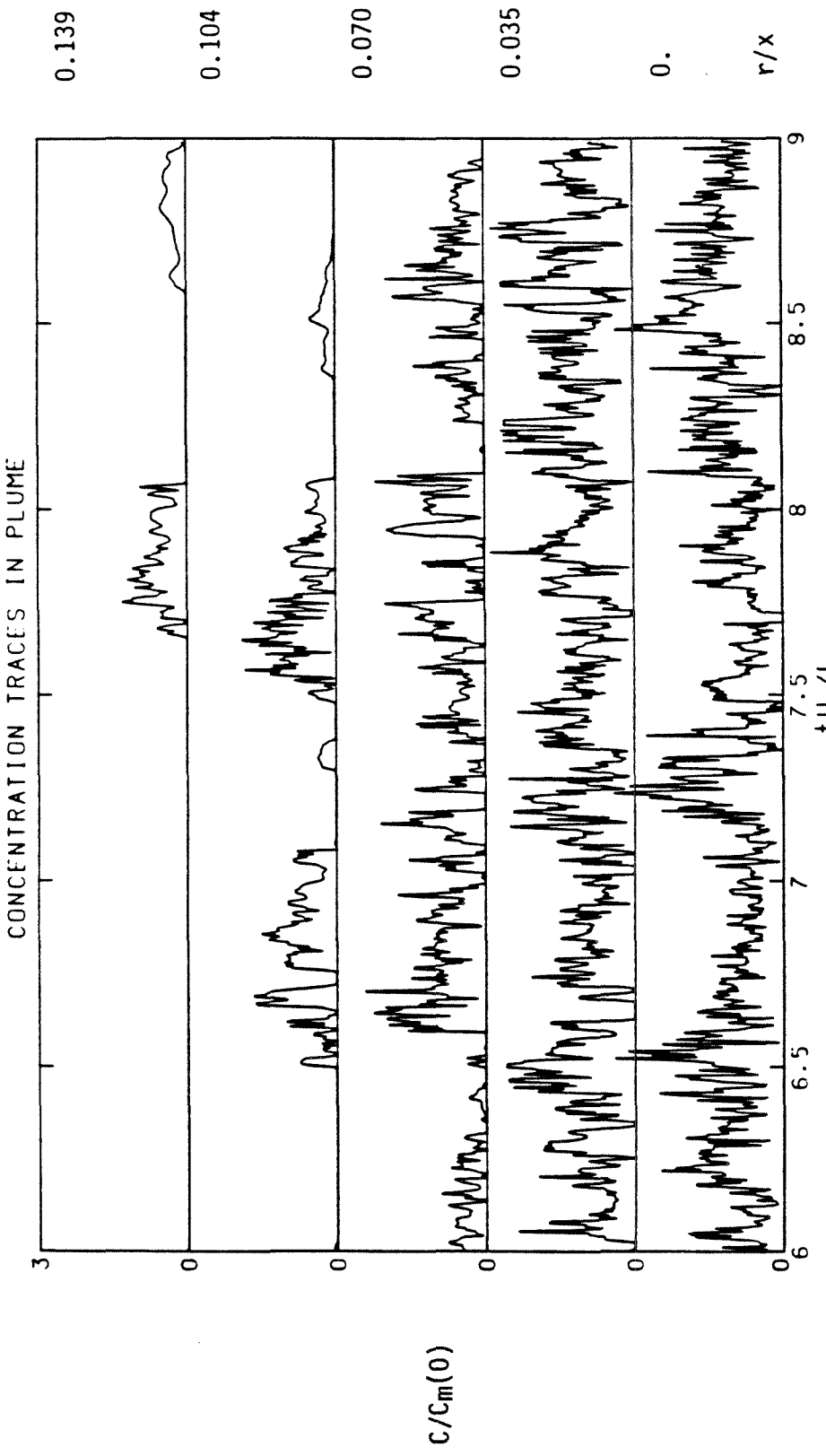

Figure 4.8. Concentration time traces at various radial positions in plume (continued).

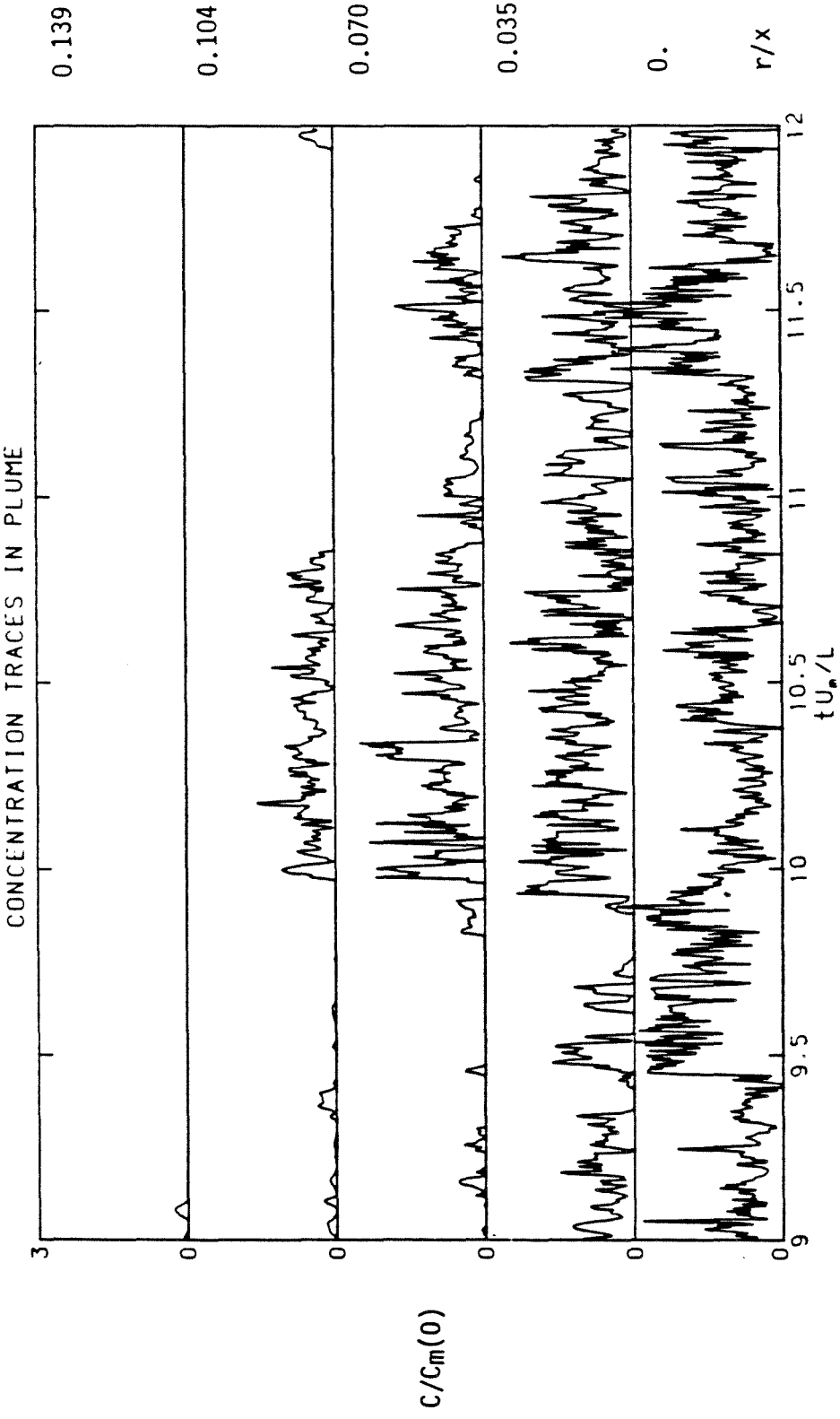

Figure 4.8. Concentration time traces at various radial positions in plume (continued).

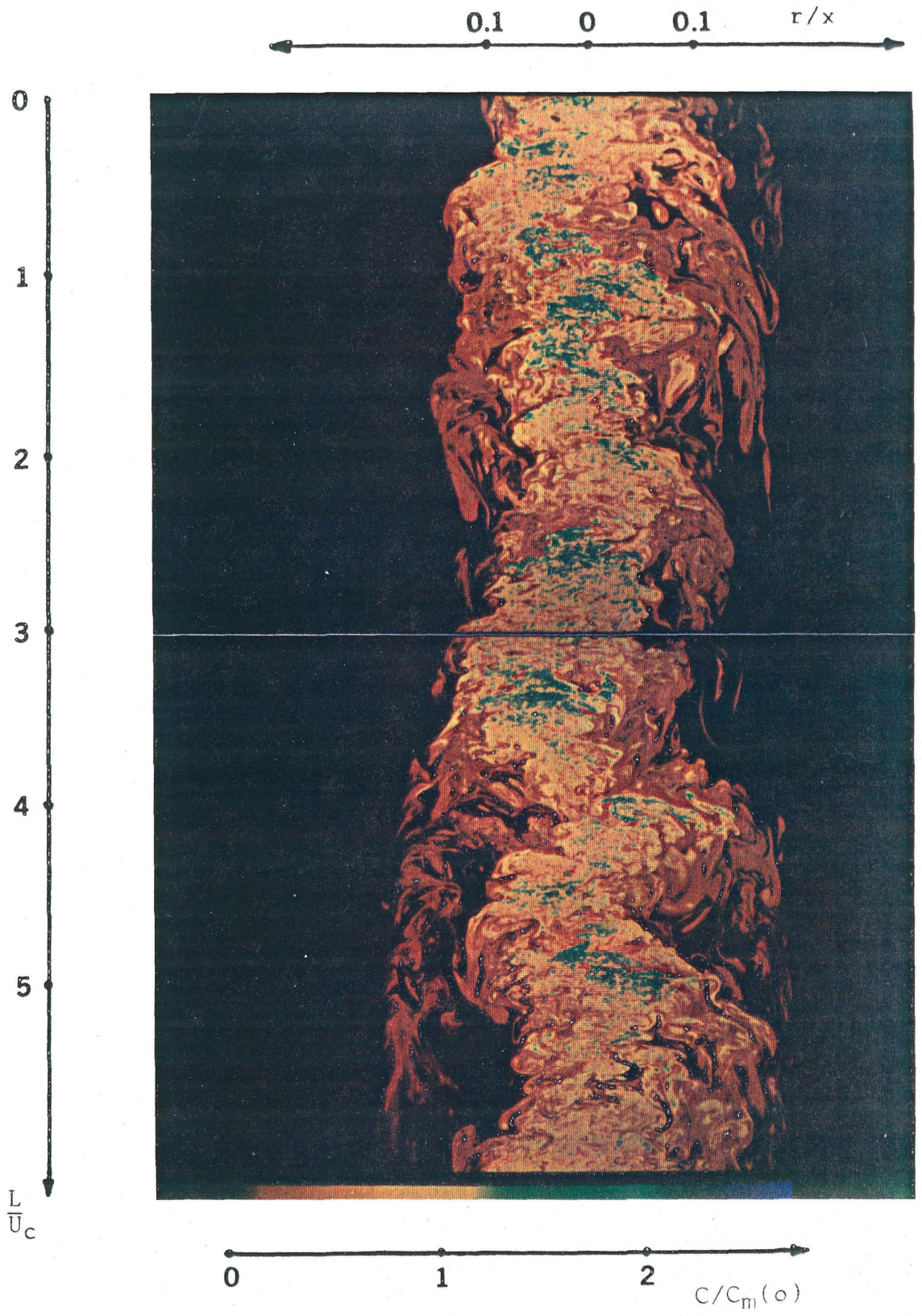

Figure 4.9. Time evolution of the instantaneous radial concentration profile in jet, Re = 5600, x/d = 150.

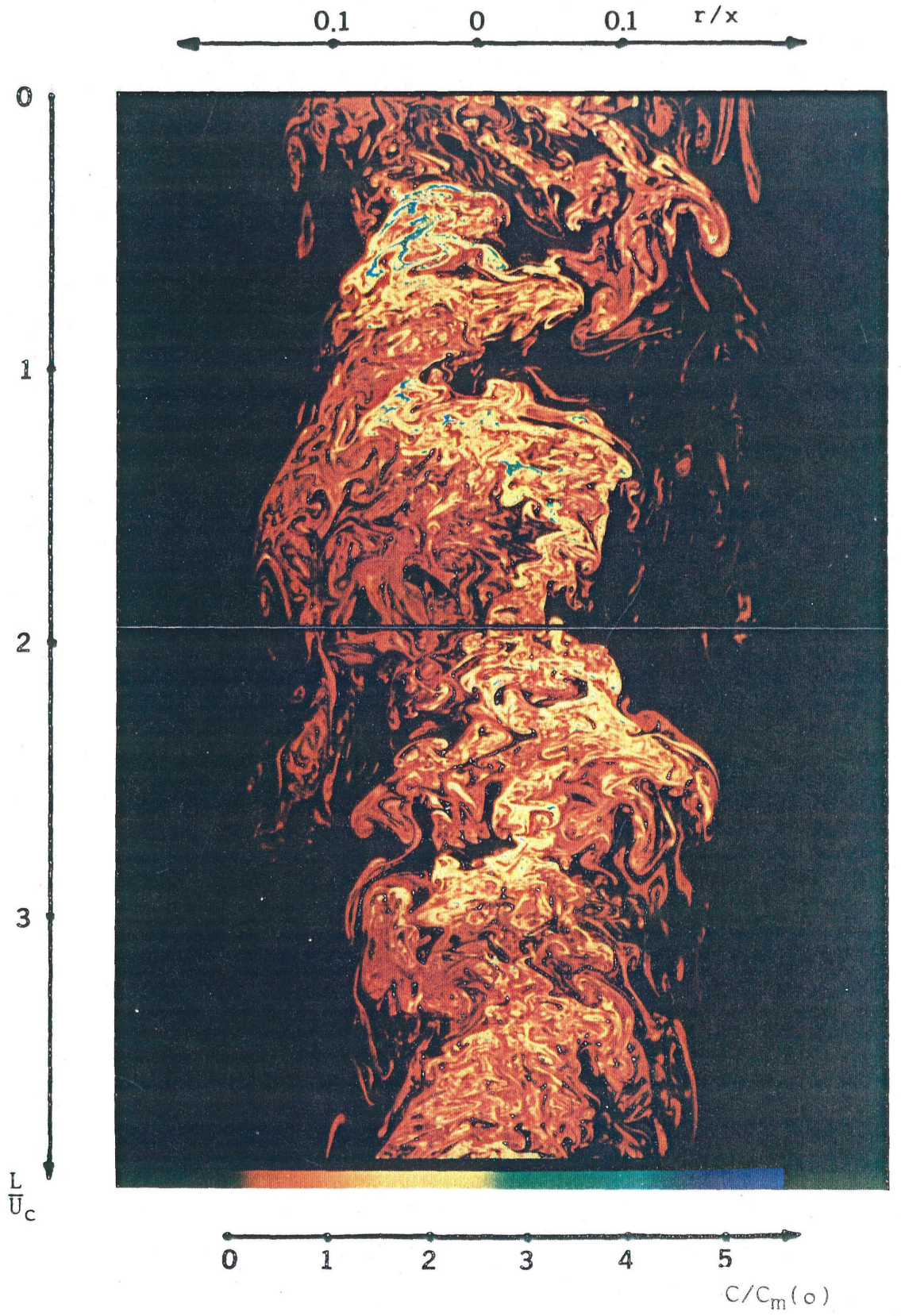

Figure 4.10. Time evolution of the instantaneous radial concentration profile in plume, x/Lm = 33, x/d = 105.

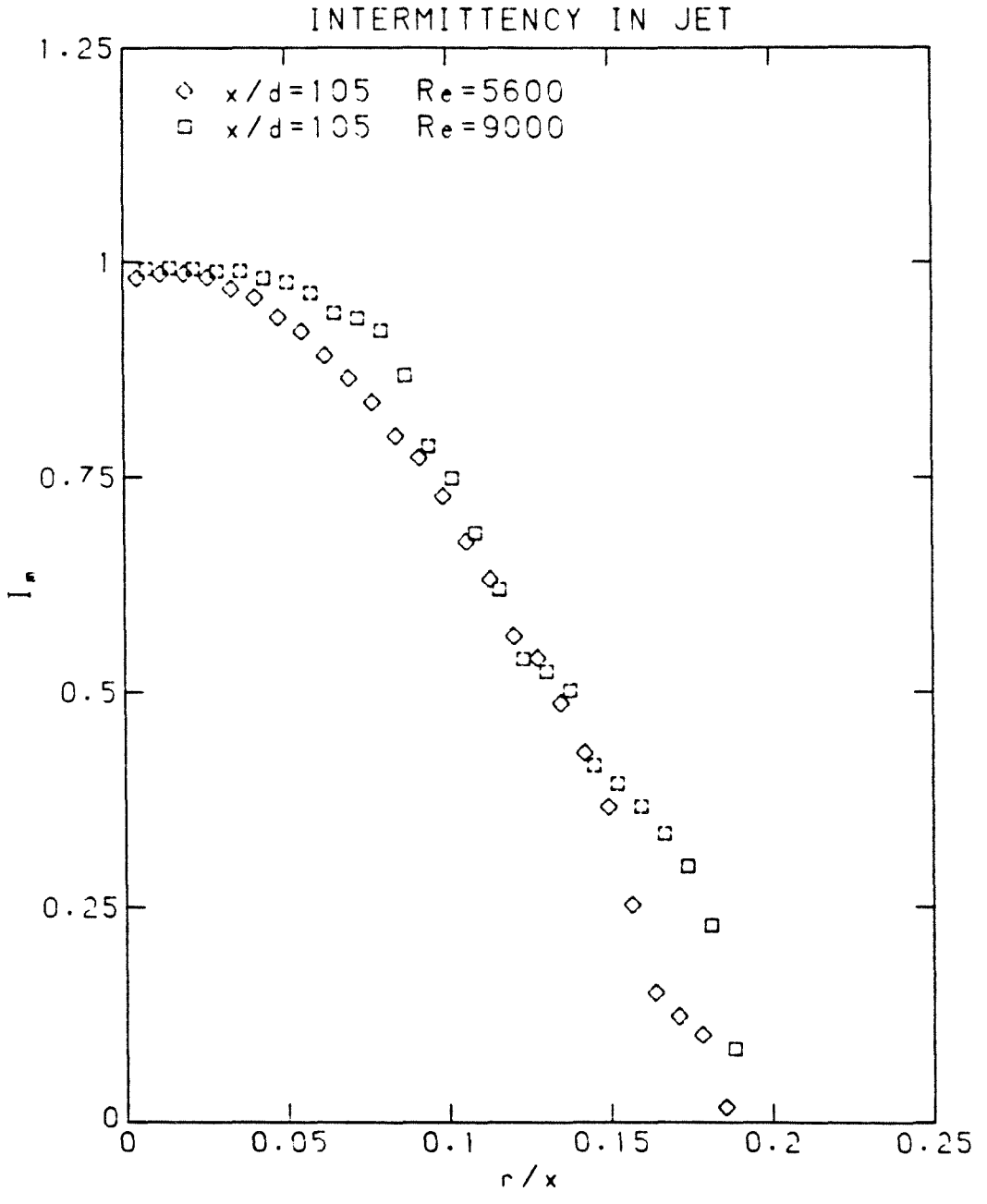

Figure 4.11. Radial profile of intermittency in jet.

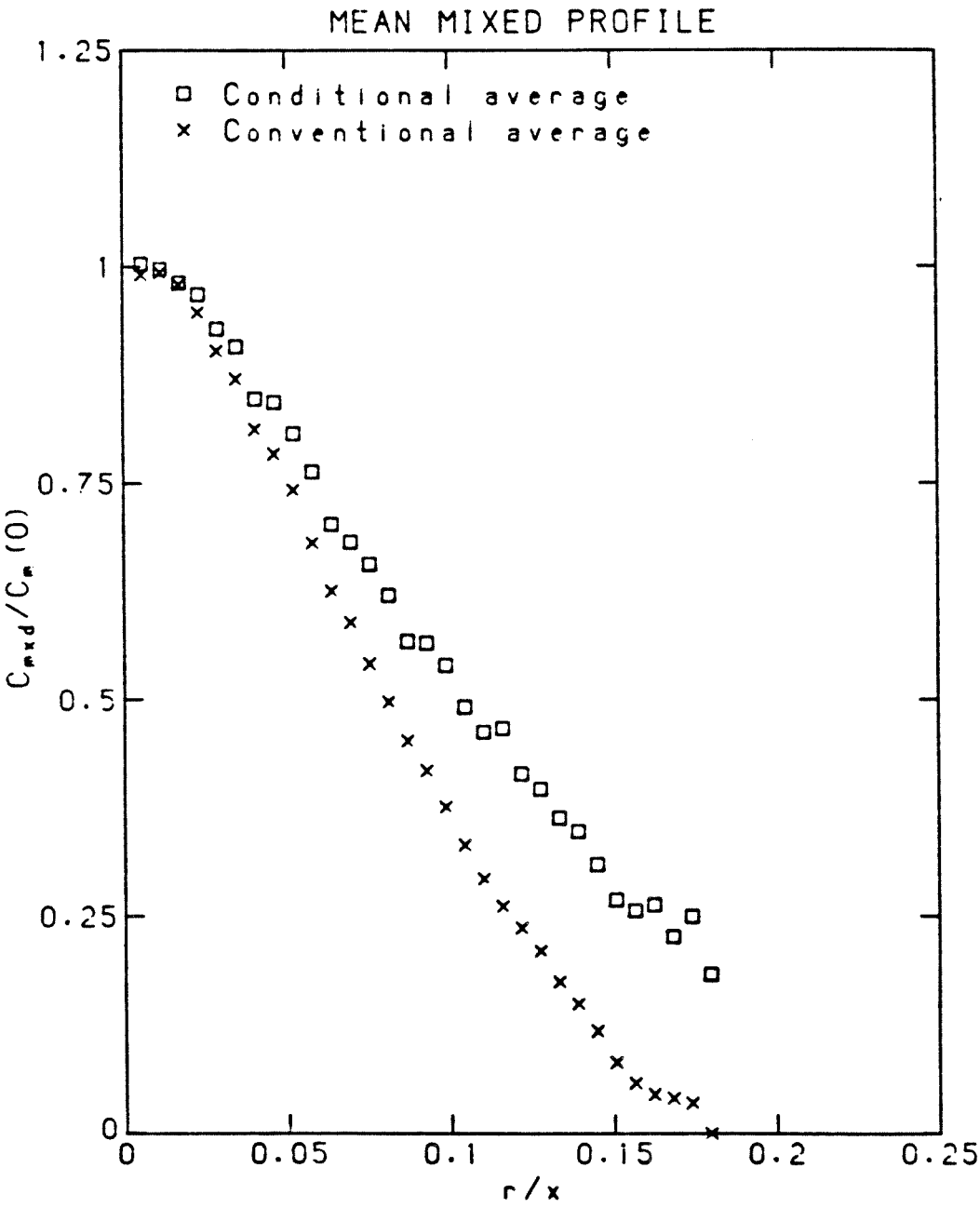

Figure 4.12. Radial profile of mean mixed concentration in jet.

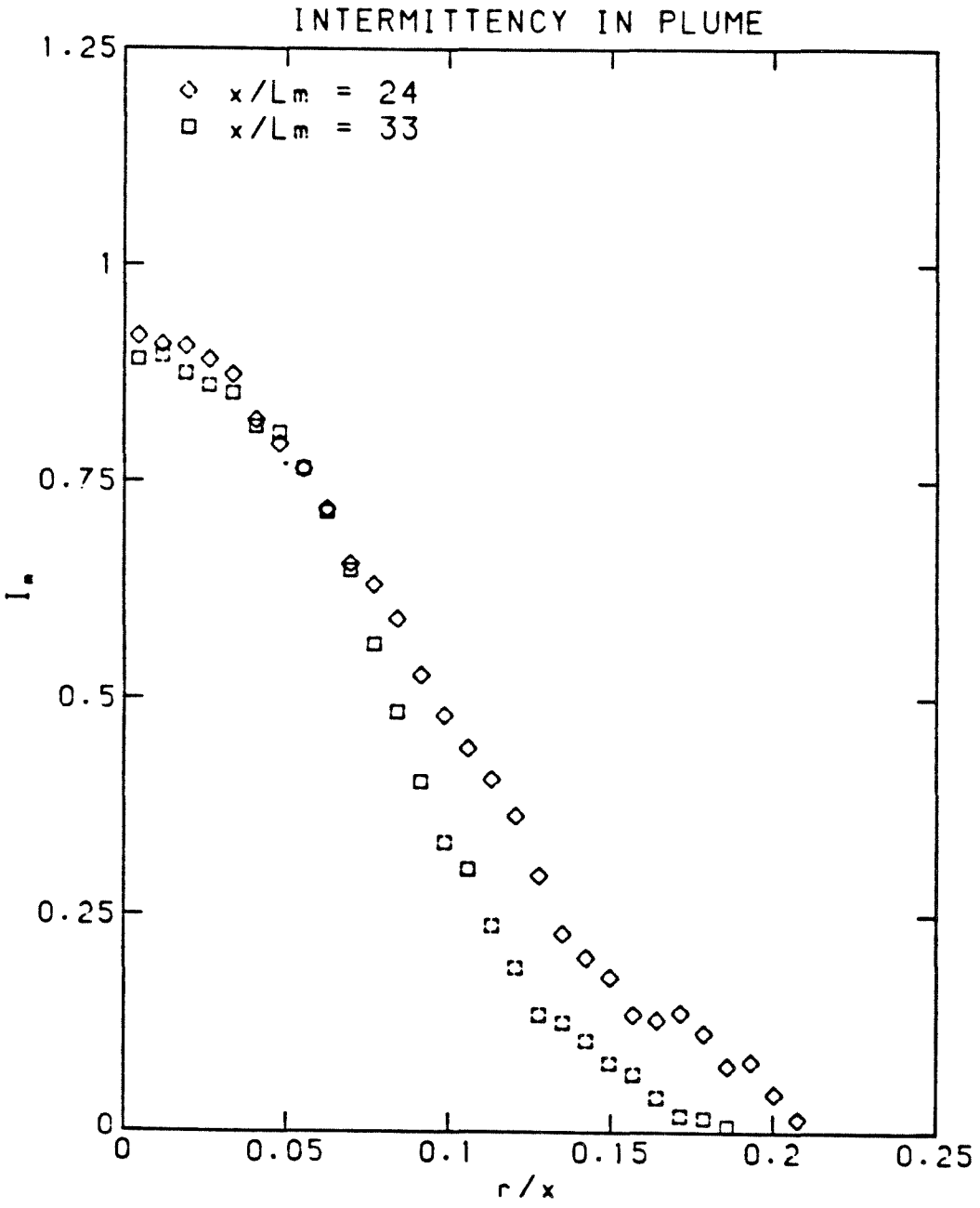

Figure 4.13. Radial profile of intermittency in plume.

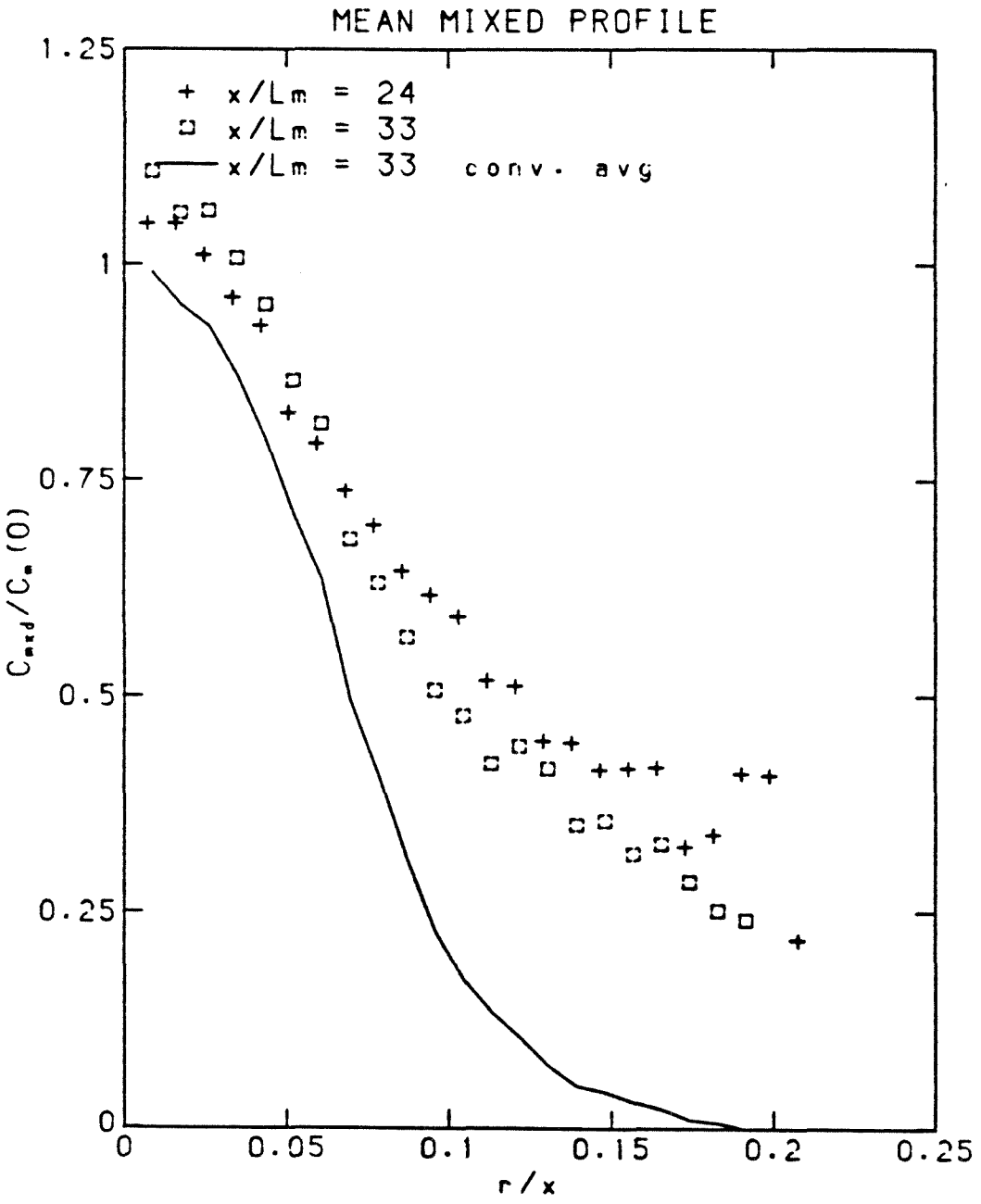

Figure 4.14. Radial profile of mean mixed concentration in plume.

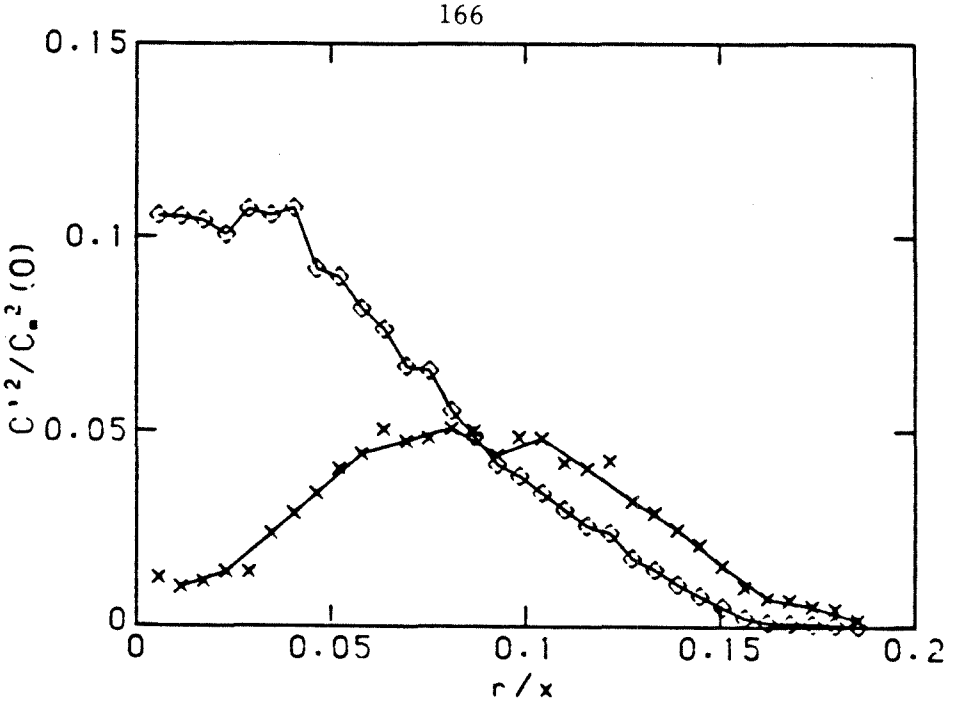

Figure 4.15. Radial profile of contributions to concentration variance from unmixed fluid and mixed fluid in jet.

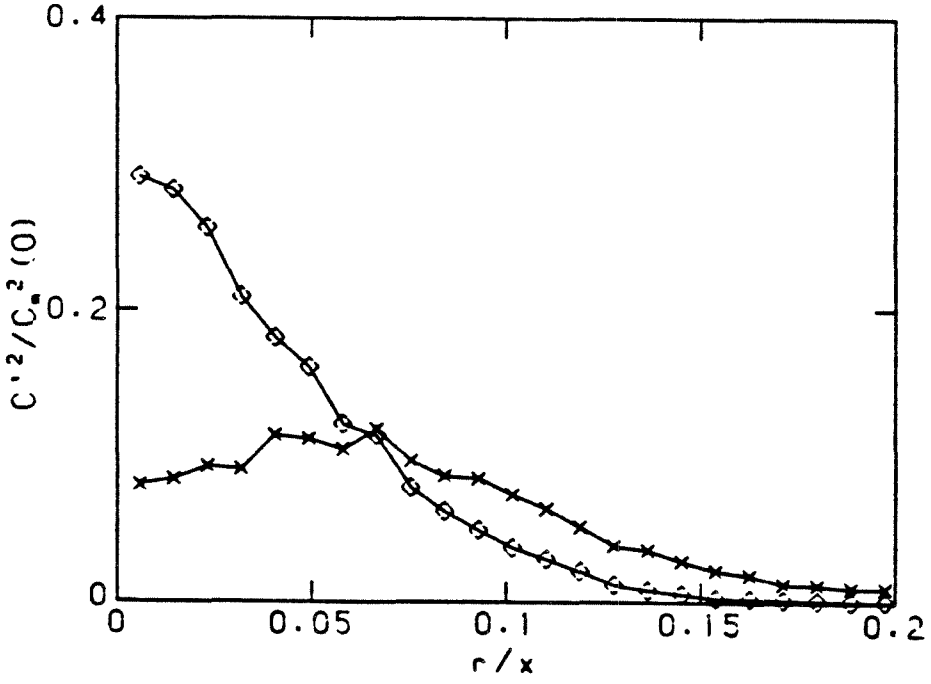

Figure 4.16. Radial profile of contributions to concentration variance from unmixed fluid and mixed fluid in plume.

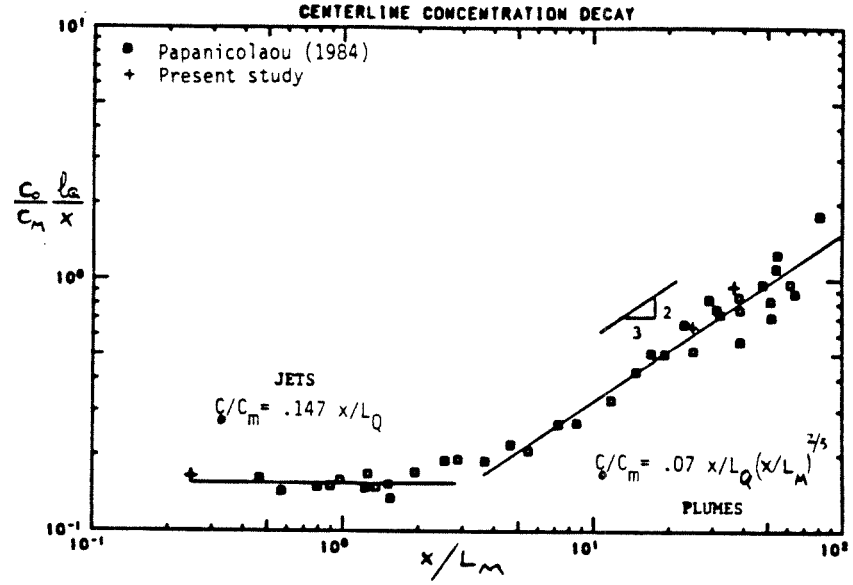

Figure 4.17a. Variation of mean centerline concentration in buoyant jet with non-dimensional axial distance from source.

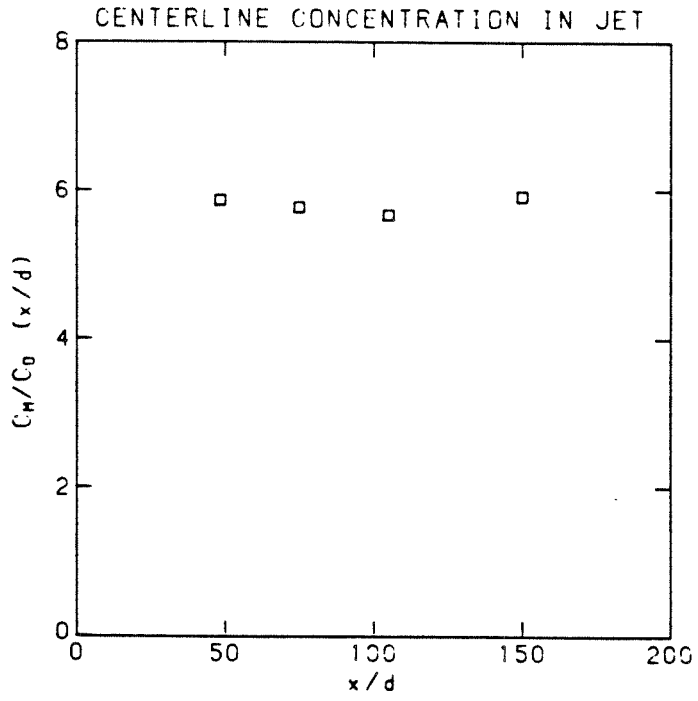

Figure 4.17b. Variation of mean centerline concentration in momentum jet with non-dimensional axial distance from source.

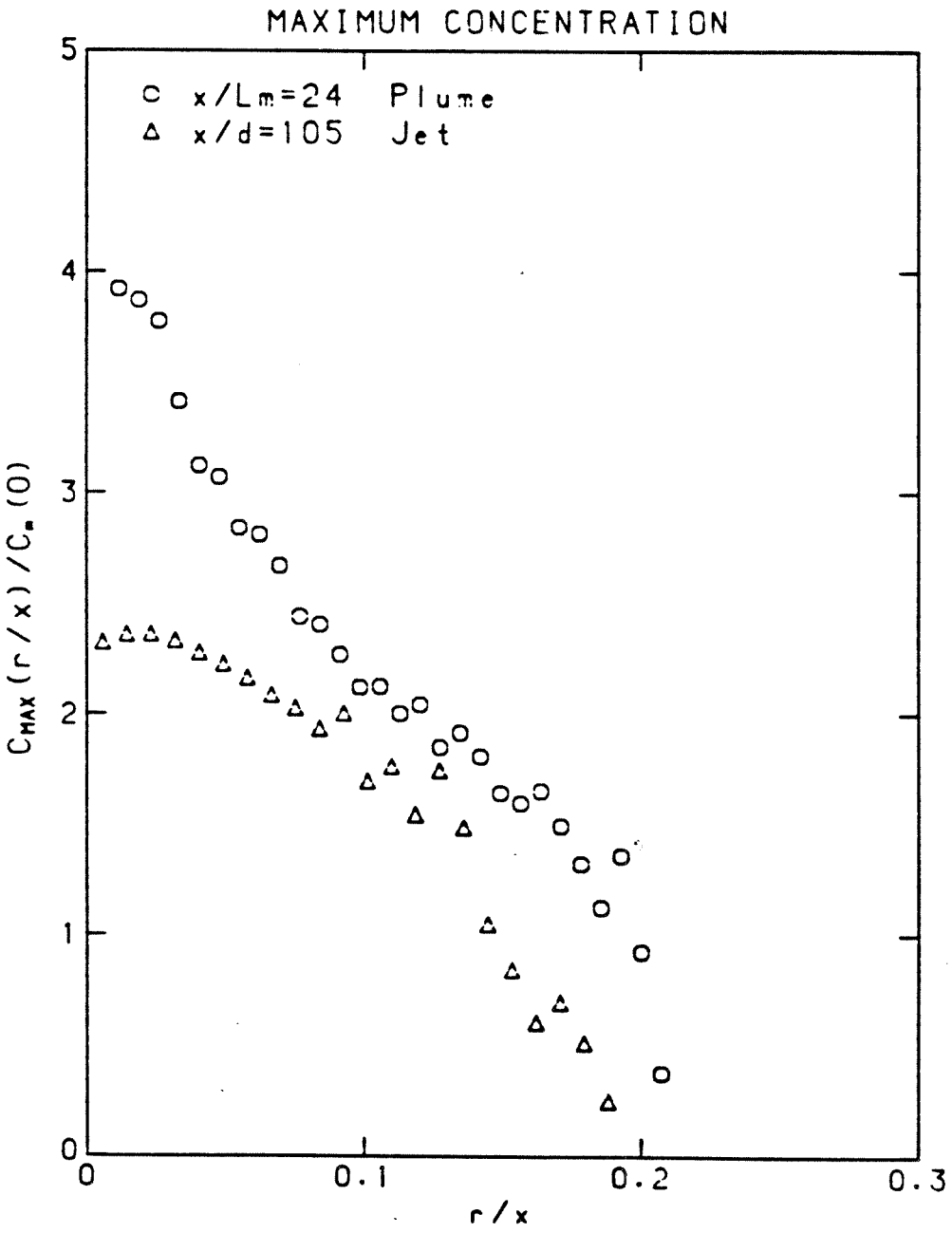

Figure 4.18. Maximum normalized concentration as a function of radial position in jet and plume.

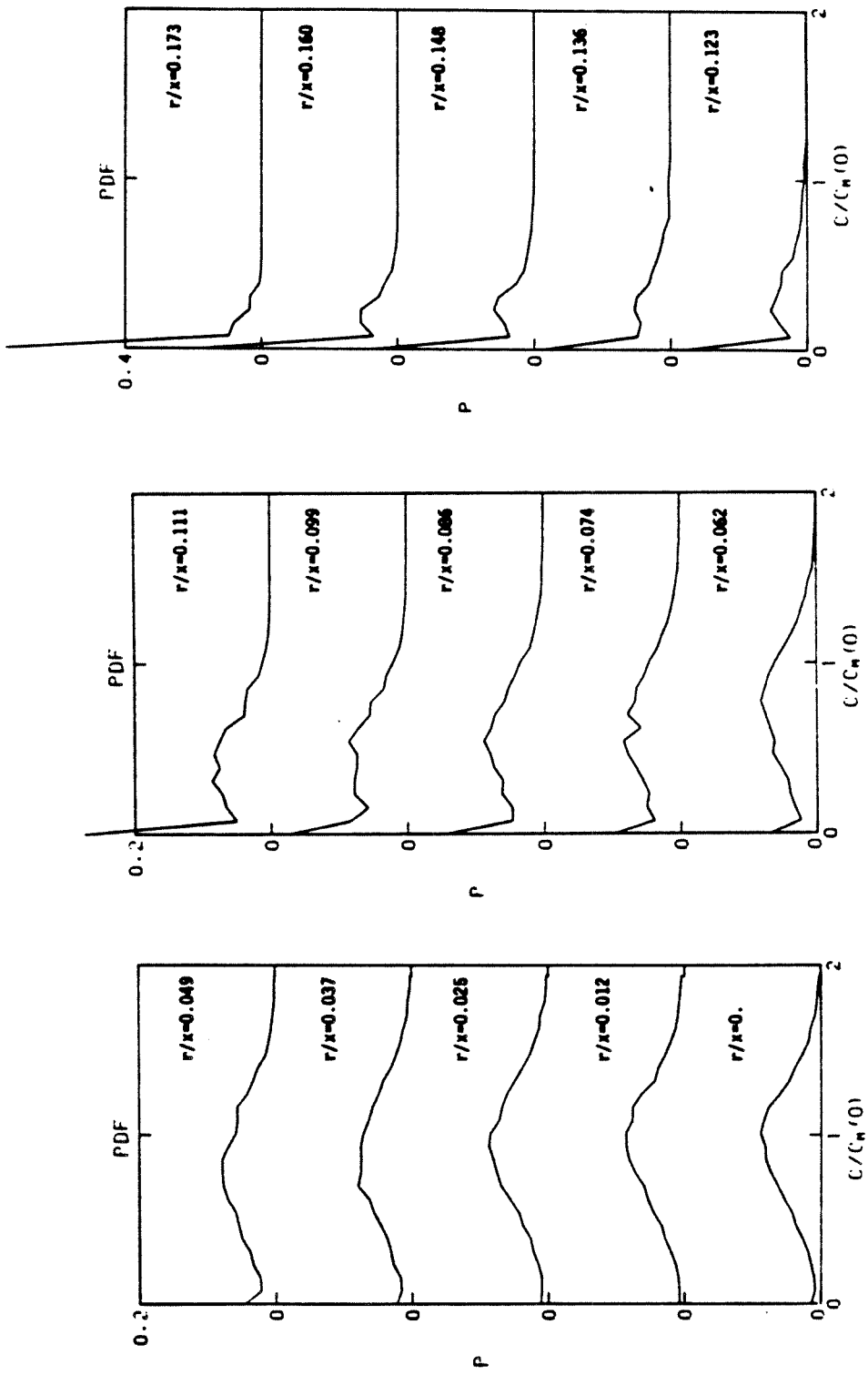

Figure 4.19a. PDF of normalized concentration as a function of radial position in jet.

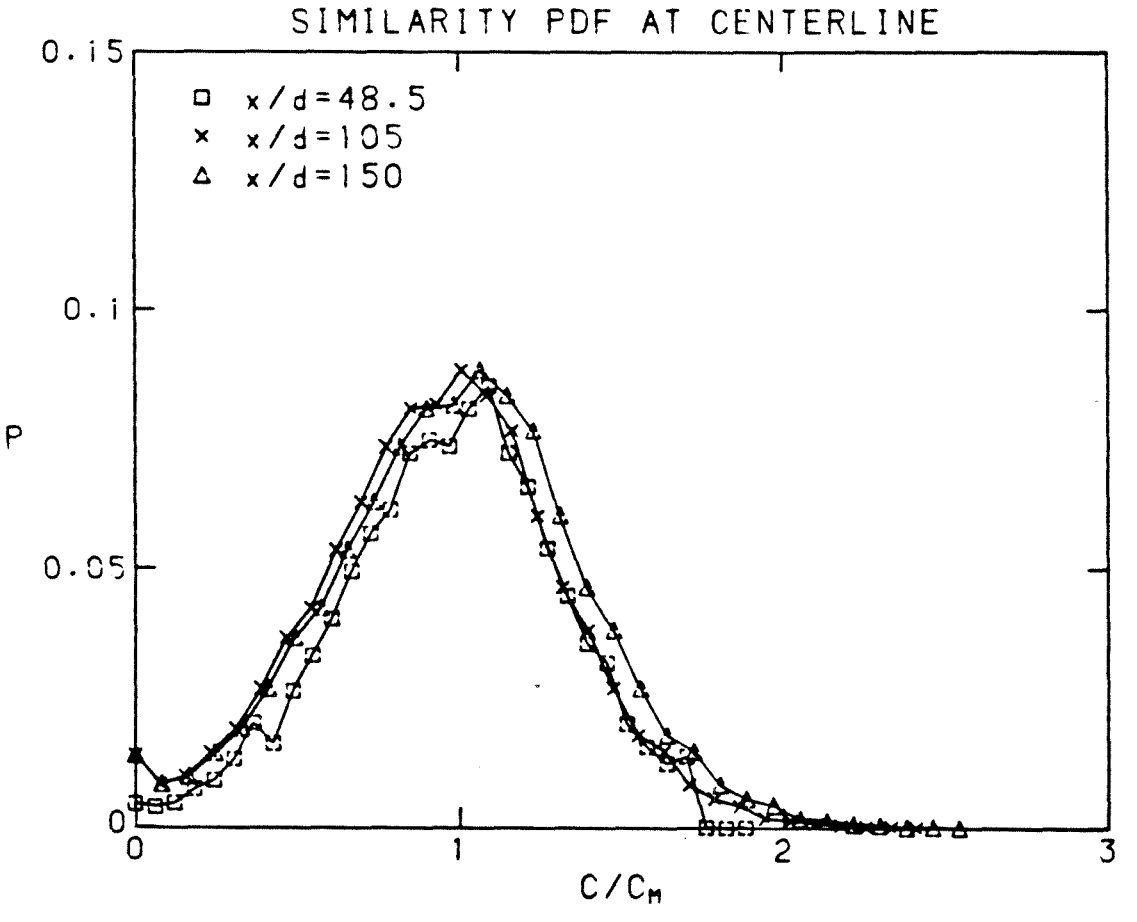

Figure 4.19b. PDF of normalized concentration at jet centerline as a function the nondimensional axial distance.

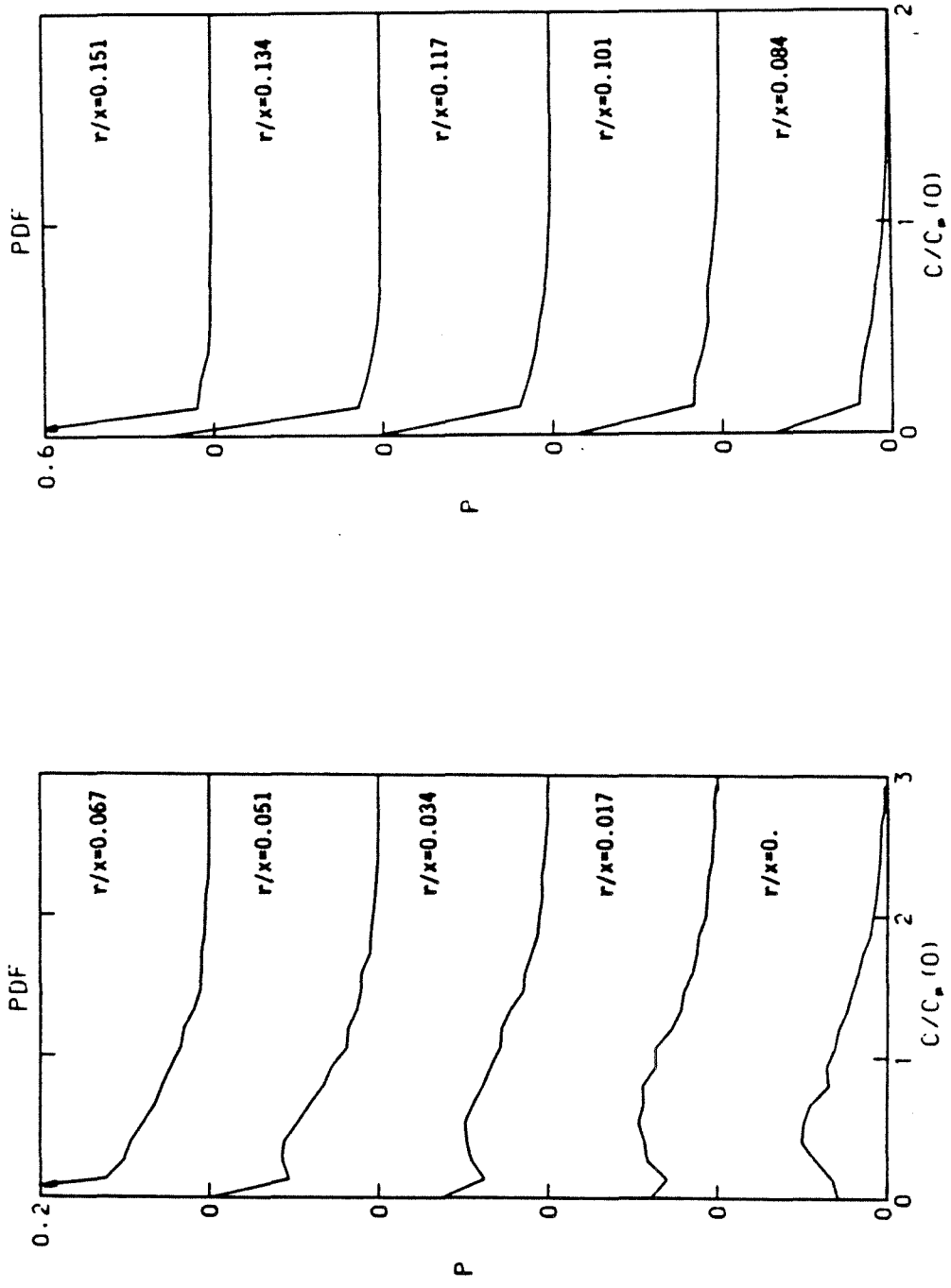

Figure 4.20a. PDF of normalized concentration as a function of radial position in plume.

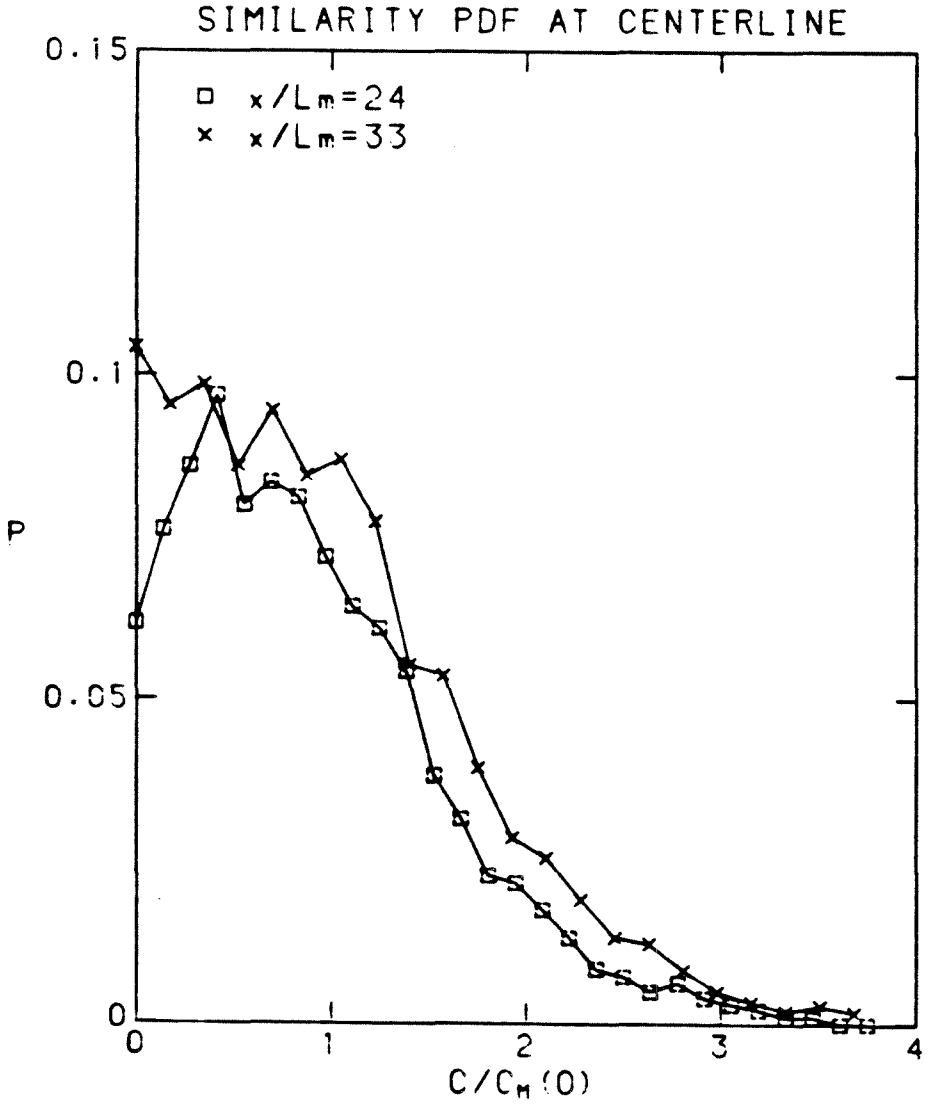

Figure 4.20b. PDF of normalized concentration at plume centerline as a function of nondimensional axial distance.

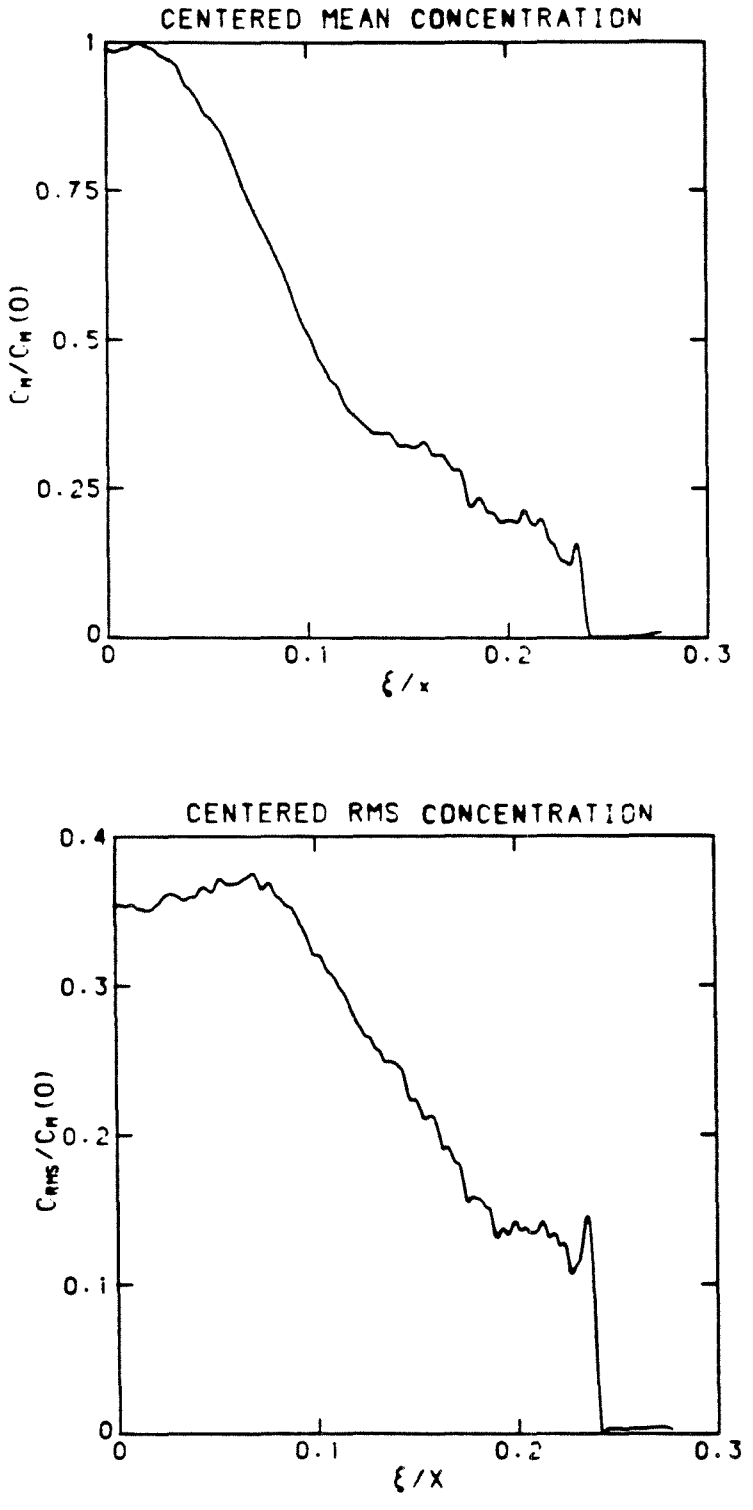

Figure 4.21. Radial profile of concentration in jet based on instantaneous jet center.

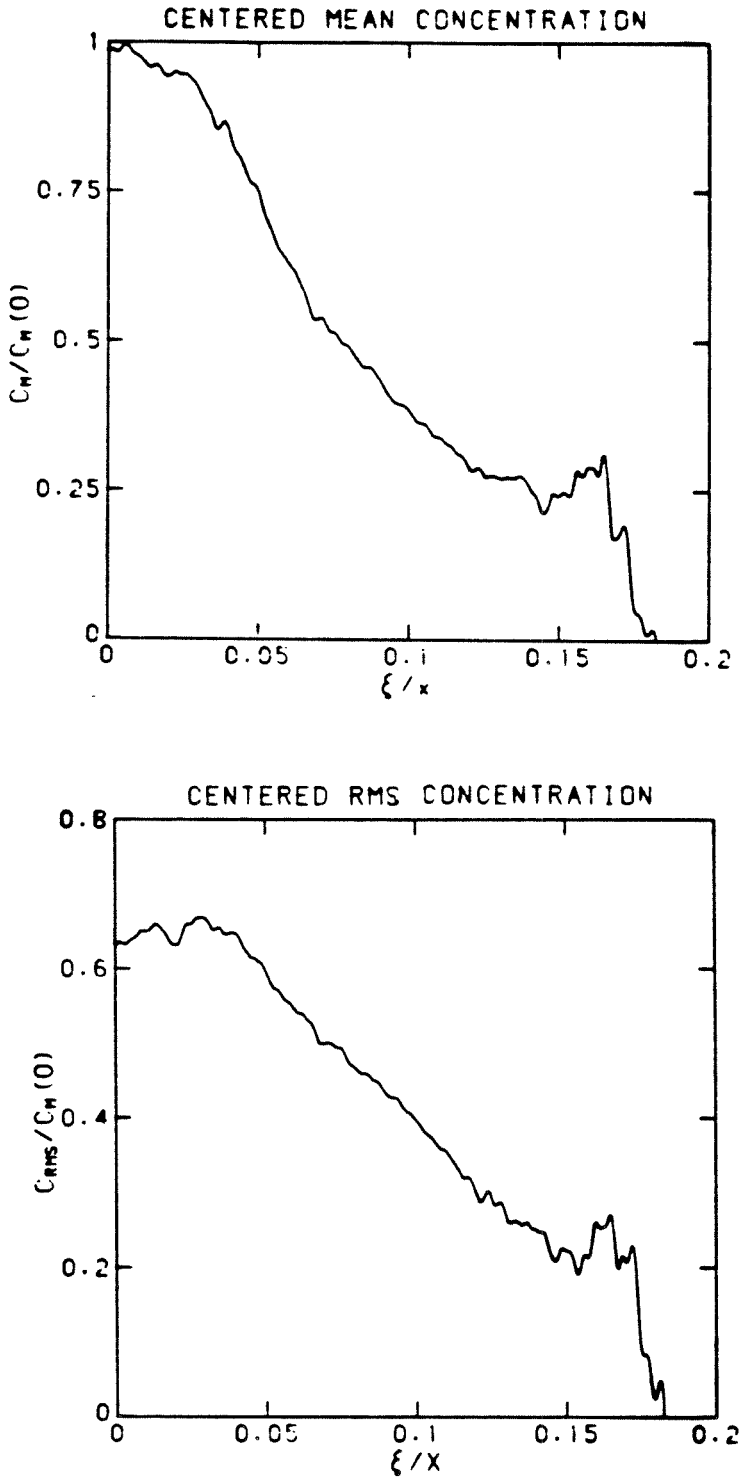

Figure 4.22. Radial profile of concentration in plume based on instantaneous plume center.

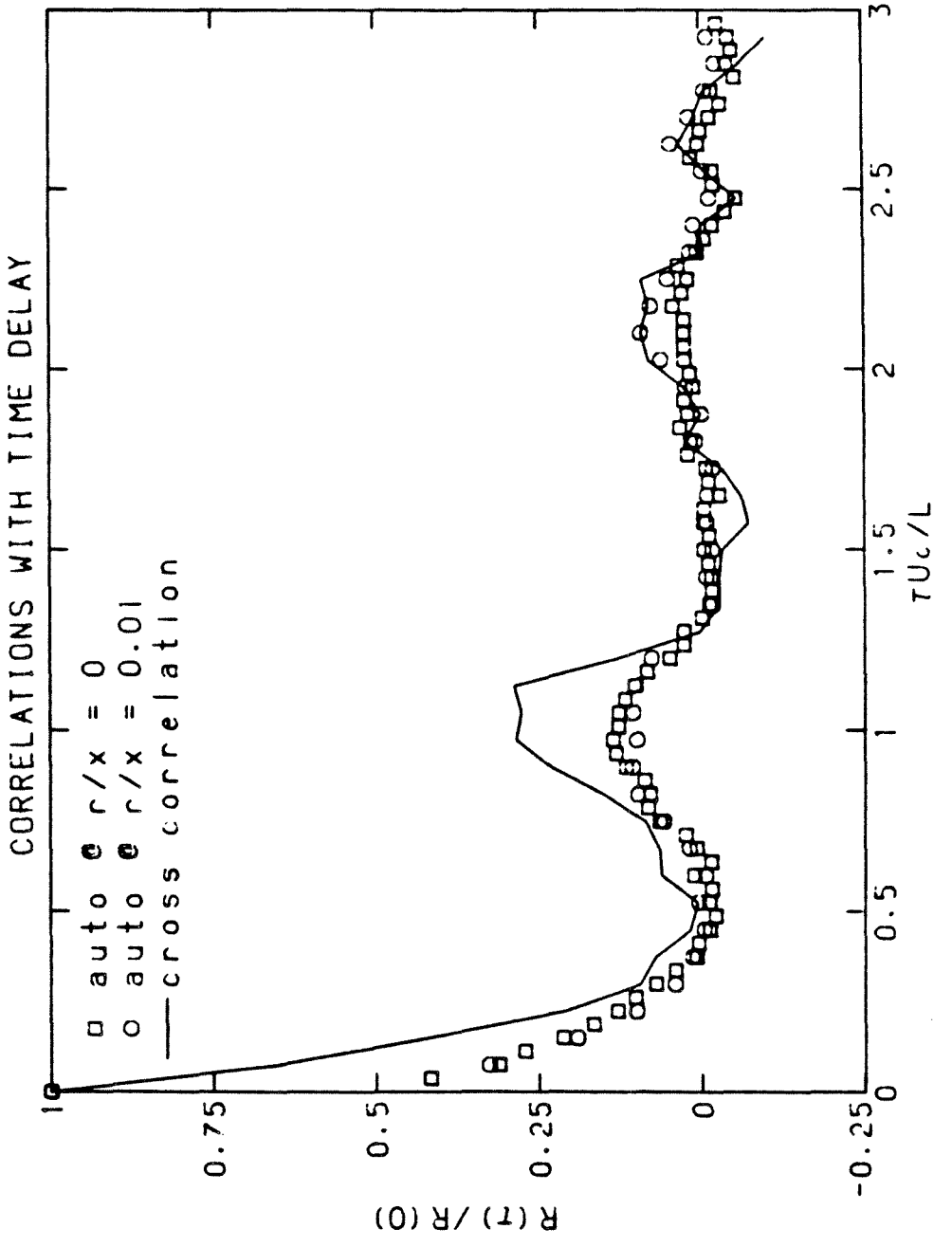

Figure 4.23a. Normalized correlation functions with variable time delay in jet.

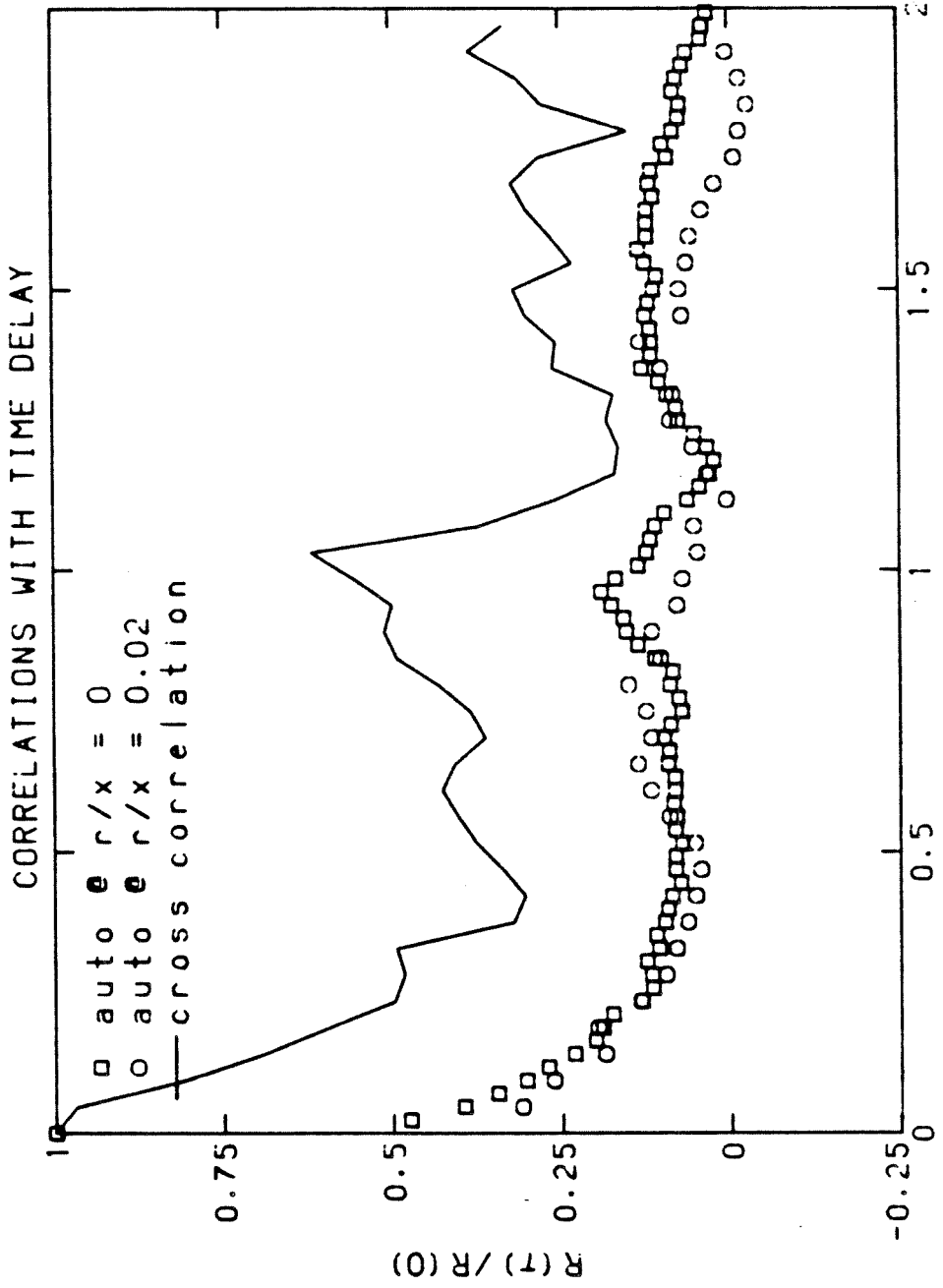

Figure 4.23b. Normalized correlation functions with variable time delay in plume.

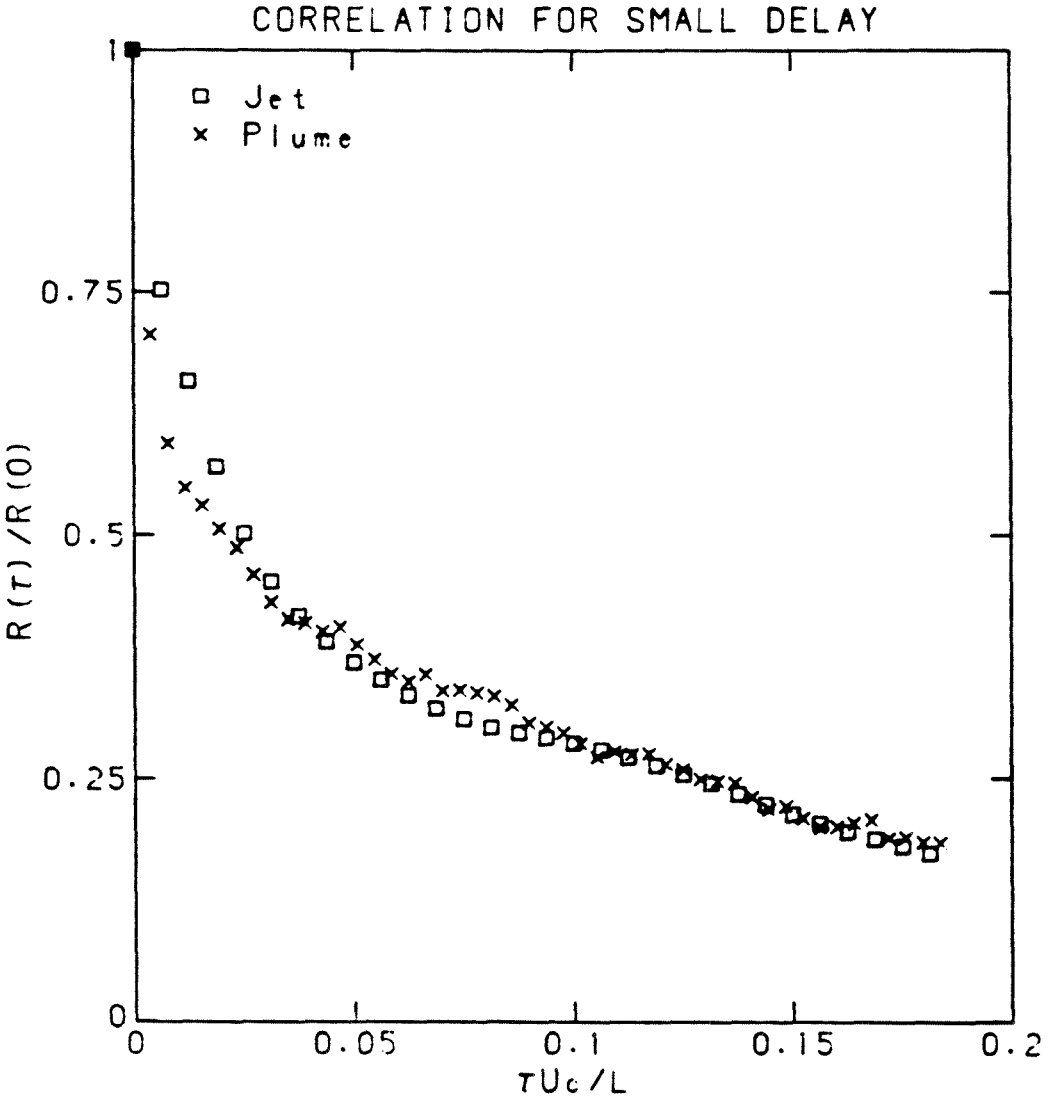

Figure 4.23c. Normalized autocorrelation function for small time delay at centerline.

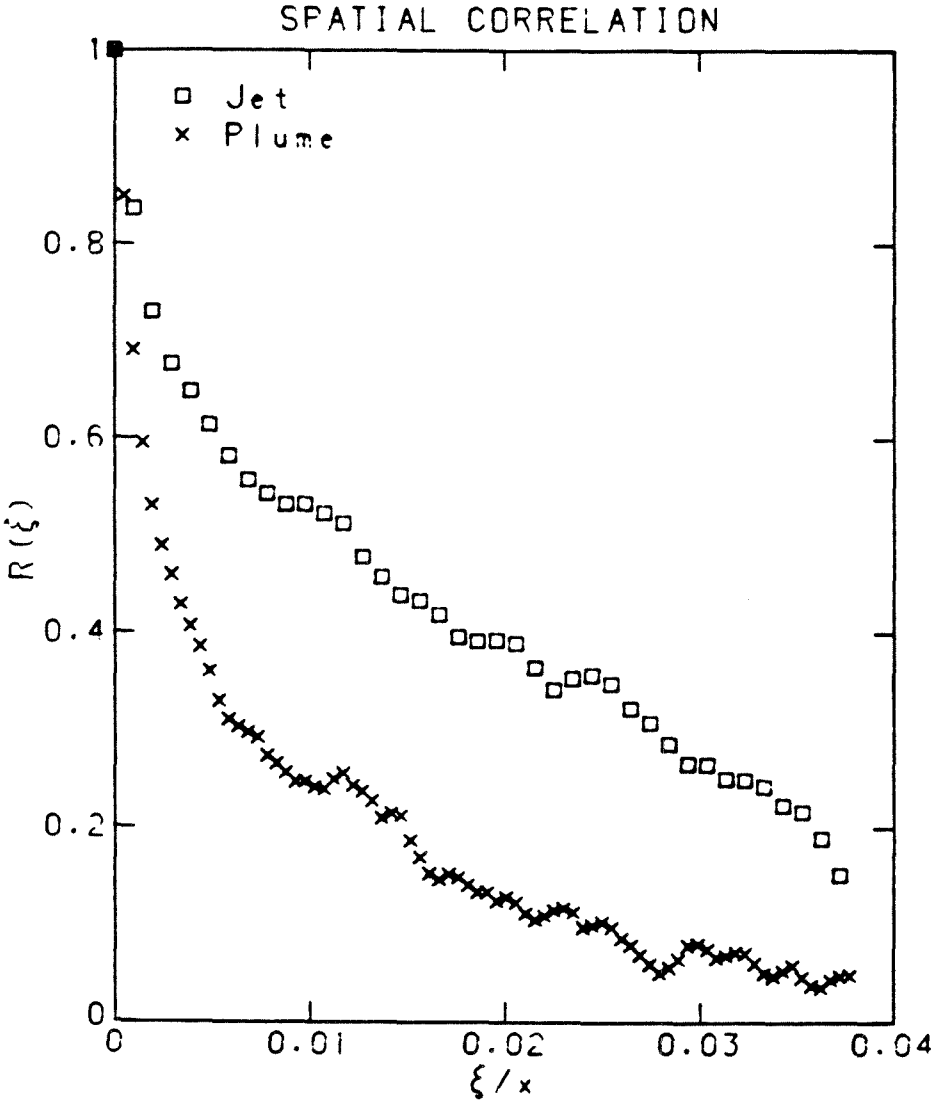

Figure 4.24. Spatial correlation function.

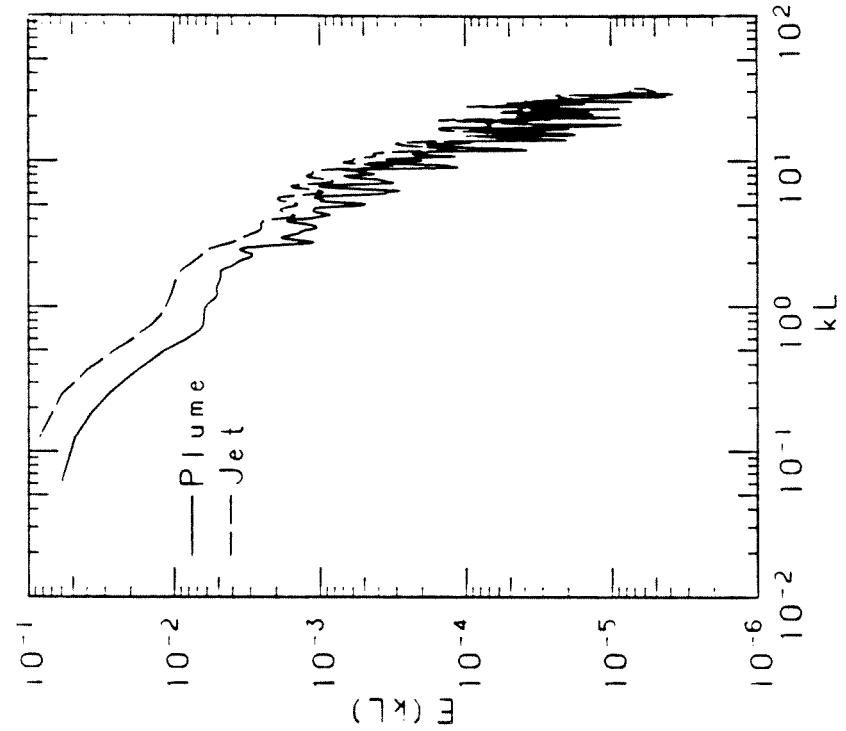

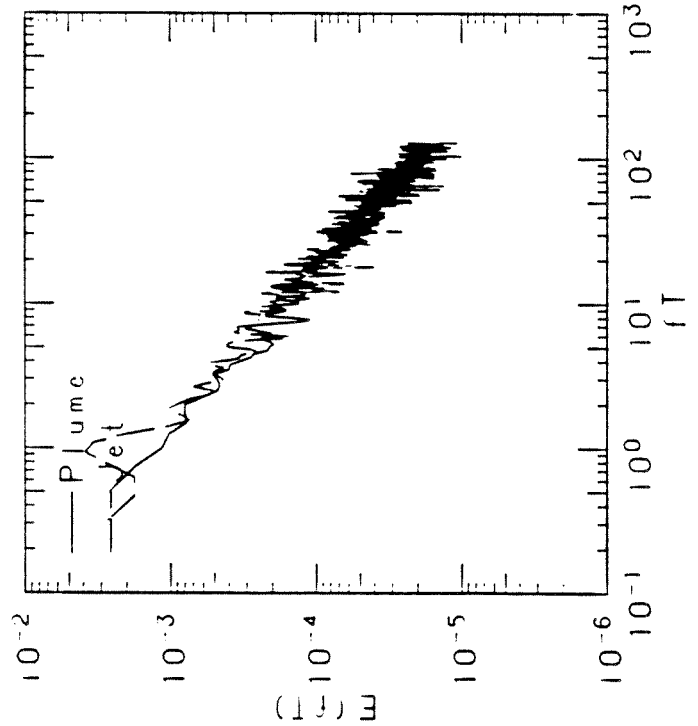

Figure 4.25a. Spectral density of concentration fluctuations as a function of the normalized frequency.

Figure 4.25b. Spectral density of concentration fluctuations as a function of the normalized wavenumber.

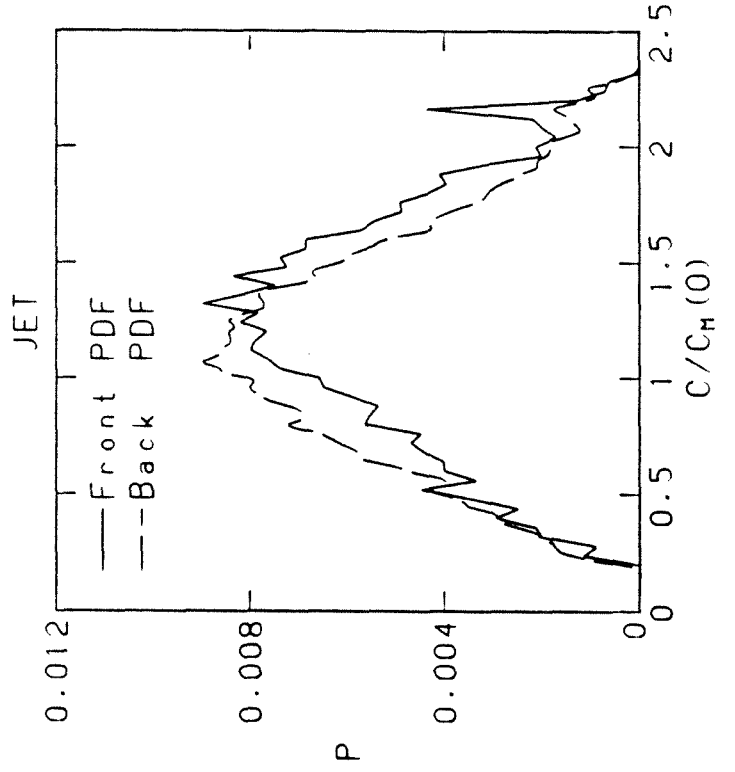

Figure 4.26a Ensemble average distributions of excursions in the normalized concentration signal in jet.

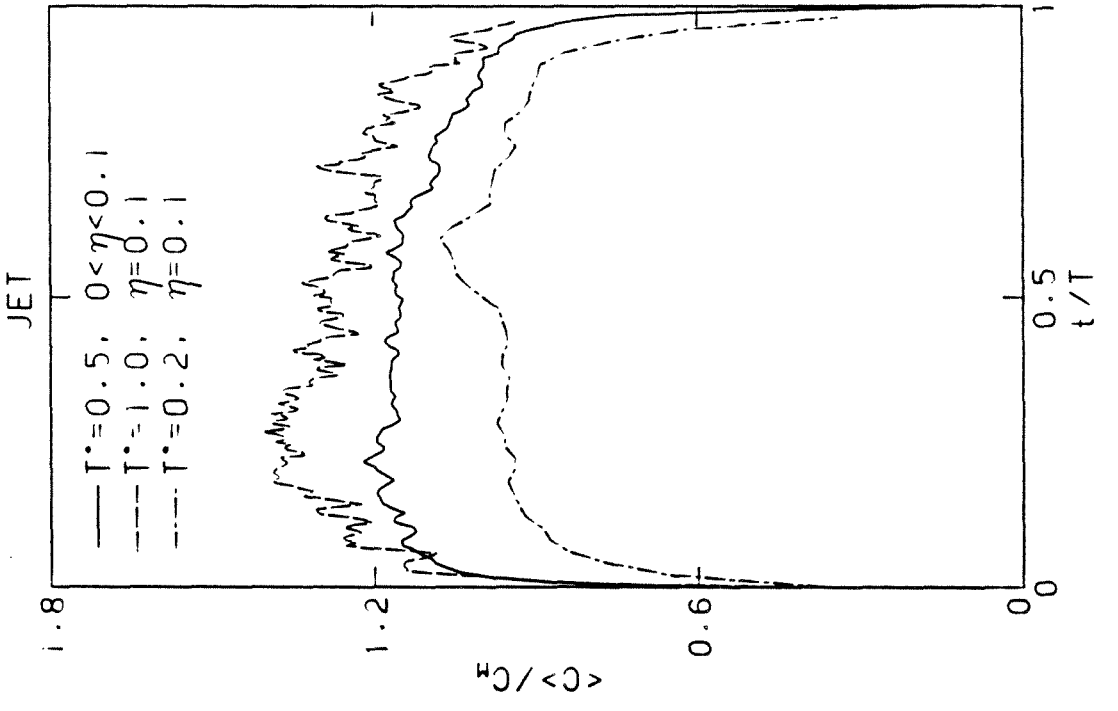

Figure 4.26b PDF of concentration in front and back regions of large scale jet structure.

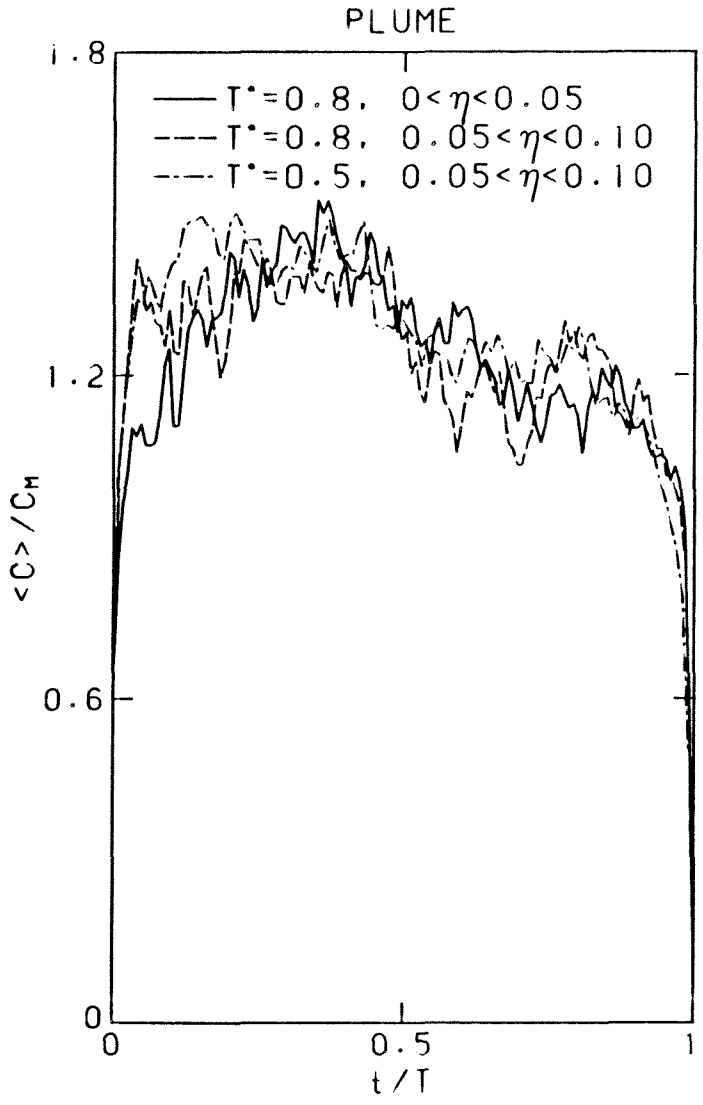

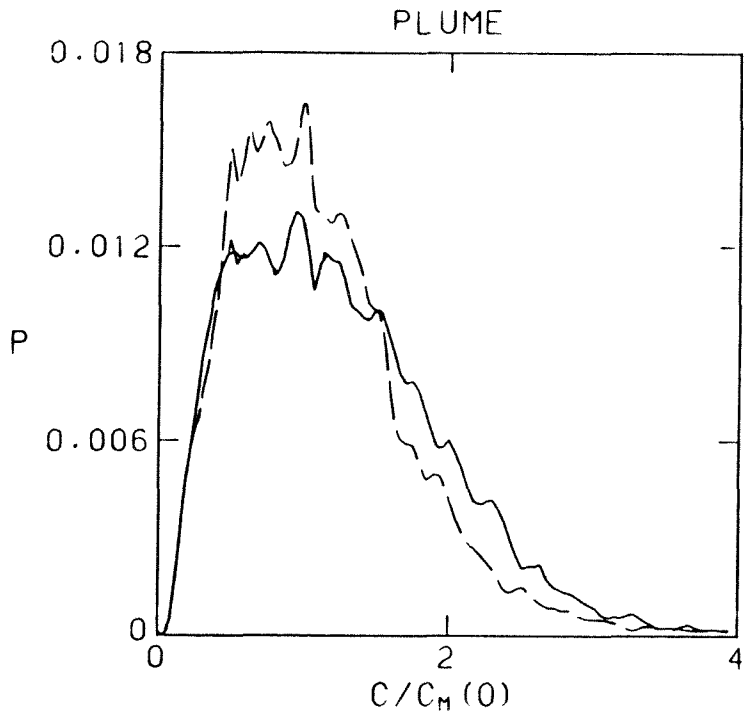

Figure 4.27a. **Ensemble average distributions of excursions in the normalized concentration signal in plume.**

Figure 4.27b. **PDF of concentration in front and back regions of large scale plume structure.**

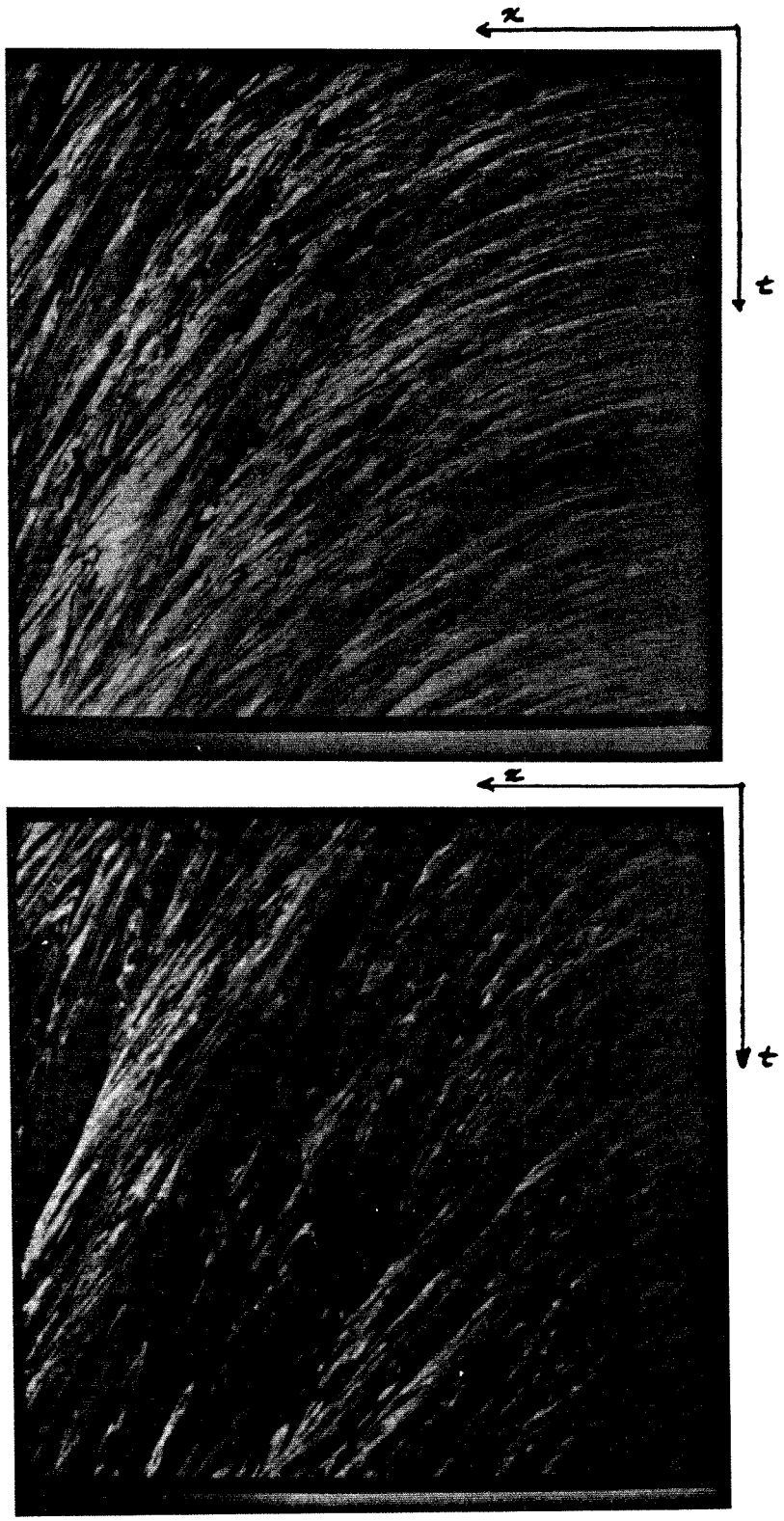

Figure 4.28. Evolution of the instantaneous axial profile of normalized concentration for $0 < x/d < 118$ a) Jet (upper) b) Plume (lower).

Table 4.1 Experimental parameters for jet experiments.

Initial conditions					
Reynolds number	5,600	5,600	5,600	5,600	9,000
Jet nozzle diameter (cm)	1	1	1	0.5	1
Local conditions					
Axial distance, x/d	48.5	75	105	150	105
Mean centerline vel. (cm/sec)	6.8	4.4	3.1	4.5	8.4
Kolmogorov scale estim. (mm)	.30	.46	.65	.46	.45
Small scale time estim. (sec)	.09	.17	.42	.21	.20
Large scale time estim. (sec)	2.8	6.8	13.5	6.6	5.0
Kolmogorov passage time (ms)	4.4	10.0	21.0	10.2	5.3
Length imaged on array (cm)	38.9	38.9	38.9	41.5	38.9
Static resolution per pixel (mm)	.38	.38	.38	.40	.38
Array clock period (microsec)	6.0	4.0	10.0	10.0	10.0
Line scan time (ms)	6.3	4.2	11.1	10.3	11.1
Pixels/scan recorded	51	256	512	1024	512
Recording interval (ms)	12.	16.4	22.2	41.28	11.1
Number of scans recorded	10240	20480	10240	5120	10240
Experimental duration (sec)	129.2	343.7	228.6	211.2	114.3

Table 4.2 Experimental parameters for plume experiments.

Initial conditions		
Reynolds number	1000	1600
Jet nozzle diameter (cm)	1	1
Richardson number	.28	.20
Local conditions		
Axial distance, x/d	105	105
Mean centerline vel. (cm/sec)	3.3	3.7
Kolmogorov scale estim. (mm)	.63	.58
Small scale time estim. (sec)	.40	.34
Large scale time estim. (sec)	12.7	11.3
Kolmogorov passage time (ms)	19.0	15.7
Length imaged on array (cm)	38.9	38.9
Static resolution per pixel (mm)	.38	.38
Array clock period (microsec)	10.0	10.0
Line scan time (ms)	10.3	10.3
Pixels/scan recorded	1024	1024
Recording interval (ms)	44.1	44.1
Number of scans recorded	5120	5120
Experimental duration (sec)	211.2	211.2

TABLE 4.4 Integral scales of concentration fluctuations

JET

Re	x/d	y/x	Λ/x	TU_m/x
5600	150	0.0	0.041	0.055
5600	150	0.1	0.046	
5600	105	0.0	0.029	0.034
9000	105	0.0	0.026	0.167

PLUME

x/L_m	x/d	y/x	Λ/x	TU_m/x
24	105	0.0	0.018	0.096
24	105	0.02		0.071
24	105	0.044	0.022	
33	105	0.0	0.011	0.022